"PREPARATION OF MIXED MANGANESE OXIDE *nano*-MATRIX AND STUDIES ON ITS OXIDATIVE AND PATHOGENIC ACTIVITIES"

By

MD. AMINUL ISLAM

Roll No. 0412033203P

SUBMITTED IN PARTIAL FULFILLMENT OF THE REQUIREMENT FOR
THE DEGREE OF MASTER OF PHILOSOPHY
(M. PHIL) IN CHEMISTRY

Material and Nano-chemistry Research Laboratory

Department of Chemistry

Faculty of Engineering

BANGLADESH UNIVERSITY OF ENGINEERING AND TECHNOLOGY (BUET)

Dhaka-1000, Bangladesh

February, 2015

CANDIDATE'S DECLERATION

It is hereby declared that this thesis or any part of it has not been submitted elsewhere for the award of any degree or diploma.

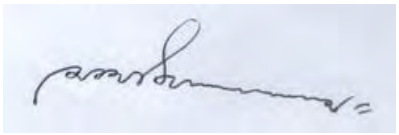

.....

Md. Aminul Islam
(Candidate)
M. Phil Student
Roll No. 0412033203 P
Department of Chemistry
BUET, Dhaka
Bangladesh

The thesis titled PREPARATION OF MIXED MANGANESE OXIDE *nano*-MATRIX AND STUDIES ON ITS OXIDATIVE AND PATHOGENIC ACTIVITIES, submitted by Md. Aminul Islam, Roll No. 0412033203 P, Session: April/2012 has been accepted as satisfactory in partial fulfillment of the requirement for the degree of Master of Philosophy (M.Phil) in Chemistry on February 28, 2015.

BOARD OF EXAMINERS

1. _____ Supervisor & Chairman
   Dr. Md. Manwarul Islam
   Professor
   Department of Chemistry
   BUET, Dhaka

2. _____ Member
   Dr. Md. Nazrul Islam (Ex-Officio)
   Professor & Head
   Department of Chemistry
   BUET, Dhaka

3. _____ Member
   Dr. Al-Nakib Chowdhury
   Professor
   Department of Chemistry
   BUET, Dhaka

4. _____ Member
   Dr. Mohammad Abu Yousuf (External)
   Professor
   Department of Chemistry
   KUET, Khulna – 9203.

Dedicated

to

my wife Tania Yeasmin and our son Md. Tajwar Islam Araf and our esteemed parents for their endless love and support

ACKNOWLEDGEMENTS

First of all, all praises are due to Almighty whose blessings and sympathetic direction had been with me throughout the execution of my entire research. I wish to give special thanks to my supervisors, Prof. Dr. Md. Manwarul Islam and Prof. Dr. Al-Nakib Chowdhury, for their kind guidance, support and encouragement during my M. Phil study. Without their trust, insightful suggestions and enormous knowledge, this thesis would not have been possible.

I am much indebted to all current and previous members of the Nano-chemistry Research Group for their assistance and cordial friendships. Most of the results in this thesis would not have been available without the enjoyable collaboration with Prof. Dr. Md. Monimul Haque, Prof. Dr. Md. Nazrul Islam, Dr. Md. Shakhawat Hossain Firoz and Dr. Md. Shafiul Azam. I also thank to Dr. Abu Bin Hasan Imran, Md. Elius Hossain and Md. Abu Hasan Hawlader for their help and fruitful discussions. I would especially like to mention my lab mates, Amad Hossain, Md. Shukanul Islam (Fuad), Md. Ikram, Akteruzzzaman, Samira Saimoma and Maria, who showed me the standard of excellence in research.

Special thanks must be given to all collaborators outside the Material and Nano-chemistry Group for their valuable assistance and suggestions, including Prof. Dr. Md. Yousuf Ali Mollah, Prof. Dr. Abu Bin Hasan Susan, Dr. Md. Mominul Islam and Dr. Md. Shah Miran at Department of Chemistry, University of Dhaka, Dr. Md. Mahbubur Rahman, ICDDR,B, Dhaka, Prof. Dr. Mahammad Abu Yousuf, Prof. Deptt. of Chemistry, KUET, Prof. Dr. M. Shahabuddin, Dr. S. M. Abdul Karim, Dr. Samar Kumar Guha and Md. Shahid Ullah, Deptt. of Arts and Sciences, Ahsanullah University of Science & Technology, Dhaka. I also sincerely thank to Md. Patwary, Md. Abdul Hakim, Md. Golam Rasul, Md. Kabir Hossain, Md. Belaet Hossain, Department of Chemistry, BUET for their cooperation.

Finally, I would like to express my sincerest gratitude to my wife, Tania Yeasmin and our son Md. Tajwar Islam Araf who has filled our life and heart. I would never have achieved this academic goal if it were not for their continual unselfish support. Lastly, I would like to give my deepest thanks to my parents and all of my family members for the love and warm support they have provided throughout my life. They have been and will always be my best source of inspiration. Financial support from the CASR, BUET is greatly acknowledged.

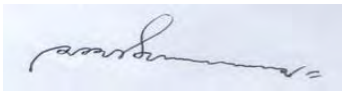

Md. Aminul Islam
Author

CONTENTS

CHAPTER-II

EXPERIMENTAL

CHAPTER-III

RESULTS AND DISCUSSION

LIST OF FIGURES

LIST OF TABLES

ABSTRACT

Nanotechnology is an emerging interdisciplinary subject that has been booming in many areas during the recent decade. Looking into this aspect, black MnO_2 nanoparticles (nps) have been synthesized, via a facile one stop solution phase approach, by co-precipitation method by the reduction from a system containing $KMnO_4$ and $MnSO_4$ solutions. Pure phase, spherical, uniformly dispersed brown Mn_3O_4 nps powder was synthesized successfully by forced hydrolysis of Mn(II) acetate by heating its aqueous solution at 80^0C. Blackish brown γ–MnOOH nps was synthesized by a simple route using Mn(II) acetate as precursor by hydrothermal treatment.

The evidence of MnO_2, Mn_3O_4 and γ–MnOOH nps formation under the synthesis conditions were confirmed by UV–vis spectra, FT-IR, XRD, SEM, EDX, DLS, TG-DTA, pH_{pzc} and Specific Surface Area (SSA) analysis. FT-IR spectra of MnO_2 nps showed the occurrence of O–Mn–O vibrational mode at around 571 and 535 cm^{-1}. The selected area electron diffraction patterns revealed that the MnO_2 was crystalline and rod like in nature. Elemental analysis exhibited the presence of Mn and oxygen elements in the MnO_2, Mn_3O_4 and γ–MnOOH and no foreign elements in them. The average crystallite size was calculated from the XRD data for MnO_2, Mn_3O_4 and γ–MnOOH nps were approximately 7.0 nm, 10.0 nm and 11.0 nm respectively. The specific surface area of γ–MnOOH nps was found to be 142.962 and 195.747 ($m^2 g^{-1}$) respectively.

Oxidative decolorization of MB and OG were studied at different pH, concentration, adsorbent dose and contact time by UV-Vis spectroscopy. From kinetic analysis, it was found that decolorization is dependent on parameters such as dye concentration, Mn-oxide doses, pH and other parameters. The observed results were in good agreement with experimental data.

The decolorization data showed that both MB and OG could be decolorized by Mn-oxide surface. But the extent of MB decolorization was much higher than OG, suggesting the present γ–MnOOH nps can be used as a highly efficient material for oxidative decolorization of MB. MB decolorization was through a surface mechanism, that is, formation of surface precursor complex between MB and surface bound MnOOH center, followed by electron transfer within the surface complex. Kinetic study demonstrated that both MB and OG decolorization followed pseudo-second-order kinetic.

The experimental isotherm results were fitted using Langmuir, Freundlich, Temkin and Sips isotherm. The Freundlich model agreed very well with experimental data.

The pathogenic experiment was performed following the standard conventional method by treating the Mn-oxides nps in 7.5% (v/v) DMSO suspension to various pathogenic organisms. The experiments were performed duplicate and triplicate. From the experimental evidence it was clear that Mn-oxides did not have potential antibacterial activity.

CHAPTER I

INTRODUCTION

CHAPTER- I

INTRODUCTION

1.1. Chemical aspects of nanomaterials

1.1.1. Nanomaterials

Nanomaterials, having a dimension scale 1-100 nm, have received increasing interest owing not only to their fundamental scientific significance but also to the potential applications that derive from their fascinating electrical, magnetic and catalytic properties [1-3]. Compared to bulk active electrode materials, the corresponding nanomaterials possess more excellent electrochemical activity, such as higher capacities, larger surface areas, and lower current densities, thereby, nanomaterials have wildly potential application in electrochemistry field. Manganese oxides, including MnO, MnO_2 and Mn_3O_4, are intriguing composites and have been used in wastewater treatment, catalysis, sensors, supercapacitors, and alkaline and rechargeable batteries [4–10]. Particularly, MnO and MnO_2 nanomaterials have attracted great interest as anode materials in lithium-ion batteries (LIBs) for their high theoretical capacity, low cost, environmental benignity, and special properties [11].

Nowadays, nano metal oxide is one of the promising materials for scientists. The applications of nano metal oxide particles are increasing day by day. The most commonly used transition metal oxides are titania, manganese oxide, zinc oxide, cobalt oxide, nickel oxide, iron oxide etc.

Nanotechnology is expected to be the basis of many of the main technological innovations of the 21^{st} century. Research and development in this field is growing rapidly throughout the world. A major output of this activity is the development of new materials in the nanometer scale, including nanoparticles. A unique aspect of nanotechnology is the vastly increased ratio of the surface area to volume present in many nanoscale materials which opens new possibilities in surface-based science, such as catalysis.

A number of physical phenomena become noticeably pronounced as the size of the system decreases. These include statistical mechanical effects, as well as quantum mechanical effects, for example the "the quantum size effect" where the

electronic properties of solids are altered with great reductions in particle size. This effect does not come into play by going from macro dimension. However, it becomes dominant when the nanometer size range is reached.

Materials reduced to the nanoscale can suddenly show very different properties compared to what they exhibit on a macroscale, enabling unique application. For instance, opaque substances become transparent (copper); inert materials become catalyst (platinum); stable materials turn combustible (aluminum); solids turn into liquids at room temperature (gold); insulators become conductors (silicon). Materials such as gold, which is chemically inert at normal scales, can serve as a potent chemical catalyst at nanoscales. Much of the fascination with nanotechnology exhibits at the nanoscale.

A nanoparticle (which historically has included nanopowder, nanocluster and nanocrystal) is a small particle with at least one dimension less than 100 nm. This definition can be fleshed out further in order to remove ambiguity from future nano nomenclature. A nanoparticle is an amorphous or semicrystalline zero dimensional (0D) nano structure with at least one dimension between 10 and 100 nm and a relatively large (≥15%) size dispersion [3].

1.1.2. Review of mixed metal oxide

Mixed-metal oxide (MMO) nanoparticles (nps) (also called heterometal oxide nanoparticles) have been intensively studied in the last decade for their unusual physical and chemical properties owing to their extremely small size, large specific surface area and number of promising applications. Among various classes of nanomaterials, metal oxides are very common, most diverse and possess richest class in terms of physical, chemical and structural properties. The result and prospects of numerous applications of metal oxides, such as fabrication of microelectronic circuits, sensors, piezoelectric devices, fuel cells, dielectrics, lasers, magnets and catalysts have been discussed in literature [1-13]. Recently, considerable effort has been made on the preparation of surface modified nanoparticles of different types of metal oxides. Mixed metal oxide nanoparticles can play an appreciable role in many areas of chemistry and physics. The unique

electronic and magnetic properties obtained when combining two metals in an oxide matrix have been well studied. However, the most common use for MMOs has been in the area of catalysis mixed metal oxides are also used in many applications in the electronic industry as passive or active components in devices. These exhibit high dielectric, and ferro- or pyroelectric properties, e.g., $BaTiO_3$, $LiNbO_3$, $KTaO_3$, $Pb_{1-x}La_xTi_yZr_2O_3$ etc.

1.1.3. Review of manganese oxide (MnO_x)

Manganese oxides are some of the most abundant minerals on earth, and can commonly be found in natural sediments, soils and ores. They are also prominent in formations such as desert rock varnish and marine manganese oxides [14]. Manganese occurs in a variety of oxidation states and chemical and structural forms. Manganese oxides are also powerful oxidants due to high reducing potential. Due to a variety of oxidation states as well as the facile phase transformations of MnOx during preparation, only a mixture of various manganese oxides (MnO_2, Mn_2O_3 and Mn_3O_4) is usually obtained. In addition, manganese oxyhydroxides (MnOOH) are often associated phases in wet synthesis. Manganese oxide is any of a variety of manganese oxides and hydroxides [13]. This includes:

(i) Manganese(II) oxide, Manganosite, MnO
(ii) Manganese(II, III) oxide, Hausmannite, Mn_3O_4
(iii) Manganese(III) oxide, Mn_2O_3
(iv) Manganese dioxide, (manganese(IV) oxide), Pyrolusite, MnO_2
(v) Manganese(VII) oxide, Mn_2O_7
(vi) manganese oxide-hydroxide ,Manganite MnOOH

Manganese may also form mixed oxides with other metals such as Fe, Nb, Ta:

(i) Bixbyite, a manganese iron oxide mineral
(ii) Jacobsite, a manganese iron oxide mineral
(iii) Columbite, also called niobite, niobite-tantalite and columbate
(iv) Tantalite, a mineral group close to columbite
(v) Coltan, a mixture of columbite and tantalite

(vi) Galaxite, a spinel mineral

(vii) Todorokite, a rare complex hydrous manganese oxide mineral.

There are over three dozen naturally-occurring crystalline manganese oxides with approximate MnO_2 stoichiometry. In addition, there are many amorphous forms [14-17]. Crystalline architectures of these materials are comprised primarily of edge-shared MnO_6 octahedral units which are arranged to form tunneled or layered structures. These structures contribute to the high porosity and surface areas of the manganese oxides. A few examples of crystalline tunneled and layered structures include the layered structure of birnessite and tunneled arrangements as seen in the 1x1 nonporous pyrolusite, 1x2 ramsdellite, 2x2 hollandite, 2x3 romanechite and 3x3 todorokite. Many of these materials have Mn(III)/Mn(IV) mixed-valency, imparting an overall negative charge to their framework. This allows the intercalation of cations and water molecules in tunnels or between layers, when there is an appropriately large volume. Due to high porosity, many manganese oxides exhibit high surface areas that are advantageous in potential applications related to rechargeable battery technology [14-17] toxic waste remediation [14, 18, 19] and heterogeneous catalysis [16, 20,21].

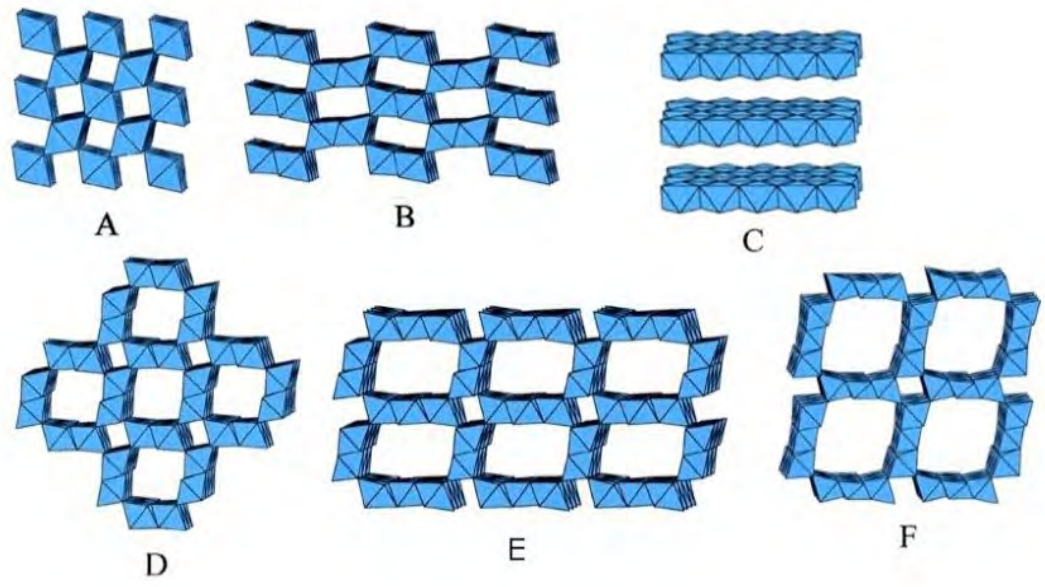

Fig.1.1. Crystalline structures of (A) pyrolusite, (B) ramsdellite, (C) birnessite, (D) hollandite, (E) romanechite and (F) todorokite.

1.1.4. Review of the chemistry of manganese (IV) oxide

Manganese (IV) oxide is the inorganic compound with the formula MnO_2 (Molar mass: 86.9368 g/mol, Melting point: 535°C, Density: 5.03 g/cm³, Insoluble in water but soluble in HCl and H_2SO_4. This blackish or brown solid occurs naturally as the mineral pyrolusite, which is the main ore of manganese and a component of manganese nodules. Of the known catalysts, MnO_2 is considered one of the best because of its low cost and toxicity, high catalytic activity, and environmental compatibility [20-22]. However, MnO_2 particle size and morphology importantly contribute to battery performance [22]. The principal use for MnO_2 is for dry-cell batteries, such as the alkaline battery and the zinc-carbon battery [23]. MnO_2 is also used as a pigment and as a precursor to other manganese compounds, such as $KMnO_4$. It is used as a reagent in organic synthesis, for example, for the oxidation of allylic alcohols. It is known that MnO_2 can exist in different structural forms, α-, β-, γ-, δ-, ε- and λ-types and so forth, when the basic structural unit MnO_6 octahedron is linked in different ways. Based on the different MnO_6 links, MnO_2 can be divided into three categories: the chain-like tunnel structure such as α-, β-, and γ types, the sheet or layered structure such as δ-MnO_2, and the 3D structure such as λ-type [23]. The properties of MnO_2 are significantly affected by their phases and morphologies; moreover, the operating properties of LIBs also depend on the phase of MnO_2. In this regard, a great effort has been directed toward the preparation of MnO_2 with different phases and various shapes [24]. Generally, MnO_2 nanostructures could be synthesized through the oxidation of Mn^{2+}, reduction of MnO_4^-, redox reactions between Mn^{2+} and MnO_4^-, or direct phase transformation from other manganese oxides. As regards all other non-noble metals or transition metal oxides studied in modern times, MnO_2 is one of the most attractive inorganic materials not only because of its physical and chemical properties and wide range of applications in catalysis, ion-exchange, molecular adsorption, biosensor and particularly energy storage but also because of its low cost and environmentally benign nature.

1.1.5. Review of manganese (II, III) oxide Mn_3O_4

Manganese is present in two oxidation states +2 and +3 and the formula is sometimes written as $MnO.Mn_2O_3$. (Molar mass: 228.812 g/mol, Appearance: red or brown, Density: 4.86 g/cm^3, Melting point: 1,567°C, Boiling point: 2,847°C, insoluble in water but soluble in HCl). Mn_3O_4 is found in nature as the mineral hausmannite. Mn_3O_4 formed when any manganese oxide is heated in air above 1000°C [25]. Considerable research has centered on producing nano-crystalline Mn_3O_4 and various syntheses that involve oxidation of Mn(II) or reduction of Mn(IV). Mn_3O_4 has been found to act as a catalyst for a range of reactions e.g. the oxidation of methane and carbon monoxide [26, 27]; the decomposition of NO [28], the reduction of nitrobenzene [29] and the catalytic combustion of organic compounds [30]. Mn_3O_4 has the spinel structure, where the oxide ions are cubic close packed and the Mn(II) occupy tetrahedral sites and the Mn(III) octahedral sites[25]. The structure is distorted due to a Jahn-Teller effect [25]. At room temperature Mn_3O_4 is paramagnetic, below 41-43K, it is ferrimagnetic [31]. Although it has been reported as reducing agent in nano-crystalline sample to around at 39K [32-33]. Mn_3O_4 is sometimes used as a starting material in the production of soft ferrites e.g. manganese zinc ferrite [34], and lithium manganese oxide, used in lithium batteries [35].

1.1.6. Review of manganese oxyhydroxide, manganite (γ−MnOOH)

There are three forms of MnOOH and they are α−MnOOH (groutite), β−MnOOH (feitknechtite) and γ−MnOOH (Manganite). Manganite (γ−MnOOH) is the most stable of the trivalent manganese hydroxides and is the hydroxide most like to be present in lakes and rivers with high manganese concentrations and or high sulphate concentration [36]. It occurs in the form of colloidal particles in water and sediments. Manganite is one dimensional nanostructure which has attracted a great deal of attention because of their potential applications in many fields including separation, chemical sensing devices, biology and electronics. Among them α and γ−MnOOH, present particular interest because of their applications as catalysts and as electrode materials in Li batteries [37].

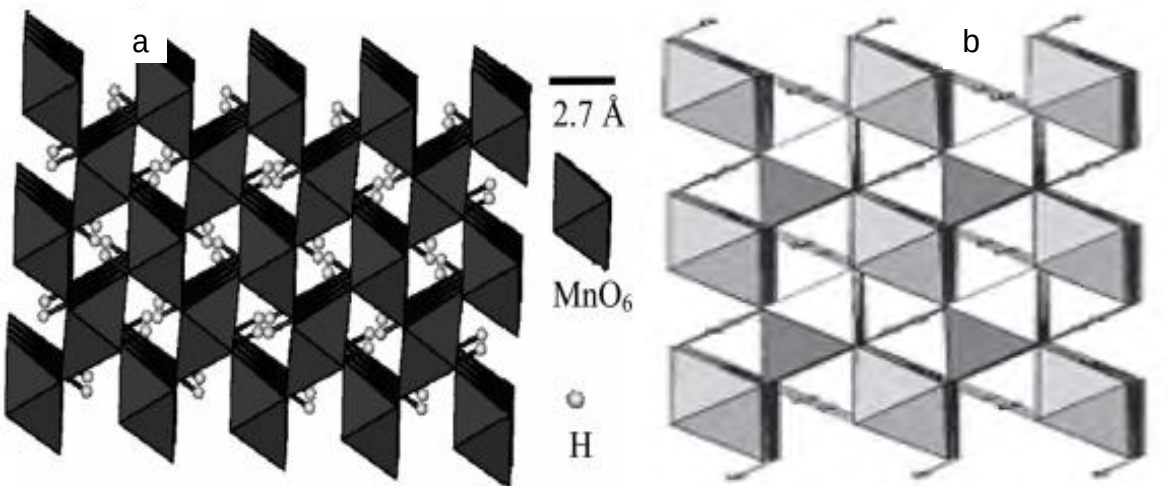

Fig.1.2. (a) Representation of the crystal structure of γ−MnOOH and (b) Illustration of tunnel structures of manganite. MnO_6 units are linked via edges and vertices.

The structure of monoclinic manganite consists of MnO_6 octahedra sharing edges to form single octahedral chains. These chains are corner linked by oxygen atoms parallel to the b-axis to a three dimensional framework. The octahedral framework of manganite is characterized by endless 1×1 edge-shared MnO_6 octahedral chains, which are corner-connected to form one-dimensional channels

of about 0.23 nm × 0.23 nm parallel to the c-axis. The hydrogen position is located in the interstitial channels between the chains and bonds to oxygen together with a H-bond to another oxygen.

1.2. Synthesis of manganese oxide nano materials

There is a great research interest for the synthesis of Mn-oxide nanoparticles due to their potential applications in electronic, optical and mechanical devices based on variable oxidation states. Different methodologies are used to synthesize metal oxide nanopowder but reported procedures have limited control on the particle functionality [36]. So it is an urgent need to modify the cost-effective procedure in chemical and environment friendly approach. These nanoparticles are of great importance because of their unique properties like large surface to volume ratio, high crystallinity, chemical purity, and phase selectivity which are different from their bulk counterpart. It has been reported that the physical and chemical properties are relative to its stoichiometry as well as particle size and shape. MnO_2, Mn_3O_4 nanoparticles are potentially used in various fields such as electrodes [36] catalysis [37] sensors [38] and in optoelectronics [39].

1.3. Synthesis techniques of Mn-oxides

The first requirement of any novel study of nanoparticulated oxides is the synthesis of the material. The development of systematic studies for the synthesis of oxide nanoparticles is a current challenge and essentially, the corresponding preparation methods may be grouped in two main streams based upon the liquid-solid and gas-solid nature of the transformations. Developments in the field of MMO nanoparticles have produced many significant and interesting results in all areas investigated. This attracted attention toward the preparation of these potential new materials with variable composition having unique properties. Researchers have explored and developed both physical and chemical methods by which such materials can be prepared. Supported metal oxide and mixed metal oxide are usually prepared by the following methods:

1.3.1. Physical Methods

a) Vapor condensation method,
b) Spray Pyrolysis,
c) Thermochemical / flame decomposition of metal and
d) organic precursors

1.3.1 (a). Vapor condensation method

It involves two steps. In the first step, a metallic nanophase powder is condensed under an inert convection gas at high pressure, after the supersaturated vapor of metal is obtained inside a chamber. In the second step, the powder is oxidized by allowing oxygen into the chamber. It is a critical step in which the temperature is as high as 1000^0C because of the exothermic nature of the reaction.

1.3.1(b). Spray Pyrolysis

The starting materials, or chemical precursors, are usually the appropriate salts, either in solution or in a sol or in suspension form. Aerosol droplets are generated by nebulizer or atomization technique. These droplets generated undergo evaporation with solute condensation within the droplet followed by drying and thermolysis of precipitate particles at high temperatures forming microporous particles. They are finally sintered to form dense particles.

1.3.2. Chemical Methods

a) Precipitation,
b) Co-precipitation,
c) Incipient wet impregnation,
d) Deposition,
e) Grafting,
f) Sol-gel method,
g) Precipitation-deposition,
h) Selective removal and

i) Reverse microemulsion/micelle method.

1.3.2(a). Precipitation method

Hydroxide or carbonate of the desired metal is precipitated out from solution by using a precipitating agent [44]. The hydroxides or carbonates are decomposed by heating to the oxides, which are, reduced to the metal when required on to a suspension of the support. In all precipitations it is essential to carefully control all the details of the process including.

(i) The order and rate of addition of one solution into the other.

(ii) The mixing procedure.

(iii) The pH and variation of pH during the process and

(iv) The maturation process.

Precipitation involves two distinct processes, namely nucleation and growth. Nucleation requires that the system is far from equilibrium. Growth of the new phase takes place in conditions which gradually approach the equilibrium state.
Many procedures are used for precipitation. One simple method is to add drop-wise the solution containing the active component to the precipitating solution, or vice versa. There is little difference between those inverse procedures. In both cases high super saturation can be produced locally, leading, if the solubility constant is low, to fine precipitates. If not, redissolution takes place at the beginning of the process, when agitation disperses the precipitate in the liquid. In both cases, concentrations change continuously throughout the precipitation process resulting in an inhomogeneous product being formed, at least with respect to texture. Any precipitation process is situated somewhere between two extremes. Either the solutions are contacted instantaneously (only an ideal situation as, in all cases, diffusion has to take place), the super saturation decreasing continuously, or the super saturation is maintained constant during the whole precipitation process.

Instantaneous precipitation is achieved by two methods. The first consists in pouring continuously, in constant proportion, both solutions into a vessel under constant and vigorous stirring. The second consists in mixing the solutions

through specially designed mixing nozzles. The latter method ensures a better uniformity in composition and texture of the Precipitate.

1.3.2(b). Co-precipitation method

This method involves the addition of a precipitation agent leading to the formation of a mixture of metal compound and the support, both previously in solution. This method is traditionally associated with nickel alumina catalyst used mostly in the hydrogenation of unsaturated fatty oils [41]. At a defined temperature the precipitating agent is OH^- ions that convert the active metal salts to a mixture of metal hydroxide. After drying, the decomposed and reduced to get a co-precipitated supported catalyst. This method offers a better surface in terms of homogeneity, though some of the active component may be embedded within the carrier and hence not available. This method is especially employed for the preparation of mixed oxide catalyst.

1.3.2(c). Sol-gel method

Sol-gel preparation, which involves the formation of a sol followed by formation of a gel, typically uses either colloidal dispersions or inorganic precursors as the starting material. However, it is important to realize that sol-gel preparation can be done with a wide variety of precursors. With an alkoxide M(OR) as a precursor, sol-gel chemistry can be described in terms of two classes of reactions:

Hydrolysis: $MOR + H_2O = MOH + ROH$

Condensation: $MOH + ROM = MOM + ROH$

or $MOH + HOM = MOM + H_2O$

Despite its oversimplification, this description of sol-gel chemistry identifies two key ideas. First, a gel forms because of the condensation of partially hydrolyzed species into a three-dimensional polymeric network. Second, any factors that affect either or both of these reactions are likely to impact on the properties of the gel. In fact, it is the control of many of these factors, generally referred to as sol-gel parameters that separate sol-gel preparation from other

methods. A representative but not exhaustive list of these parameters includes type of precursor, type of solvent, water content, acid or base content, precursor concentration, and temperature. These parameters affect the structure of the initial gel and, in turn, the properties of the material at all subsequent processing steps [42].

A gel, a solid matrix encapsulating a solvent, needs to be dried to remove the solvent. The time between the formation of a gel and its drying, known as aging, is also an important parameter. As Scherer pointed out, a gel is not static during aging but can continue to undergo hydrolysis and condensation. Furthermore, syneresis, which is the expulsion of solvent due to gel shrinkage, and coarsening, which is the dissolution and reprecipitation of particles, can occur. These phenomena can affect both the chemical and structural properties of the gel after its initial formation. One other parameter that affects a sol-gel product is the drying condition. Conventional evaporative drying, such as heating a gel in an oven, induces capillary pressure associated with the liquid-vapor interface within a pore. In a sample with a distribution of pore sizes, the resultant differential capillary pressure often collapses the porous network during drying. The dried sample, known as a xerogel, thus often has a surface area and pore volume that is too low to be of catalytic interest. There are several ways to minimize the deleterious effect of conventional drying, and xerogels with high surface areas and pore volumes can be prepared with care. One other approach is that of Kistler, who used supercritical drying to bypass the problem of differential capillary pressure. The resultant materials, known as aerogels, have high surface area, porous structure, and low density. In a way drying can be viewed as part of the overall aging process because the material can, and often does, undergo physical and chemical changes during this stage [43].

1.3.2(d). Reverse microemulsion/micelle method

Surfactants dissolved in organic solvents to form spheroidal aggregates called reverse micelles. The polar ends of surfactant molecules organize around small water pools (100A°) in the presence of water. This leads to dispersion of aqueous

phase in the continuous oil phase. These reverse micelles are used as water solutions of reactive precursors to prepare insoluble nanoparticles. Solvent removal followed by calcinations lead to the final product.

1.4. Properties of metal oxide nanoparticles

The current knowledge on oxide materials allows affirming that most of their physico-chemical properties display acute size dependence. Physico-chemical properties of special relevance in Chemistry are mostly related to the industrial use of oxides as sensors, ceramics, absorbents and/or catalysts. A bunch of novel application within these fields rely on the size-dependence of the optical, (electronic and/or ionic) transport, mechanical and, obviously, surface/chemical (redox, acid/base) properties of oxide nanomaterials. We should stress that size effects in oxide chemistry have frequently two interrelated faces, structural/electronic quantum influence of these two phenomena in the main physico-chemical properties of oxides. Properties of MMO nanoparticles are mainly size dependent, and their chemical and physical properties are unique in comparison to corresponding bulk materials.

1.4(a).Chemical properties

i) Acid–base behavior (catalysts)

This behavior varies from one MMO to another. Some exhibit surface basic behavior and some surface acidic behavior, whereas mixtures show unusual properties. The mixing of two oxides can enhance the catalytic activity many fold because of synergistic effects, as seen in the mixed aerogel of titania/zirconia.

ii) Unusual adsorptive properties

Perhaps one of the greatest promises of MMO nanoparticles in chemistry is their ability to chemically adsorb a wide range of organic molecules or inorganic gases that are considered as hazardous environment pollutants. They not only adsorb but also dissociate these to nonhazardous substances on their surface.

Carnes et al. studied the adsorption of CCl_4, SO_2, and paraoxon on both Al_2O_3 and Al_2O_3/MgO.

1.5. Characterization of metal oxide

Metal oxide characterization is necessary to establish understanding and control of metal and mixed metal oxides synthesis and application. Characterization is done by using a variety of different techniques, mainly drawn from metal oxide materials. Common techniques are Electron Microscopy [TEM, SEM], Atomic Force Microscopy [AFM], Dynamic Light Scattering [DLS], X-ray Photoelectron Spectroscopy [XPS], Powder X-ray Diffractometry [XRD], Energy Dispersion X-ray (EDX) spectroscopy, Fourier Transform Infrared Spectroscopy [FT-IR] TG-TDA, point of zero charge (pH_{PZC}) and SSA analysis. Whilst the theory has been known for over a century, the technology for Nanoparticle Tracking Analysis (NTA) allow a direct tracking of the Brownian motion and this method therefore allow the sizing of individual nanoparticles of metal oxide in solution [44].

1.6. Structure and surface morphology of mixed oxides

1.6.1. Spinel structures

The general formula of spinel is written as AB_2O_4 [where, A is a Group 2 metal ion or transition metal in +2 oxidation state and B is a Group 3A (B, Al, Ga, In) cation or transition metal ion in +3 oxidation state]. As a unit cell has 32 O_2 ion and only 4 are present per molecule (from the formula), then spinel structure has 8 (64/8) tetrahedral and 4 (32/8) octahedral vacancies per molecule of AB_2O_4.

1.6.2. Perovskite structures

The class of MMOs having the formula ABO_3 (such as $CaTiO_3$) is called perovskite. The structure of this mineral was first thought to be cubic but later confirmed as orthorhombic. The truly cubic form is referred to as "ideal perovskite" having a unit cell edge of A° containing one ABO_3.

1.6.3. Surface morphology

Control over structural and morphological properties is most crucial for performance of MMO nanoparticles in various applications. Mixed metal oxides are known to have different structural arrangement of constituent ions. The nature of these ions is important (size and charge) in the final adaptation of geometry. As MMOs contain a variety of cations, the prediction of structure simply on the basis of radius ratios of cations and oxide ions becomes complicated. This means some simpler approach is required. For example, take a list of known structures and the radii of the ions present in them. The radii of two of the ions present in a given compound are plotted against each other.

Scientists have taken to naming their particles after the real world shapes that they might represent. Nanospheres [45], Nanoreefs [46], nanoboxs [47], microsphere [45] and more have appeared in the literature. These morphologies sometimes arise spontaneously as an effect of a templating or directing agent present in the synthesis such as micellular emulsions or anodized alumina pores, or form the innate crystallographic growth patterns of the materials themselves. Some of these morphologies may serve a purpose, such as long carbon nanotubes being used to bridge an electrical junction, or just a scientific curiosity like the stars shown at left. As MMOs contain a variety of cations, the prediction of structure simply on the basis of radius ratios of cations and oxide ions becomes complicated. This means some simpler approach is required. For example, take a list of known structures and the radii of the ions present in them. The radii of two of the ions present in a given compound are plotted against each other.

1.7. Applications of Mn-oxide nanomaterials

From the past and even recently MMO materials preparation have received great interest because of the large variety of their potential applications such as in catalysis [48, 49] adsorption [50, 51], as anode [52] and alternative cathode material [53]. Taylor et al. [54] also reported the use of a mixed oxide of copper and zinc as catalysts. MMO can also be used as material as capacitor [55], its

films as pH sensing materials [56], as pigments [57] and also found as coating materials [58].

Metal oxides with wide or moderate band gap, such as TiO_2, CeO_2, ZrO_2, and HfO_2, have been widely used for various applications like semiconductor materials in dye-sensitized solar cell, catalysts, fuel cells, resistors, gas sensors, transparent optical device, and optical coatings [59-60]. Oxide materials, which have very important optical properties, can also be used in the fields such as short wavelength lasers, blue light emitting diodes, UV detectors, gas sensors, etc. [61]. The American Nuclear Society (ANS) also endorses the rapid application of mixed oxide (MOX) fuel technology to accomplish the timely disposition of surplus weapons-grade plutonium in the United States and in the Russian Federation (November 2002).

1.8. Review of dye

Dye has been used since the prehistoric times. The prehistoric man used to dye furs, textile and other objects with natural substances, mainly vegetable, but also of animal origin. Nowadays, dyes are not only made from the natural sources but also there are synthetic dyes. They are widely used in many industries such as textile, paper, leather and mineral processing industries to colour their product. Dye is a natural or synthetic colouring material, whether soluble or insoluble, which impart its colour to a material by staining or being imbibed by it, and which employed from a solution of fine dispersion, sometimes with aid of mordant.

A dye can generally be described as organic colorants that have an affinity to the substrate which it is being applied and consists of a color producing structure.

Dyes can be firmly fixed to the fabrics and other supporting materials used in textile, food and other industries for imparting different shades of colors [62]. All colored compounds are not dyes. A substance is referred to as a dye when it bears the following criteria:

i) It must have a desired color to match the object to be dyed.
ii) It must be capable of being fixed to the fabrics or supports directly or indirectly with the help of certain reagents called mordant.

iii) When fixed to the supports, the color must be fast to light and resistant to soap and water and to a certain extent to dilute acids and alkalis.

1.8.1. Classification systems for dyes

Dyes can be grouped in accordance with two different principles:

(a)Chemical structure (chemical classification)

(b)Dyeing methods areas of application (colouristic classification)

A review of the whole field of technical dyes shows that the two classifications overlap that there is hardly a chemical class of dye, which occurs solely in one coloristic group, and vice versa. When classified according to the dyeing method, they may be anionic, direct or disperse dyes, depending on whether they are intended for use on protein, cellulose or polyamide fibers. Moreover, certain reactive dyes with a particular type of chemical structure can be used for several substrates, whilst others with the same type of structure are suitable for only a single substrate.

It is possible to devise a logical method of chemical classification. With some classes of dyes, however, we have abandoned the conventional nomenclature, since it is either wrong (for instance, 'basic' instead of 'cationic' dyes) or insufficiently comprehensive (e.g., phthalocyanine as a sub group of azo annulene structure). Both classifications are used by the Colour Index (1971) which lists all dyes and pigments used commercially for large-scale colouration purposes, that is dying of textile fibers, for pigment colouration of plastics, paints, printing inks and for the colouration of liquids (solvent and so on).

Dyes are classified as anionic, cationic and nonionic. Anionic dyes are the direct, acid and reactive dyes. A cationic dye is basic dyes; while a nonionic dye is disperse dyes. Nonionic dyes refer to disperse dyes because they do not ionize in an aqueous medium. The chromophores in anionic and nonionic dyes are mostly azo groups or anthraquinone types. Where, chromophore is the group producing the colour.

1.8.2. Review of Methylene blue (MB)

Methylene blue (MB) ($C_{16}H_{18}N_3SCl$) is the typical organic cationic dye. Molecular mass of MB is 355.89 and λ_{max} of MB is 664 nm. It is the most commonly used substance for dying cotton, wood and silk. It is also used as a photosensitizer commonly employed in solar cells, a photodynamic antimicrobial agent in biological materials, a test compound in semiconductor photocatalysis, and a surface modifier of semiconductor colloids [63–66]. Other than a marked quantity of colorful wastewater generated from various industrial processes, the biodegradable resistance of MB suggests that physicochemical treatments are indispensable for effectively controlling pollution [67-71]. The chemical structure is shown in **Fig. 1.3.**

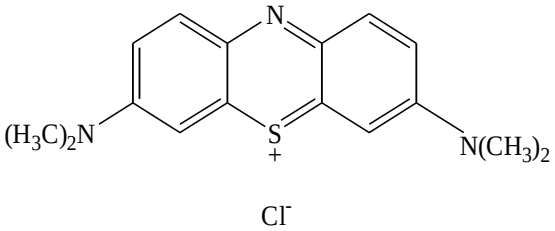

Fig. 1.3. Chemical structure of methylene blue (MB).

1.8.3. Review of orange green (OG)

Orange green is a typical azo anionic dye in textile wastewaters whose molecular mass is 452.38 and λ_{max} of OG is 477 nm. The chemical structure of orange Green (OG) is shown in **Fig. 1.4.**

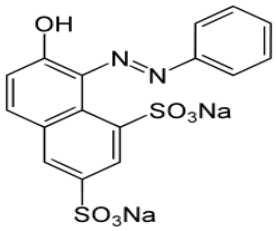

Fig. 1.4. Chemical structure of orange Green (OG).

1.9. Importance of dye removing

Water is absolutely essential to animals and plants in order for their survival. Human beings use water for drinking, bathing, washing, culinary purpose, transportation, industrial and agricultural activities etc [72]. The day to day

human activities and industrial revolution have influenced the flow and storage of water and the quality of available fresh water. Many industries like textile, refineries, chemical, plastic and food processing plants produce wastewater characterized by a perceptible content of organics [73]. Significant amounts of chemically different dyes are used in various industries such as textile, pesticide, paint, solvent, pharmaceuticals, paper, pulp and petroleum etc [74, 75].

Textile and other industrial dyes have become major environmental contaminants in many countries including Bangladesh owing to their non-biodegradability and toxicity [76-78]. Several of these dyes are stable and resist photodegradation by sunlight, oxidation by molecular oxygen O_2, and decomposition by common acids and bases. A typical textile dyeing process consists of resizing, scouring, bleaching, dyeing, finishing and drying operations. Dyeing is a fundamental operation during textile fiber processing. The dyeing process consumes large quantities of water for dyeing, fixing and washing and produce large volume of wastewater [79]. Over the last decades, the increasing demand for dyes by the textile industries has shown a high pollutant potential. It is estimated that around 10-15% of the dyes are lost in the effluent during the dyeing processes [80].

The effluent generated from the textile processing industries are considered to be a very complex and inconsistent mixture of many pollutants, such as, mixture of heavy metal ions (e.g., Cr, Al, Cu etc.), suspended solids, dissolved solids, inorganic salts, dispersing agents, dyestuffs, and other toxic organic pollutants including poly vinyl alcohol, starches, various surfactants, organic-chlorine based pesticides, biocides as well as acidic and alkaline contaminants.

Effluents discharged from textile and dyeing industries are characterized by low BOD, high COD and variation of pH in the range of 2-12 [81-82]. Color is usually the first contaminant to be recognized in wastewater; a very small amount of dye in water (10-20mg/L) is also highly visible and affects water transparency and the gas solubility of water bodies. The discharge of these colored dye effluent as wastewater in the ecosystem is a damaging source of esthetic pollution, eutrophication, and interruption in many natural processes (e.g., photosynthesis,

respiration) and perturbations in aquatic life. These dyes in the strongly absorb sunlight, which decreases the intensity of light absorbed by water plants and phytoplankton, reducing photosynthesis and the oxygenation of water reservoirs [83]. Dyes often contain elements such as nitrogen, Chlorine or sulfur. The oxidation product of these molecules may be more toxic than the parent molecule. Because of these unbearable problems created by the discharge of dyes as effluent, it requires clear concepts about dye and its undesirable impact and a quick search for the remedy of these problems.

1.10. Disadvantages of dyes

Many dyes are toxic. This is because many dyes are made from known carcinogens, such as benzidine and other aromatic compounds [84]. Dye bath effluent, in particular are not only aesthetic pollutants by nature of their colour but also can interfere light penetration through the bodies of water [85]. Hence, dyes disturbing biological process of the aquatic life especially the photosynthesis activity. Furthermore, dyes are also carcinogenic, mutagenic, or teratogenic in various microbiological, fish species. It also can cause severe damage to human beings such as dysfunction of kidney, reproductive system, liver brain and central nervous system [86]. The better representation may be possible in the **Table 1.1** according to different dye class[87] .

Table 1.1. Disadvantages of different dye class

Dye class	Disadvantages
(i) Azo groups	Their reductive cleavage of azo linkages is responsible for the formation of toxic amines in the effluent.
(ii) Anthraquinone-based	It is most resistant to degradation due to their fused aromatic ring structure and thus remains coloured for a longer time in wastewater.
(iii) Basic dyes	It has high brilliance and intensity of colours and is highly visible even in a low concentration.

Especially some disperse dyestuffs have been found to cause allergic reactions, i.e. eczema or contact dermatitis. Reduction of azo dyes, i.e. cleavage of the dyes azo linkage(s), leads to formation of aromatic amines. The acute toxic hazard of aromatic amines is carcinogenesis, especially bladder cancer. Hence, dye removal is very much essential.

1.11. Treatment technologies of dyes removal

Conventional biological wastewater treatment systems are inefficient in treating dye wastewater. This is due to the low biodegradability of dye. Usually dye wastewater treated by physical- or chemical-treatment process. These include physico-chemical flocculation combined with flotation, electroflotation, flocculation with Fe(II)/$Ca(OH)_2$, membrane-filtration, electrokinetic coagulation, precipitation, ozonation and Katox treatment method involving the use of activated carbon and air mixtures [88] have done a review on the widely used methods of removal dye from dye-containing industrial effluents. The methods have been categorized in three categories, which are chemical, biological, and physical. Various physical, chemical and biological treatment techniques can be employed to remove color from dye containing wastewaters [81-82]. Physico-chemical techniques include membrane filtration, coagulation/flocculation, precipitation, flotation, adsorption, ion exchange, ion pair extraction, ultrasonic mineralization, electrolysis, advanced oxidation (chlorination, bleaching, ozonation, Fenton oxidation and photocatalytic oxidation) and chemical reduction. Biological techniques include bacterial and fungal biosorption and biodegradation in aerobic, anaerobic, anoxic or combined anaerobic/aerobic treatment processes.

1.11.1. Chemical methods

1.11.1(a). Oxidative processes

This is the most commonly used method of decolourisation by chemical means. This is mainly due to its simplicity of application [89]. It was stated that there is a need for more powerful oxidizing methods, such as chlorine, ozone, Fenton's reagent (peroxide and ferous sulfate), UV/peroxide, UV/ozone, or other oxidizing techniques or combination. This is because modern dyes are resistant to mild oxidation condition, such as exist in biological treatment system. The main oxidizing agent is usually hydrogen peroxide. This agent needs to be activated by some means, for example, ultra violet light.

1.11.2. Biological method

1.11.2(a). Decolourisation by white-rot fungi

White-rot fungi are those organisms that are able to degrade lignin, the structural polymer found in woody plants [89]. The most widely studied white-rot fungus, in regards to xenobiotic degradation, is *Phanerochaete chrysosporium.* This fungus is capable of degrading dioxins, polychlorinated biphenyls (PCBs) and other chloro-organics [90] also showed the potential of using *P. sordida* to treat creosote-contaminated soil. *P.chrysosporium* had the ability to decolourise artificial textile effluent by up to 99% within 7 days [91].

1.11.2(b). Other microbial cultures

Mixed bacterial cultures from a wide variety of habitats have also been shown to decolourise the diazolinked chromophore of dye molecules in 15 days [92]. They demonstrated that a mixture of dyes was decolourised by anaerobic bacteria in 24-30 hrs, using free growing cells or in the form of biofilms on various support materials. Ogawa and Yatome (1990) also demonstrated the use of bacteria for azo dye biodegradation [93]. These microbial systems have the drawback of requiring a fermentation process, and are therefore unable to cope with larger volumes of textile effluents.

1.11.2(c). Adsorption by living/dead microbial biomass

The uptake or accumulation of chemicals by microbial mass has been termed biosorption [94]. Dead bacteria, yeast and fungi have all been used for the purpose of decolourising dye-containig effluents. Textile dyes vary greatly in their chemistry, and therefore, their interactions with micro-organisms depend on the chemistry of a particular dye and the specific chemistry of the microbial biomass [95]. Depending on the dye and the species of micro-organism used different binding rates and capacities was observed. It can be said that certain dyes have a particular affinity for binding with microbial species.

1.11.3. Physical methods

1.11.3(a) Adsorption: surface process

Adsorption techniques have gained favour recently due to their efficiency in the removal pollutants too stable for conventional methods. Adsorption produces a high quality product, and is a process, which is economically feasible [96]. Also, adsorption process provides an attractive alternative treatment, especially if the adsorbent is inexpensive and readily available [97]. Furthermore, this process has the edge on the other method due to its sludge free clean operation and complete removal of dyes even from dilute solution [98]. Therefore, one of the powerful treatment processes for the removal of dyes from water with a low cost is adsorption. Several adsorbents are eligible for such a purpose.

Adsorption is operative in most natural physical, biological, and chemical systems, and is widely used in industial applications such as activated charcoal, synthetic resins and water purification. Although there is no chemical distinction between the molecules or atoms on the surface and the molecules or atoms in the bulk, energy considerations lead to quite dissimilar properties.

Adsorption is a process that occurs when a gas or liquid solute accumulates on the surface of a solid or a liquid (adsorbent), forming a molecular or atomic film (the adsorbate). Adsorption is a surface phenomenon. Formally adsorption may be defined as a process in which the concentration of a chemical species is greater in the surface than in the bulk resulting from inelastic collision suffered by molecules on the surface. The species that is adsorbed is called adsorbate and the material of the surface on which adsorption takes place is called adsorbent. Adsorption strictly refers to accumulation of adsorbate on the surface only due to residual field of force. It is different from absorption, in which a substance diffuses into a liquid or solid to form a solution. The term sorption encompasses both processes, while desorption is the reverse process.

1.12. Classification of adsorption

Adsorption is a consequence of surface energy. In a bulk material, all the bonding requirements (be they ionic, covalent or metallic) of the constituent atoms of the material are filled. But atoms on the (clean) surface experience a bond deficiency, because they are surrounded by other atoms. The adsorbed material is generally classified as exhibiting two categories:

(a) Physisorption and

(b) Chemisorption.

1.12.1. Physisorption

Physisorption occurs when non-balanced physical forces appear at the boundary of the phases and adsorbed species is attached to the surface by weekly Van der Waals force. Physisorption is characterized by,

i) Low heat of adsorption (10-40 KJ/mol).

ii) Non specific.

iii) Mono or multi-layer.

iv) Rapid, non activated and reversible.

v) Significant at low temperature.

vi) No electron transfer.

1.12.2. Chemisorption

Adsorption, which results from chemical bond formation (strong interaction) between the adsorbent and the adsorbate in a monolayer on the surface, is called chemisorption. Chemisorption is characterized by,

i) More heat of adsorption (80-400 KJ/mol, sometimes endothermic).

ii) Very specific for active site of heterogeneous catalyst.

iii) Mono-layer only.

iv) Effective over a wide range of temperature.

v) Slow, activated and irreversible.

vi) Electron transfer between adsorbate and surface.

1.13. The main purpose of the adsorption study

Numerous investigations have focused on surface adsorption as a means of removing textile dyes from water. Beside, the following information can be obtained in an adsorption experiment:

(i) Nature of adsorption, that is whether it is adsorbed physically or chemically and the conditions (temperature, pressure, state or adsorbent etc.) under which the adsorption takes place.

(ii) Thermodynamic data regarding the adsorption process. This include the amount of the adsorbent adsorbed under various equilibrium concentrations at definite temperature.

(iii) Specific surface area-surface area of one gram of the substance by the adsorption process can also be measured.

1.14. Adsorption isotherms

Adsorption is usually described through isotherms. Many different types of isotherms have been observed in the literature [99, 100]. These isotherms can have very different shapes depending on the type of adsorbent, the type of adsorbate, and intermolecular interactions between the solute and the surface.

The variation of surface coverage (Θ) with equilibrium pressure (or concentration in the case of solution) at a given temperature is called adsorption isotherm. According to IUPAC classification [101], there are six different types of adsorption isotherm as shown in **Fig. 1.5**:

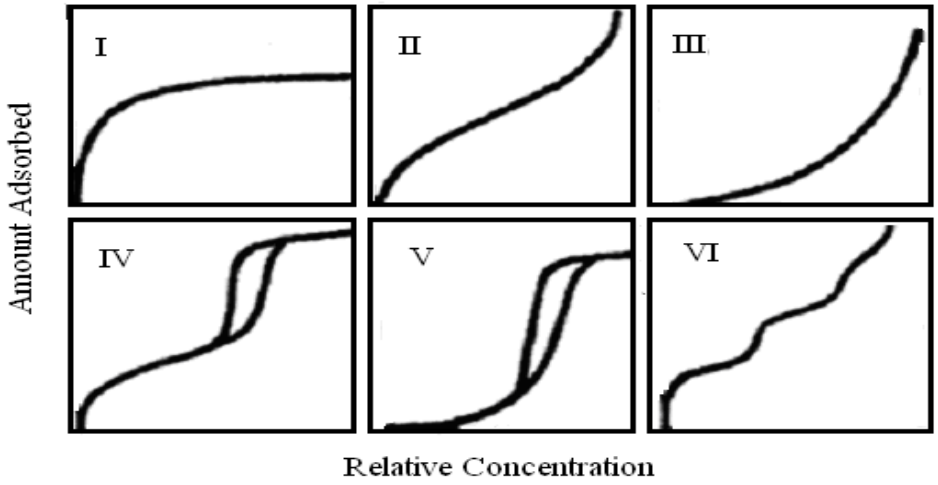

Fig. 1.5. IUPAC classification of adsorption isotherms.

(a) Type 1: This shape of the isotherm is characterized by the asymptotic approach of monolayer of adsorbate on the surface.

(b) Type 2: This is the most common type of isotherm corresponding to multi-layer formation on a surface of high adsorption potential.

(c) Type 3: This pattern of isotherm is comparatively uncommon, corresponding to multi-layer formation on the solid.

(d) Type 4 and 5: These are analogous to type 2 and 3 on porous adsorbents where the adsorption is limited by the volume of mesopores, causing the adsorption to level off at a pressure less than saturation pressure of adsorbate (P_0). They reflect capillary condensation and may show hysteresis effect.

IUPAC classification considers adsorption at sub critical temperature, but adsorption at near critical and super critical temperature was not considered. Hence this classification is incomplete. Considering the adsorption at near or super critical temperature a new classification is proposed as shown in **Fig. 1.6.**

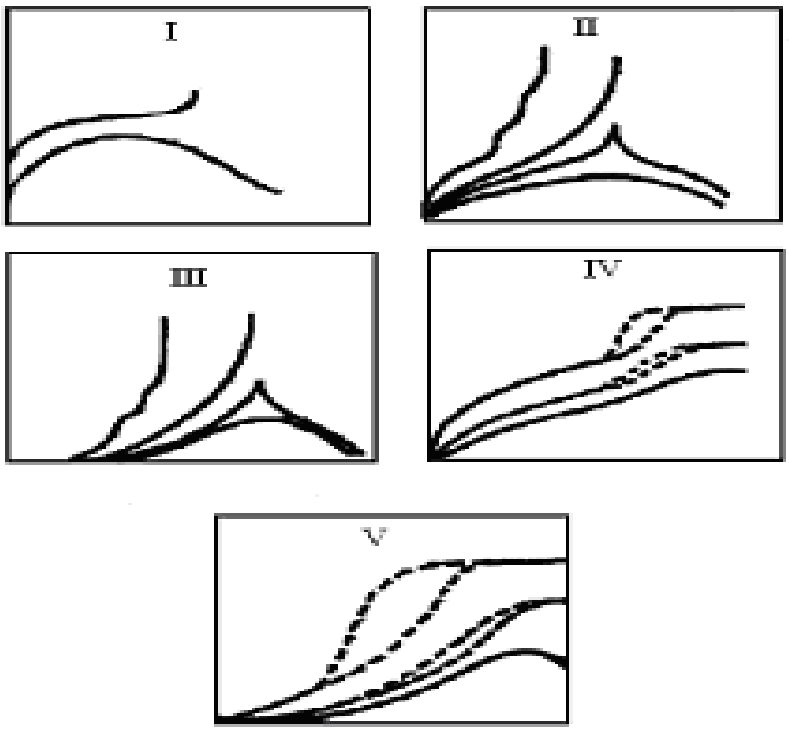

Fig. 1.6. A new classification for adsorption isotherms.

1.15. Model of adsorption isotherms

Several theoretical models were proposed in order to explain the experimental adsorption isotherms:

a) Langmuir isotherm,
b) Freundlich isotherm,
c) BET isotherm,
d) Temkin isotherms and
e) Sips Isotherm.

1.15.1. Langmuir isotherm

Characteristics feature of Langmuir isotherm equation:

(i) Adsorption is limited to monolayer formation.

(ii) In the case of physisorption, this equation satisfactorily explains adsorption behavior only at low surface coverage and at low adsorbate pressure.

(iii) In the case of chemisorption which is associated with monolayer coverage Langmuir equation is quite consistent.

Langmuir derived the following equation to explain the experimental adsorption isotherm:

$$C_e/q_e = C_e/q_m + 1/ K_L q_m$$

Where, q_e is the amount of adsorbate adsorbed at equilibrium Conctration, (C_e) in mg/g and q_m is the monolayer capacity in mg/g; K_L is the adsorption constant (eqm. constant for adsorption process) in L/mg

From plot of C_e/q_e vs. C_e ,slope = 1/ q_m, q_m = 1/slope =monolayer capacity and, intercept = 1/ $K_L q_m$ and K_L = 1/(intercept *q_m) **(Fig. 1.7 and 1.8)**.

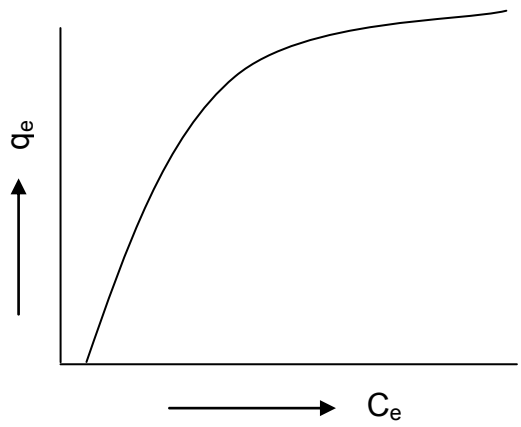

Fig. 1.7. Langmuir plot of q_e vs. equilibrium concentration (C_e).

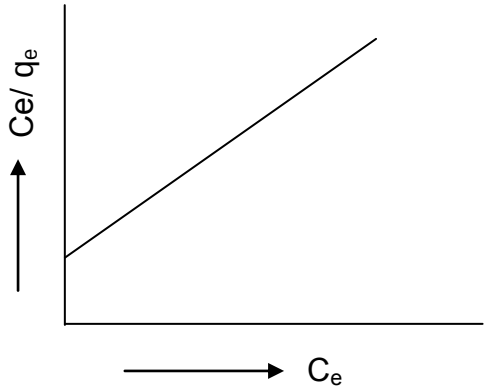

Fig. 1.8. Langmuir-Hinshelwood linear plot of C_e/q_e vs. C_e.

1.15.2. Freundlich adsorption isotherm

The variation of adsorption with concentration of the substance in solution is usually represented by Freundlich isotherm as follows:

$$y = kC^{\frac{1}{n}}$$

or, $$\log y = \log k + \frac{1}{n}\log C$$

1.15.3. BET adsorption isotherm

The theory of Brunauer, Emmett and Teller (BET) is an extension of the Langmuir treatment to allow for multilayer adsorption on non-porous solid surface.

The BET equation is usually written as:

$$\frac{P}{X(P_o - P)} = \frac{1}{X_m C} + \frac{C-1}{X_m C} \cdot \frac{P}{P_o}$$

where, P_o = saturation vapor pressure, X_m = the monolayer capacity and C = exp $^{[(\Delta H2 - \Delta H1) / RT]}$.

1.16. Factors affecting adsorption

1.16.1. Temperature

The level of adsorption at any particular concentration decreases with the increase in temperature; that is the overall process is exothermic. At higher temperature the adsorbed molecules have greater vibrational energies and therefore, more likely to desorb from the surface.

1.16.2. Nature of the solvent

The solvent has an important effect, since it competes with the surface of the adsorbent in attracting the solute. There are three different ways to describe the influence of solvent on adsorption behavior of the solvent (a) its interaction with the solute in solution, (b) its interaction with the adsorbed layer, and (c) its interaction with the solute in the adsorbed layer. However, when the solvent is water, it is worthless to consider the solvent effect.

1.16.3. Particle and pore size

The adsorption efficiency increases as mean diameter of the particle decreases. Large surface area is available for adsorption with the small particles. Another reason is the reduced diffusive path length of the interior of small adsorbent particles and the adsorbate particles require less energy of jump from one active site to another, resulting in higher uptake by the adsorbent.

1.16.4. pH of the solution

The effect of pH is extremely important when the adsorbing species is capable of ionizing in response to prevailing pH. It is well known that substances adsorb poorly when they are ionized. When the pH is such that an adsorb able compound

exists in ionic form, adjacent molecules of the adsorbed species on the adsorbent surface will repel each other to a significant degree, because they carry the same electrical charges. Thus the adsorbing species cannot be packed together very densely on the surface. This is the common observation that non-ionized forms of acidic and basic compounds adsorb much better than their ionized counterparts. The acidic species thus adsorb better at low pH and basic species adsorb better at high pH.

1.17. Adsorption from aqueous solution

Adsorption from solution is much simpler than that of gas adsorption. A known mass of adsorbent is kept in touch with a known volume of solution at a given temperature until there is no further change in the concentration of the supernatant solution. This concentration can be determined by a variety of methods involving chemical or radiochemical analysis such as colorimetry, refraction index, etc. The experimental data are usually expressed in terms of an apparent absorption isotherm in which the amount of solute adsorbed at a given temperature per unit mass of adsorbents calculated from the decreases of solution concentration is plotted against the equilibrium concentration. By analogy with gas adsorption, one might hope to calculate the monolayer capacity, the application of an equation of the individual isotherm has a pattern of a sharp knee followed by a clear plateau; the monolayer capacity is then given by the height of the plateau.

1.18. Theoretical aspects of the analytical techniques

1. 18.1. Scanning electron microscope (SEM) technique

The scanning electron microscope (SEM) uses a finely focused beam of electrons to scan over the area of interest. The beam-specimen interaction is a complex phenomenon. The electrons actually penetrate into the sample surface, ionizing the sample and cause the release of electrons from the sample. These electrons are detected and amplified into a SEM image that consists of Back Scattered Electrons and Secondary Electrons. Since the electron beam has a specific energy and the sample a specific atomic structure, different image will be collected from different samples, even if they have the same geometric appearance. The specimen stage allows movement of the specimen along 5 axes as indicated in **Fig.1.9**. The basic stage is controlled manually by micrometers and screw-type adjusters on the stage door. The motorized stage has motors driving the X, Y, Z and rotation controls, all with manual override. The stage can be tilted over 90^{o}. The tilt axis always intersects the electron optical axis of the column at the same height (10 mm). When the specimen positioned at this height, the specimen can be tilted in the eucentric plane. This means that during tilt, almost no image displacement occurs. The tilting mechanism can be locked for more stability at high magnification.

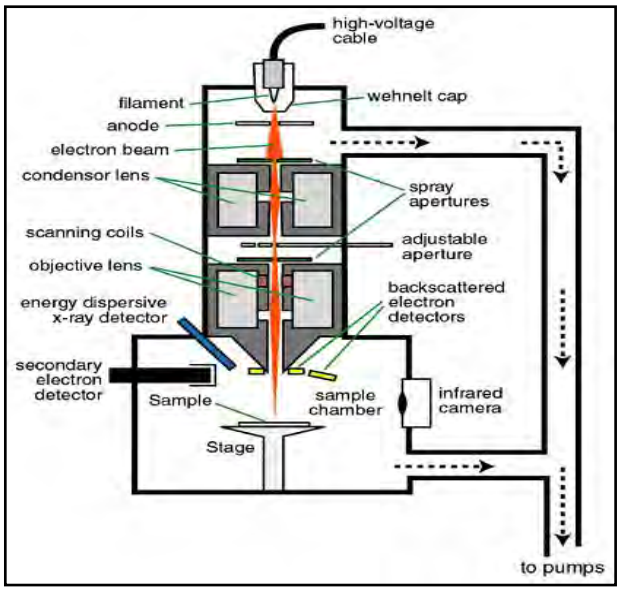

Fig. 1.9. A schematic overview of Scanning Electron Microscope (SEM).

1.18.2. Energy dispersive X-ray analysis (EDX)

EDX is a micro analytical technique that uses the characteristic spectrum of X-ray emitted by the specimen after excitation by high-energy electrons to obtain information about its elemental composition. An electron beam strikes the surface of the sample. The energy of the beam is 120 keV. This causes X-rays to be emitted. The energy of the X-rays emitted depends on the material under examination. The X-rays are generated in the whole section. The detector used in EDX is the Lithium drifted Silicon detector. This detector must be operated at liquid nitrogen temperatures. When an X-ray strikes the detector, it will generate a photoelectron within the body of the Si. As this photoelectron travels through the Si, it generates electron-hole pairs. The electrons and holes are attracted to opposite ends of the detector with the aid of a strong electric field. The size of the current pulse thus generated depends on the number of electron-hole pairs created, which in turn depends on the energy of the incoming X-ray, which depends on the composition of the sample. Thus, an X-ray spectrum can be acquired giving information on the elemental composition of the material under examination. By moving the electron beam across the material an image of each element in the sample can be acquired. If an electron beam strikes the surface X-rays (hv) were emitted, which energy depends on the elemental composition of the sample and Vice versa the energy of the electrons is reduced. Analysis of the X-rays is called EDX.

1.18.3. X-Ray diffraction (XRD)

The X-ray diffraction (XRD) provides substantial information on the crystal structure. This method is applied for the investigation of orderly arrangements of atoms or molecules through the interaction of electromagnetic radiation to give interface effects with structures comparable in size to the wavelength of the radiation. Studies on the crystal structures developed based on methods using single crystals after the discovery of X-ray diffraction by crystals made by the Von Laue. Now a days XRD is used not only for the determination of crystal structure but also chemical analysis, such as chain conformations and packing for polymers,

for stress measurements and for the measurement of phase equilibria and the measurement of particle size, for the determination of the orientation of the crystal and the ensemble of orientations in a polycrystalline material.

X-rays are the electromagnetic radiation whose wavelength is in the neighborhood of 1^{o} A. The wave length of an X-ray is thus of the same order of magnitude as the lattice constant of crystals, and it is this which makes X-rays so useful in structures analysis of crystals whenever X-ray are incident on a crystal surface they are reflected. The reflection abides by the celebrated Bragg's law as given below:

$$2d\,Sin\theta = n\lambda$$

Where, d is distance between crystal planes, θ is the incident angle, λ is the wave length of X-ray and n is a positive integer. The diffracted X-ray may be detected by their action on photographic films or plates or by means of a radiation counter or electronic equipment feeding data to a computer **(Fig 1.10).**

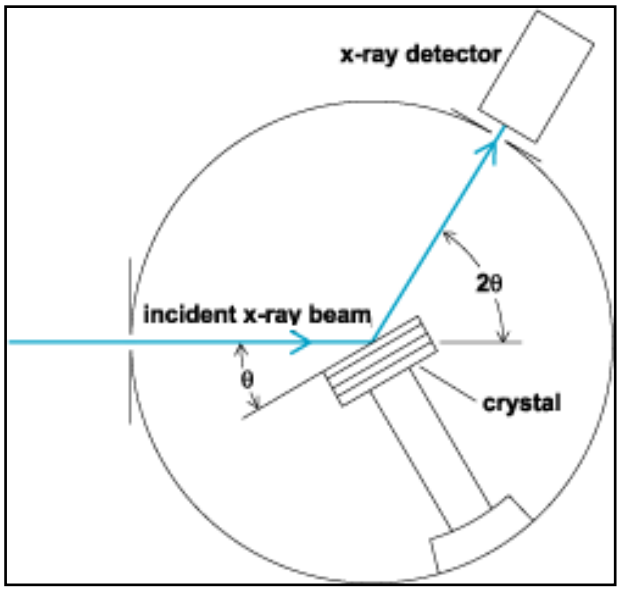

Fig. 1.10. A schematic diagram of XRD instrumentation.

The phase formation of the samples calcined at different temperature is confirmed by X-ray diffraction studies using Bruker X-ray diffractometer with CuK_{α}

radiation (λ =1.54056Å). The lattice parameters are calculated for the cubic and tetragonal phase using following relations.

For cubic phase, $a = d (h^2 + k^2 + l^2)^{1/2}$

Where, a is the Lattice parameter, (h,k,l) = Miller indices, d is the interplanar distance. The crystallite size of Mn-oxides (D_p) can be calculated from the full width at half maxima (β) of the most intense peak by using Scherrer's formula,

$$D_p = 0.9\lambda / \beta \cos\theta$$

Where, symbols have their usual meaning. The X-ray density (theoretical density) can be calculated according to the formula,

$$dx = 8M/Na^3$$

Where, N_a is the Avogadro's number (6.023×10^{23} atom/mole), M is the Molecular mass, and 'a' is the lattice constant which was calculated from the X-ray diffraction pattern.

1.18.4. FT-Infra-red (FT-IR) spectroscopy

Emission or absorption spectra arise when molecules undergo transition between quantum states corresponding to two different internal energies. The energy difference ΔE between the states is related to the frequency of the radiation emitted or absorption by the quantum relation,

$$\Delta E = h\nu$$

Where, h is the Planck's constant and ν is the frequency. Infrared frequencies have the wave length range from 1 μm to 50 μm are associated with molecular vibration and vibration-rotation spectra. Detection of chemical groups and bonding are done by the typical spectra. In oxides surface, the IR absorption spectrum is often surprisingly simple, if one considers the number of atoms involved. This simplicity results first from the fact that many of the normal vibrations have almost the same frequency and therefore appear in the spectrum as one absorption band and second, from the strict selection rules that prevent many of the vibrations from causing absorptions. IR spectrums of all the compounds are recorded on IR spectrophotometer in the region of 4000-400 cm^-

[1]. Samples are introduced as KBr pellets. A block diagram of an IR spectrophotometer is shown in **Fig. 1.11.**

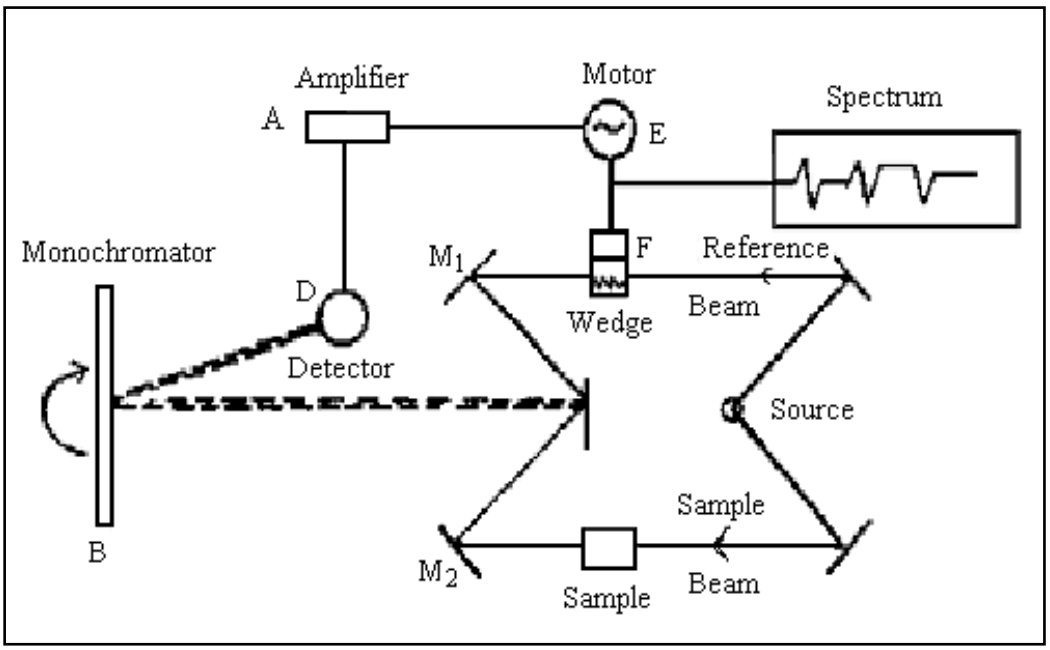

Fig. 1.11. A block diagram of an IR spectrophotometer.

1.18.5. Absorption (UV-Visible) spectroscopy

The greater the number of molecules capable of absorbing light of a given wavelength; the greater will be the extent of light absorption. Furthermore, the more effective a molecule is in absorbing light of a given wavelength, the greater will be the extent of light absorption. From these guiding ideas, the following empirical expression, known as the Beer-Lambert law, which is the basis of spectrometric methods of chemical analysis, may be formulated:

$$A = \log (I_0/I) = \varepsilon c/ \qquad \text{(for a given wavelength)}$$

Where, I_0 is the intensity of the light incident upon the sample cell, I is the intensity of the light having the sample cell, c is the molar concentration of solute, / is the thickness of sample cell (1 cm), ε is the molar absorption coefficient and A is the absorbance. The molar absorption coefficient (ε) is a property of the molecule undergoing an electronic transition and related to transition probability and is not a function of the variable parameters involved in preparing a solution.

The value of ε indicates how intense a given transition is and totally an intrinsic property of the molecule, i.e.

$\varepsilon > 10^4$ is high intensity absorption.

$\varepsilon < 10^3$ is low intensity absorption and

ε =100 to 1000 is forbidden transition.

A block diagram of a double beam UV-Visible spectrophotometer is shown in **Fig. 1.12.**

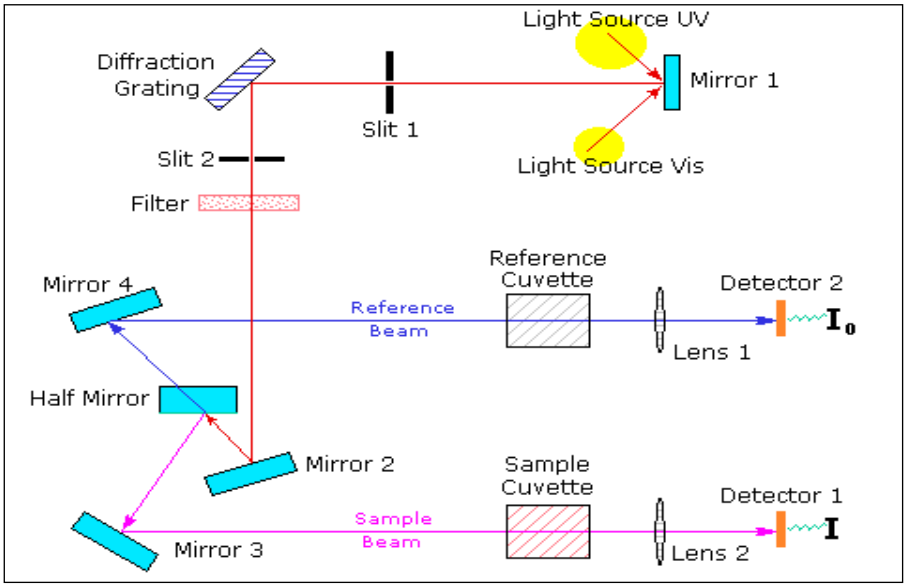

Fig.1.12. A block diagram of a double beam UV-visible spectrophotometer.

1.18.6. Dynamic light scattering (DLS)

Dynamic light scattering is a technique that can be used to determine the size distribution profile of small particles in suspension or polymers in solution. It is a relatively simple spectroscopic technique based on Rayleigh scattering to determine the size of nanoscale objects such as particles, aggregates and large molecules, e.g. polymers and proteins [102-106]. When light hits particles that are small compared to the wavelength of light, a major scattering mechanism observed is elastic Rayleigh scattering. DLS is based on measuring the speed at which particles move under Brownian motion by monitoring the intensity of light scattered by the sample at some fixed angle. Brownian motion causes constructive and destructive interference of the scattered light. Technically, DLS

uses the method of autocorrelation to uncover information contained in the light intensity fluctuations. Autocorrelation measures how well a signal matches a time-delayed version of itself, as a function of the amount of time delay. Quicker autocorrelation function decay indicates faster motion of the particles. The autocorrelation function can be related to the hydrodynamic radius (R_h) of the particles, which is the information of interest, by the Stokes Einstein equation [107]:

$$D = \frac{kT}{6\pi\eta_0 R_h}$$

Where, D is the diffusion coefficient of the molecules, k is Boltzmann-constant, T is absolute temperature and η_0 is the solvent viscosity. Larger particles correspond to slower Brownian motion and slower delays of the autocorrelation function. If the system is monodisperse, the mean effective diameter of the particles can be determined. This measurement depends on the size of the particle core, the size of surface structures, particle concentration, and the type of ions in the medium. Since DLS essentially measures fluctuations in scattered light intensity due to diffusing particles, the diffusion coefficient of the particles can be determined.

DLS software of commercial instruments typically displays the particle population at different diameters. If the system is monodisperse, there should only be one population, whereas a polydisperse system would show multiple particle populations. If there is more than one size population present in a sample then CONTIN analysis must be applied. For more than two populations CONTIN analysis at several scattering angels is required. Periodical DLS measurements of a sample can show whether the particles aggregate over time by seeing whether the hydrodynamic radius of the particle increases. If particles aggregate, there will be a larger population of particles with a larger radius. A schematic set up of a modern DLS instrumentation is shown in **Fig.1.13.**

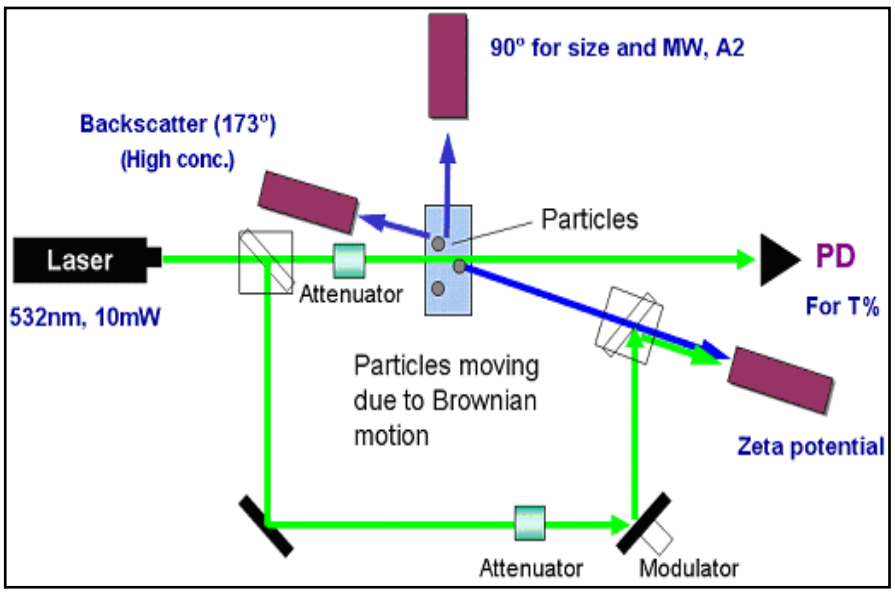

Fig.1.13. A schematic set up of a modern DLS instrumentation.

1.18.7. TG-TDA Analysis

Thermal analysis is a branch of materials science where the properties of materials are studied as they change with temperature. Several methods are commonly used – these are distinguished from one another by the property which is measured:

a) Thermogravimetric analysis (TGA): mass
b) Differential thermal analysis (DTA): temperature difference
c) Dielectric thermal analysis (DEA): dielectric permittivity and loss factor
d) Differential scanning calorimetry (DSC): heat difference
e) Dilatometry (DIL): volume
f) Dynamic mechanical analysis (DMA) : mechanical stiffness and damping
g) Evolved gas analysis (EGA) : gaseous decomposition products
h) Laser flash analysis (LFA): thermal diffusivity and thermal conductivity
i) Thermomechanical analysis (TMA): dimension
j) Thermo-optical analysis (TOA): optical properties.

1.18.7(a). Thermal gravimetric analysis (TGA)

TGA is a method of thermal analysis in which changes in physical and chemical properties of materials are measured as a function of increasing temperature (with constant heating rate), or as a function of time (with constant temperature and/or constant mass loss) [108]. TGA can provide information about physical phenomena, such as second-order phase transitions, including vaporization, sublimation, absorption, adsorption, and desorption. Likewise, TGA can provide information about chemical phenomena including chemisorptions, dessolvation (especially dehydration), decomposition, and solid-gas reactions (e.g., oxidation or reduction) [109-110]. TGA is commonly used to determine selected characteristics of materials that exhibit either mass loss or gain due to decomposition, oxidation, or loss of volatiles (such as moisture). Common applications of TGA are

(i) Materials characterization through analysis of characteristic decomposition patterns,
(ii) Studies of degradation mechanisms and reaction kinetics,
(iii) Determination of organic content in a sample,
(iv) Determination of inorganic (e.g. ash) content in a sample, which may be useful for corroborating predicted material structures or simply used as a chemical analysis.
(v) It is an especially useful technique for the study of polymeric materials, including thermoplastics, thermosets, elastomers, composites, plastic films, fibers, coatings and paints.
(vi) TGA can be used to evaluate the thermal stability of a material. In a desired temperature range, if a species is thermally stable, there will be no observed mass change. Negligible mass loss corresponds to little or no slope in the TGA trace. TGA also gives the upper use temperature of a material. Beyond this temperature the material will begin to degrade.TGA has a wide variety of applications, including analysis of ceramics and thermally stable polymers.

1.18.7(b). Differential thermal analysis (DTA)

DTA is a thermoanalytic technique, similar to differential scanning calorimetry. In DTA, the material under study and an inert reference are made to undergo identical thermal cycles, while recording any temperature difference between sample and reference [111-116]. This differential temperature is then plotted against time, or against temperature (DTA curve, or thermogram). Changes in the sample, either exothermic or endothermic, can be detected relative to the inert reference. Thus, a DTA curve provides data on the transformations that have occurred, such as glass transitions, crystallization, melting and sublimation. The area under a DTA peak is the enthalpy change and is not affected by the heat capacity of the sample. A DTA curve can be used only as a finger print for identification purposes but usually the applications of this method are the determination of phase diagrams, heat change measurements and decomposition in various atmospheres. A modern TGA-DTA system is shown in **Fig.1.14 and 1.15**:

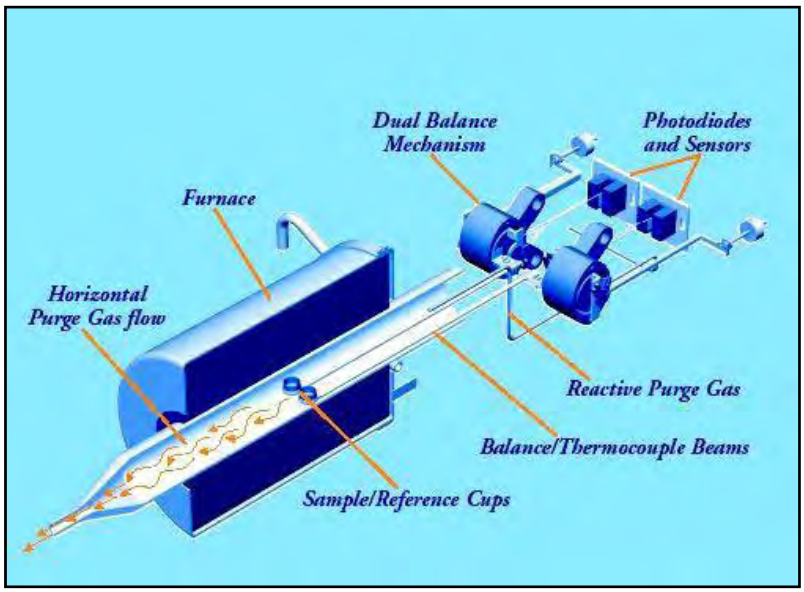

Fig. 1.14. A schematic diagram of a modern TGA-DTA system.

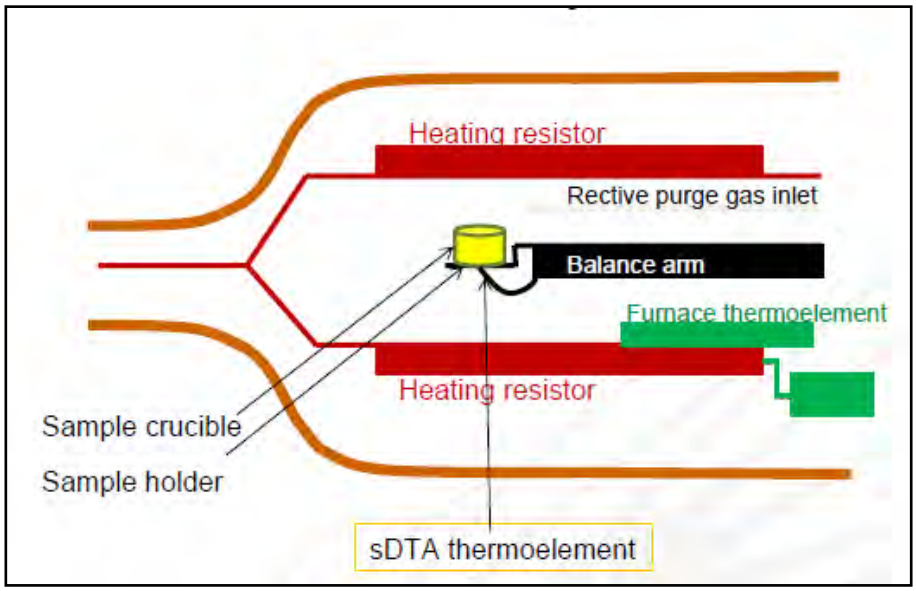

Fig. 1.15. Furnace components of a typical modern TGA-DTA system.

1.19. Point of zero charge (pH_{PZC})

The pH where the net total particle charge is zero is called the point of zero charge (PZC), which is one of the most important parameters used to describe variable-charge surfaces. The pH_{PZC} of solid surface naturally depends on the relative number of each type of grouping and on their respective dissociation constants. It has been found that the point of zero charge is usually not obtained at equal concentration of the positive and negative ions but at a slight excess of one of the ions. The zero point does not necessary occur at neutral pH, but it known to vary with the crystal structure of the solid. For example, alumina is not neutral at pH. The PZC of the oxide may be the most important parameter since it is the pH around which strong buffering effect is observed [117]. The buffering effect is seen through the plateau on a pH final (pH after oxide addition) vs. pH initial graph.

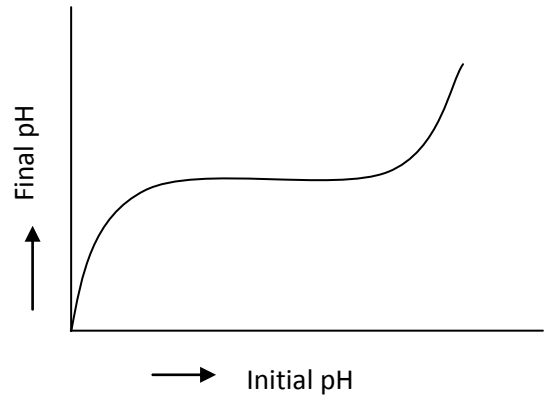

Fig. 1.16: Plot of a pH final (pH after oxide addition) vs. pH initial graph.

The oxide surface becomes protonated (deprotonated) when the initial pH is below (above) the afore-mentioned plateau region. Oxide ions are strong bases. Thus, in aqueous solutions, they become neutralized by water to form hydroxyl groups. The hydroxyl groups on the surface of an amphoteric oxide then become protonated or deprotonated, which leads the solution pH increasing or decreasing. In other words, as oxides in an acidic (basic) pH become protonated (deprotonated) the solution, which supplies (consumes) protons, becomes more basic (acidic). Adsorption is largely depends on the pH of the bulk. If the pH of the bulk higher than pH_{PZC} surface become negative and the lowering of the pH of the bulk than pH_{PZC} surface become positive. This general concept is shown in the diagram **(Fig.1.17).**

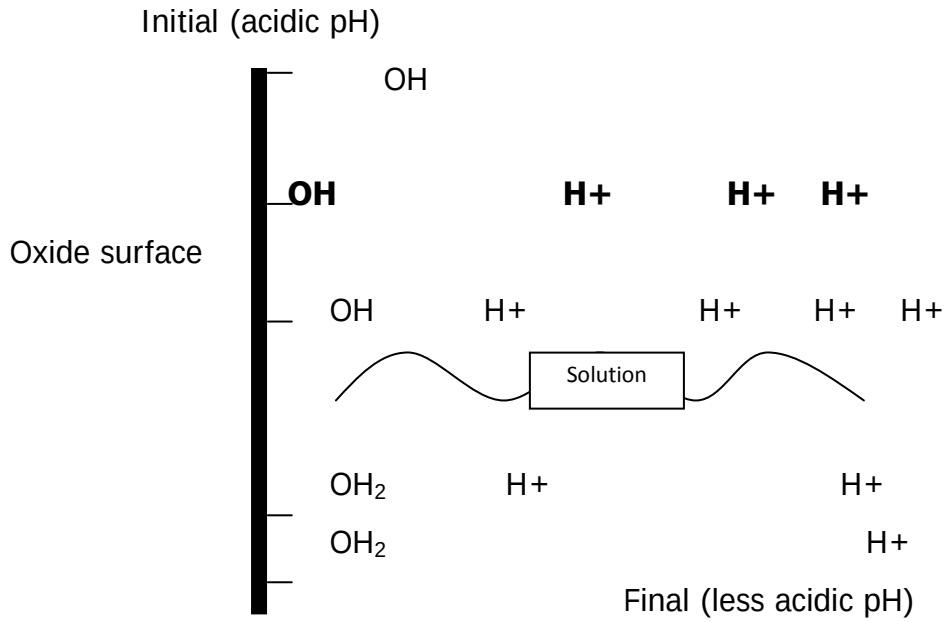

Fig. 1.17: A visual representation of a pH shift.

In solution, when the pH is greater than the PZC, the surface of the oxide is negatively charged and deprotonated. When the pH is less than the PZC, the surface of the oxide is positively charged and protonated. So, oxides that are places in solutions with a pH greater than its PZC will absorb cations and oxides contacted with a solution with a pH less than its PZC will absorb anions. Two important points are to be noted here,

(i) The surface charge is equal to the fraction of positively charged sites minus the fraction of negatively charged sites.

(ii) The electrical double layer consists of a layer of charge on the oxide's particle surface and another layer of opposite charge in the surrounding solution.

1.19.1. Methods for the determination of point of zero charge (PZC)

There are several methods namely:

a) Mass titration;

b) Potentiometric titration;

c) Ion adsorption and

d) Electrophroretic mobility.

1.19.1(a). Mass titration

Mass titration was originally developed for pure metal oxides [118] and later extended so that it can be used also for contaminated samples. The principle of the method is simple; one needs to be added subsequent portions of metal oxide powder to the water or aqueous electrolyte solution, which might be acidified or may contain a base. The pH of the system is changed gradually and approaches a constant value, which is the PZC in the case of pure oxide. If the sample is contaminated, i.e., if it contains a certain portion of acid or base, the final pH is higher or lower than PZC, depending on the type and amount of the acid or base in the powder.

1.20. Surface characterization by adsorption methods

Adsorption methods may be used to provide information about the total surface area of a catalyst, the surface area of the phase carrying the active sites, or possibly even the type and number of active sites. The interaction between the adsorbate and the adsorbent may be chemical (chemisorption) or physical (physisorption) in nature and ideally should be a surface-specific interaction. It is necessary to be aware, however, that in some cases the interaction between the adsorbate and the adsorbent can lead to a chemical reaction in which more than just the surface layer of the adsorbent is involved. For example, when using oxidizing compounds as adsorbate (O_2 or N_2O) with metals such as copper or nickel or sulfides, sub-surface oxidation may occur.

Physical adsorption is used in the BET method to determine total surface areas [119]. Many catalysts comprise an active component deposited on a support. In order to investigate relationships between catalytic properties and the amount of active surface it is necessary to have a means of determining the surface area of the phase carrying the active sites (active phase) in the presence of the support. One has to resort to phenomena specific to the active phase. Chemisorption on the active phase is commonly used for this purpose. Because of its intrinsically specific nature, chemisorption has an irreplaceable role. It should

be recognized, however, that well defined thermodynamic equilibrium physisorption is much more difficult to achieve by chemisorption than with physisorption. Moreover, it does not obey simple kinetics. Empiricism permits the derivation of procedures which give reproducible results, and yield values which are proportional to the true surface area within certain limits. But the real coefficient of proportionality is actually unknown. Different procedures are used, according to UIC nature of the active phase/support system to be characterized, and depending on the choice of adsorbate. Provided standard, reproducible procedures are used, invaluable information can be obtained.

1.21. Measurement of specific surface area by adsorption method

Adsorption measurements have a variety of uses and applications, but perhaps the most important from our point of view is in determining the surface areas of catalysts. Provided the rate of transport of reactants to the surface, and product away from the surface, is faster than the catalyzed reaction, then the observed rate should be proportional to the surface area of the active phase of the catalyst. Adsorption measurement can be performed by two ways,

(1) Gas adsorption measurement.

(2) Dye adsorption measurement.

The surface area of a catalyst could then be determined by either BET or Langmuir adsorption equation depending on which is appropriate for given data.

1.21.1. Gas adsorption measurements

Gas adsorption is accompanied by adsorption of a gas or vapour onto a bare solid surface. The total surface area of the catalyst can determined by adsorption of relatively inert gases like Ar, N_2 etc. at near their condensation temperature, as at such condition adsorption is non-specific and physical in nature. If the catalysts are not susceptible to poisoning by H_2, O_2, CO, NO gases, the specific surface area, i.e. the surface area due to active metal component can be determined by chemisorption of these gases.

1.21.2. Dye adsorption measurements

Dye adsorption technique involves the adsorption of dye molecules from solution onto a solid surface, in particular, dyes such as methylene blue and OG. The method of adsorption of methylene blue in liquid phase for specific surface area determination has been adopted widely for various natural solids: activated carbon, charcoal, silica etc.

1.22. Antibacterial activity of Mn-oxides nps

Bactericidal nanomaterials, particularly metallic nanoparticles, opened a new avenue in medical science. The bactericidal effect of silver nanoparticles on the micro-organisms is very well known. Antibacterial test is accomplished by a method named one of Inhibition Test or Kirby–Bauer Test. It is used clinically to measure antibiotic resistance and industrially to test the ability of solids and textiles to inhibit microbial growth. About a million cells from a single strain are spread over the agar plate using a swab. Then, incubated in the presence of the antimicrobial object (Petri disk). If the bacterial strains are susceptible to the antimicrobial agent, then a zone of inhibition appears on the agar plate and if it is resistance to the antimicrobial agent, then no zone is evident.

Researchers who develop antimicrobial textiles, surfaces and liquids use this test as a quick and easy way to measure and compare levels of inhibitory activity.

1.23. Literature review and aim of the present study

Nano-materials become more and more attractive in recent years, because they possess favorable and enhanced physical and chemical properties. The development of nanoparticles (nps) has been intensively pursued because of their huge fundamental and technological prospects. Manganese oxide (*viz.,* MnO_2 and Mn_3O_4) nps are the technologically important materials with a variety of applications. MnO_2 can be utilized as oxidative catalyst, electrode materials for rechargeable lithium batteries, colorants, corrosion inhibiting agents for paints and water treatment agents [120-122].

Solution-based synthesis and use of metal oxide nanoparticles, however, require special mention due to their low cost, mildness, convenience and use without additional templates and apparatus. In spite of their important applications, there have been only few reports on synthesis of monodisperse manganese oxide nanoparticles [123]. Deogratius Jaganyi et al. [124], have synthesized whisker-shaped MnO_2, via a facile one step solution phase approach, by the reduction of $KMnO_4$ by $Na_2S_2O_3$ solution at room temperature.

Xiujuan Chu et al. [125] have established a chemical coprecipitation route in aqueous solution, without using any templates, catalysts and organic reagents to prepare MnO_2 nps. In this process, $MnSO_4$ were dissolved in distilled water, $KMnO_4$ solution was added slowly with magnetic stirring at a molar ratio of $KMnO_4/MnSO_4$ = 2/3 at room temperature. The resulting black solution was kept at room temperature in air for 24h, then filtered and washed with double deionized water for several times to remove any soluble products. After that, the deposition was dried at 80^0C in air for about 12h.

Hyun-A Choi et al. [126] , have synthesized various MnO_2 morphologies in the forms of nanorods, nanoparticles, and mesoporous MnO_2 structures with interpores or intrapores. They synthesized MnO_2 nanoparticles using a precipitation method based on $KMnO_4$ and $Mn(OAc)_2$ and investigated the effect of calcinations on particle size. They also fabricated the interpore structure by slowly dropping 0.5 M $KMnO_4$ solution onto a CCl_4/H_2O interface [127], whereas the intrapore structure was obtained using a reduction method using $KMnO_4$ and ascorbic acid as the reducing agent [128] which involved mixing $KMnO_4$ with a solution of ascorbic acid and aging for 10 min under continuous stirring at room temperature.

DeGuzman et al. [129] prepared fibrous α-MnO_2 through redox reactions between $KMnO_4$ and $MnSO_4$. However, some minor differences in the morphology of final products have been observed as specific reaction conditions were being altered slightly [130]. Parameters such as temperature, time and capping

molecules can influence the growth of nanocrystals under nonequilibrium kinetic growth conditions in the solution-based approach [131].

Suh Cem Pang, et al. [132] reported the controlled synthesis of various MnO_2 nanostructures via a facile and mild hydrothermal route without using any physical template and addition of any surfactant. They synthesized both δ-MnO_2 and α-MnO_2 nanostructures based on the hydrothermal reaction of $MnSO_4$ and $KMnO_4$ in aqueous medium at mild temperatures. They also investigated the effects of hydrothermal synthesis conditions on the evolution of structural morphology and phase transformation of MnO_2 nanostructures.

Aye Aye Hlaing et al. [133] reported a novel and simple approach to synthesize α-MnO_2 single-crystal nanorods by hydrothermal homogeneous precipitation by mixing $MnSO_4$ (0.01M) and $KMnO_4$ (0.02M) solution and dissolving at room temperature in 70 mL of H_2O_2 solution (1:1 molar rations of H_2O_2 to water) which provides a substantial amount of O_2 for rapid redox reaction by magnetic stirring to form a homogeneous solution.

Danisa Tabassum et al. [134] also prepared black MnO_2 by mixing $KMnO_4$ and $MnSO_4$ stoichiometrically ($KMnO_4/MnSO_4$ = 2/3) in aqueous solution at room temperature and brown MnO_2 from a mixture of $KMnO_4$ and NH_4OH solution at 90^0C.

Tran Hong Con et al. [135] prepared nano dimensional MnO_2 by oxidation-reduction reaction by slowly adding of $MnSO_4$ ($3x10^{-2}$ M) water – ethanol solution into the $KMnO_4$ ($2x10^{-2}$ M) solution with the same volume at room temperature.

In the present study, attempt has been made for a facile one-step solution phase synthetic approach of MnO_2 nanoparticles without any template or stabilizing agent by the reduction from a system containing $KMnO_4$ and $MnSO_4$ solutions at room temperature. The resulting MnO_2 sol was taken under sonication to ensure dispersion of MnO_2. The dispersed phase was washed thoroughly followed by drying before its any use.

On the other hand, Mn_3O_4 has gained significant attention due to its wide range of applications such as high density magnetic storage media, catalysts,

molecular adsorption, electrochemical materials and solar energy transformation [136-138]. Due to their small size, *nps* exhibit novel material properties that are significantly different from those of their bulk counterparts.

Yang et al. [139] synthesized Mn_3O_4 polyhedral nanocrystals by a microwave assisted technique using an aqueous solution containing $Mn(OCOCH_3)_2$ and hexamethylenetetramine.

Chen et al. [140] synthesized crystalline Mn_3O_4 nanoparticles of different morphologies using liquid homogeneous precipitation with $MnCl_2$, H_2O_2, NaOH and sodium dodecylbenzene sulfonate surfactant as reactants.

Zhang et al. [141] prepared crystalline Mn_3O_4 nanopowders by solvothermal treatment of γ-MnOOH nanowires in ethylenediamine and ethylene glycol.

Gibot et al. [142] prepared Mn_3O_4 nanoparticles in aqueous solution using $KMnO_4$ and hydrazine as a reducing agent.

Wang et al. [143] synthesized single-crystal Mn_3O_4 nanorods by a method starting from $MnCl_2$ and NaOH as a precipitating agent.

Vázquez-Olmos et al. [144] reported one-step synthesis of Mn_3O_4 nanoparticles starting from Mn(II) acetate in aqueous dimethyl formamide.

Ozkaya et al. [145] synthesized Mn_3O_4 nanoparticles by a precipitation method based on the oxidation of manganese sulfate and hydrolysis with NaOH and concentrated NH_3 solution.

Hu et al. [146] synthesized monodisperse Mn_3O_4 particles by γ-irradiation of manganese sulfate in the presence of a cationic surfactant.

K. Usha et al. [147] prepared Mn_3O_4 nanoparticle by mixing Mn(II) acetate and urea in 1:3 molar ratio in ethylene glycol and kept in a domestic microwave oven. The colloidal precipitate obtained was cooled and washed several times with double distilled water and then with acetone to remove the organic impurities present, if any. The product was dried in atmospheric air and collected as the yield.

Masoud Salavati-Niasari et al. [148] have synthesized Mn_3O_4 nanoparticles by thermal decomposition of a [bis(salicylidiminato) Mn(II)] complex as a precursor without the presence of a catalyst.

Shafiul Azam et al. [67] have prepared Mn_3O_4 nanoparticles by forced hydrolysis of Mn(II) acetate solution (0.4M) heating in an oven at 80^0C for 2h. The resulting brown dispersed product, Mn_3O_4, was then quenched in cool water and recovered by centrifugation. The product was then washed several times with double distilled water and dried in air in an oven at 40 ^{0}C.

In the present study, Mn_3O_4 nps was prepared by forced hydrolysis of aqueous Mn(II) acetate solution by heating its aqueous solution. As expected, the formed Mn_3O_4 nps was then quenched in cool water and recovered by centrifugation. The product was washed several times before drying the nps under heating.

Mixed metal oxides (MMO) are used because overall properties of the MO are superior to those of the individual oxide. Preparation of new mixed metal oxides of both industrial and synthetic importance has become a routine work in advanced material laboratories. Extensive research work has been carried out in the synthesis and characterization of metal oxide and mixed metal oxides type semiconductor photo catalyst and adsorbent as they have effective capability to destroy toxic and hazardous organic substances. The wide applications of MnO_2 and Mn_3O_4 made us interested to develop a Mn-oxide *nano*-matrix containing MnO_2 and Mn_3O_4 *nps*.

Jr-I. Lai, et al. [149] have studied on mixed Fe-Mn oxide nanoparticles. They have discussed sonochemical synthesis and characterization of nanosized Mn-Fe oxide powder by FT-IR spectroscopy, X-ray diffraction, scanning electron microscopy and transmission electron microscopy and all physical measurements supported compete mixing of the Fe(III) and Mn(III) ions in the mixed oxide amorphous samples.

J. Zhou, et al. [150] has worked on Nanosized Ni-Mn oxides prepared by the citrate gel process and performances for electrochemical capacitors.

C. L. Shope, et al. [151] published research work on the influence of hydrous Mn–Zn oxides on diel cycling of Zn in an alkaline stream draining abandoned mine lands.

AZURDIA Jose A, et al. [152] has studied systematic synthesis of mixed-metal oxides in NiO-Co_3O_4, NiO-MoO_3, and NiO-CuO systems via liquid-feed flame spray pyrolysis (LF-FSP).

Samira Saimuma et al. [153] prepared Fe-Si mixed oxide in a reactor which involved the simultaneous generation of hydrous ferric oxide (FeOOH) and silica sol. A mixture containing sodium silicate (Na_2SiO_3) and sodium carbonate (Na_2CO_3) was kept under stirring. After that, $Fe(NO_3)_3$ was added in the former mixture also under stirred condition to yield a gel of Fe-Si components at an appropriate pH. The Fe-Si slurry was then allowed to age for a few hours. The slurry was then washed and separated by filtration. Finally, it was dried at a temperature of 200 °C for 3 hours in an oven.

Roushown Ali et al. [154] studied the selective oxidation of benzylic alcohols using copper-manganese mixed oxide nanoparticles as catalyst. In this case, the Cu-Mn mixed oxide (Cu/Mn=1:2) nanoparticles were prepared by co-precipitation method using the required amount of precursors $Cu(NO_3)_2.3H_2O$, $Mn(NO_3)_2.4H_2O$ and Na_2CO_3.

Gong Zhou et al. [155] have studied Ce–Mn mixed oxides for oxidation catalysis. The pure Ce-Mn oxides were prepared by dissolving stoichiometric amounts of $Ce(NO_3)_3$ and $Mn(NO_3)_2$ in distilled water and then mixed with aqueous citric acid to produce a solution with a citric acid: metal-ion ratio of 2:1. After vigorous stirring for 1 h at room temperature, the water was removed by evaporation with mild heating. The resulting solids were calcined in air at 973 K for 5 h to produce the mixed oxide solutions.

Hansung Kim et al. [156] prepared Mn/Pb and Mn/Ni mixed oxide at ambient temperature by reduction of $KMnO_4$ with either lead(II) acetate-manganese acetate or nickel(II) acetate-manganese acetate reducing solutions, respectively [157].

Nisha J tharayl et al. [158] synthesized nanoparticles of Co-Mn oxide by chemical coprecipitation method by decomposition of $CoCl_2$, $MnCl_2$ and Na_2CO_3 using ethylene diamen tertra acetic acid (EDTA) as a capping agent [159].

However, work on MnO_2-Mn_3O_4 *nano*-matrix has not been reported so far. Thus, in the present work, attempt was made to prepare MnO_2-Mn_3O_4 *nano*-matrix by a simple chemical route under ambient conditions. This low temperature synthetic route, based on the simple reaction with no participation of catalysts or templates and requiring no expensive and precise equipment, ensures higher purity of the products, greatly reduces the production cost, and thus offers great opportunity for industry scale-up preparation of nanostructure materials.

From the early days of using bone charcoal for decolorization of sugar solution and other foods, to today's thousand of applications, the adsorption phenomenon has become a useful tool for purification and separation technologies. Adsorption phenomena are operative in most natural, physical, biological and chemical systems and adsorption operations employing solids such as activated carbon, alumina, silica gel and zeolite are so far used widely in industrial applications and for purification of waters and wastewater [160-162].

A large specific surface area is preferable for providing large adsorption capacity. As a result, presently, a great deal of attention has been focused on the search for new materials with better adsorption capacity [163-166]. In catalysis, alloys or multi-component system often perform better than its pure or single component [167-168]. Like catalysis, adsorption is also a surface property. Thus, employment of a binary or multi component surface for adsorption seems to be interesting to be investigated.

Wen-Hui Kuan et al. [169] studied kinetic modeling for microwave-enhanced degradation of methylene blue Using manganese dioxide.

Lili Zhang et al. [170] Decolorization of methylene blue in layered manganese oxide suspension with H_2O_2.

Shafiul Azam et al. [67] studied the decolorization of methylene blue (MB), procion red (PR) and a dye contaminated real sample (dye effluent of a local

textile industry) as the model organic contaminants was investigated using Mn_3O_4 as an oxidant.

In our study, chemical properties of the nps were tested by the oxidative decolorization of MB and OG at different pH. The extent of dye removal was be monitored by UV-Vis spectroscopic method.

MB was chosen in this study because of its strong adsorption onto solid and recognized usefulness in characterization of catalyst. Also in aqueous solution it shows distinct absorption band near uv-visible region (400-800 nm) of the electromagnetic radiation with absorption maxima at 664 nm.

Orange G (OG), a typical azo dye in textile wastewaters, has been the subject of intense investigations [171]. However, the information about OG degradation by the manganese oxide is still limited. In this study, the kinetics of OG degradation will be elucidated based on the experimental data. Furthermore, the influence of some important reaction conditions such as pH of solutions, dosages of Mn-oxide was investigated.

A common features that metal oxide nanoparticles exhibit is their antimicrobial behavior against pathogenic bacteria. Sahin, E. et al. [172], studied Antibacterial activity against Escherichia coli and characterization of ZnO and $ZnO–Al_2O_3$ mixed oxide nanoparticles.

Ameer Azam et al. [173] have studied a comparative studyof antimicrobial activity of metal oxide nanoparticles against Gram-positive and Gram-negative bacteria.

R. Gokulakrishman et al. [174] studied in vitro antibacterial potential of metal oxide nanoparticles against antibiotic resistant bacteria pathogens. However, antibacterial acitivity of MnOOH has not yet been studied.

Therefore, in this dissertation, the pathogenic experiments were performed following the standard conventional method [175] by treating the MnO_2, Mn_3O_4 and Mn-oxide nps suspension to various pathogenic organisms at different pH. Bacteria for various diseases were grown onto a Petri dish to find out active zone

of inhibition by applying a standard reference and the Mn-oxide *nps* that proposed in the present work.

Prime aim of this work was to design a mixed matrix based on Mn-oxide *nps* and studies on its characterization and activity, particularly towards oxidative decolorization and pathogenic accomplishments. The possible outcome of this study may include:

i) A facile route, be its chemical, for the generation of Mn-oxide nps was established.
ii) A protocol for controlling the particle size and distribution of nps was identified.
iii) Organizing variety of material functionalities in a single matrix was opened.
iv) Sciences (*e.g.*, physico-chemical behaviours) were revealed differences, from its constituent Mn-oxide.
v) Information about the surface morphology and surface charge of the mixed oxide adsorbent.
vi) The functionalities of the *nps* would be able to affect the various activities and uses of Mn-oxide nps.
vii) To compare the decolorization capacity of MB and OG dyes by using MnO_2, Mn_3O_4 and MnOOH.
viii) Batch experiments to remove MB and OG dyes from water under various parameters such as pH, concentration, dose etc.
ix) The evaluation of kinetic parameters for the decolorization of MB and OG by MnO_2, Mn_3O_4 and MnOOH surface.
x) Antimicrobial activity of synthesized nanomaterials.

CHAPTER II

EXPERIMENTAL

CHAPTER - II
EXPERIMENTAL

2. Chemicals and Instruments

2.1. Chemicals

The chemicals and reagents used in the present research work were analytical grade and used without further purification. Doubly distilled water was used as solvent to prepare most of the solution of this work.

(i) Potassium permanganate [E. Merck, Germany]

(ii) Manganese sulphate.$2H_2O$ [Merck, India]

(iii) Manganese (II) acetate.$4H_2O$ [Merck, India]

(iv) Hydrochloric acid [E. Merck, Germany]

(v) Sodium hydroxide [E. Merck, Germany]

(vi) Sulphuric Acid [Uni-chem, China]

(vii) Absolute Ethanol [E. Merck, Germany]

(viii) Phosphoric Acid [Merck, India]

(ix) Acetone [Merck, India]

(x) Methylene Blue [E. Merck, Germany]

(xi) Orange Green [E. Merck, Germany]

(xii) Dimethyl Sulphoxide (DMSO) [E. Merck, Germany]

(xiii) Muller Hinton Arar broth [Aldrich].

2.2. Instruments

Analysis of the synthesized samples of manganese oxides performed in this work employed the following instruments:

(i) UV-visible spectrophotometer [UV-1601 PC, Shimadzu, Japan]

(ii) FT-IR spectrophotometer [Perkin- Elmer, UK]

(iii) Scanning electron microscope [Philips XL30, Holland]

(iv) X-ray diffractometer [Philips, Expert Pro, Holland]

(v) pH meter [Hanna, pH 209, India]

(vi) Centrifuge machine [Hermle, 2200 A, Germany]

(vii) Shaker machine [Heidolph Unimex 1010]

(viii) 100 mesh sieve [Endecotls test sieves limited, England]

(ix) Digital balance, [FR-200, Japan]

(x) Electrical Furnace [DK, Chino, England]

(xi) Microburette [China]

(xii) DLS Analyzer [Malvern]

(xiii) Electrical hot plate

(xiv) TG-DTA analyzer [Hitachi, TG-DTA-7200]

2.3. Bacterial Strains

Three bacterial strains *viz., Vibrio Cholera, E. Coli and S. Aureous* were obtained from ARI laboratory, ICDDR,B, Dhaka, Bangladesh.

2.4. Synthesis of Mn-oxides nanoparticles (nps)

2.4.1. Nanoparticle MnO_2 Synthesis

Black MnO_2 nps was prepared by reduction from a system containing aqueous $KMnO_4$ and $MnSO_4$ solutions by co-precipitation method. Details are described in result and discussion section **3.1.1.**

2.4.2. Nanoparticles Mn_3O_4 (husmannite) synthesis

Brown Mn_3O_4 nps was prepared by forced hydrolysis of Mn(II) acetate by heating its aqueous solution at 80^0C. Details are described in result and discussion section **3.1.2.**

2.4.3. Mixed manganese oxide *nano*-matrix synthesis

Dark steel grey mixed manganese oxide *nano*-matrix (identified experimentally as manganite, γ−MnOOH nps) was synthesized by incorporating MnO_2 sol into Mn(II) acetate solution at 80^0C. Details are described in result and discussion section **3.1.3.**

2.5. Characterization of synthesized nanomaterials

2.5.1. FT-IR spectral analysis

FT-IR study was used to indicate the vibrational modes in the samples. The FT-IR spectra were recorded using Perkin Elmer FT-IR in Material Chemistry Research Lab, University of Dhaka using KBr pellets. FT-IR spectra of all the dried samples of as synthesized MnO_2, Mn_3O_4 and γ−MnOOH, were recorded on an IR spectrometer in the region of 4000-400 cm^{-1} by using KBr pellets. IR spectra of the solid samples were frequently obtained by mixing and grinding a small amount of materials with dry and pure KBr crystals. Thorough mixing and grinding were done in a mortar by a pestle. The powdered mixture was then compressed in a metal holder under a pressure of 8-10 tons to make a pellet. The pellet was then placed in the path of IR beam for measurements. The spectra were presented in **Fig. 3.1, 3.2 and 3.3** respectively.

2.5.2. X-ray Diffraction (XRD) analysis

The crystalline nature of the samples was confirmed by XRD analysis using CuK_a source and at a scan rate of 1^0/min in SCSIR and BAEC Lab, Dhaka. As synthesized MnO_2, Mn_3O_4 and γ−MnOOH were analyzed for their X-ray diffraction pattern in the powder state. The powder samples were pressed in a square aluminum sample holder (40 mm × 40 mm) with a 1 mm deep rectangular hole (20 mm × 15 mm) and pressed against an optical smooth glass plate. The upper surface of the sample was labeled in the plane with its sample holder. The sample holder was then placed in the diffractometer. The spectra were presented in **Fig. 3.4, 3.5 and 3.6** respectively**.**

2.5.3. Scanning electron microscopy (SEM) analysis

The surface and structural morphologies of synthesized MnO_2, Mn_3O_4 and γ−MnOOH were studied by SEM in Deptt. of Glass and Ceramics, BUET. Samples were dispersed on a conducting carbon glued strip. The sample-loaded strip was

then mounted to a chamber that evacuated to ~ 10^{-3} to 10^{-4} torr and then a very thin gold layer (~ few nanometers thick) were sputtered on the sample to ensure the conductivity of the sample surface. The sample was then placed in the main SEM chamber to view its surface. The system was computer interfaced and thus provides recording of the surface images in the computer file for its use as hard copy. The spectra were presented in **Fig. 3.7, 3.8 and 3.9** respectively**.**

2.5.4. Electron Diffraction X-ray (EDX) analysis

Elemental analysis of the as-synthesized MnO_2, Mn_3O_4 and γ−MnOOH nps was performed by EDX spectra in Deptt. of Glass and Ceramics, BUET. The dried powders were dispersed on a 1 cm × 1 cm conducting steel plate. The still plates were then placed on a conducting carbon glued strip and a very thin gold layer was sputtered on the sample to ensure the conductivity of the sample surface. The sample was then placed in the main SEM chamber integrated with the EDX machine. The spectra were presented in **Fig. 3.10-14** respectively**.**

2.5.5. Dynamic light scattering (DLS) analysis

To determine hydrodynamic particle size of as synthesized MnO_2, Mn_3O_4 and γ−MnOOH nps, DLS data was taken over time using water as dispersant (RI= 1.333) in Material Chemistry Research Lab, University of Dhaka. The nanoparticles sample (typical concentrations are 0.5-2.0 mg/mL) was dissolved or suspended in water and fill it into a micro glass cuvette with round aperture (cell volume 10-20 µL) at 25^0C with count rate 144.8 kpcs. Then the hydrodynamic radius and polydispersity index of the sample molecules was determined. All experiments were performed in duplicate and repeated three times. Typical spectra are presented in **Fig. 3.15, 3.16 and 3.17** respectively**.**

2.5.6. TG-DTA analysis

In order to examine the thermal stability of as synthesized dry nanoparticles, thermal gravimetric (TG) and differential thermal analyses (DTA) were carried out between 25 and 800^0C in nitrogen atmosphere at the heating

rate of 10^0C/min in Material Chemistry Research Lab, University of Dhaka. Thermal analysis of the different compositions of the as-synthesized MnO_2, Mn_3O_4 and γ−MnOOH nps was carried out from the curves of TG-DTA. Different kinds of thermodynamic and kinetic parameters were determined from the plots of TG-DTA curves. Spectra are presented in **Fig. 3.18, 3.19 and 3.20** respectively.

2.5.7. Determination of point of zero charge

The point of zero charge (pH_{PZC}) of solid substance means the pH at which the positive and negative charge in the surface is equal. To determine the point of zero charge of Mn-oxide, the experiment was done in the following way: Exactly 0.005 g of Mn-oxide was taken in four different reagent bottles. Then 1 × 10^{-1} M NaCl solution was added to each bottle. The sample solution was agitated for 24.0 hours at low speed in a shaker. Then, the suspensions were observed in each bottle. Two bottles of them were titrated directly with 0.05 M NaOH using microburette (± 0.01 mL). The pH values were noted carefully after addition of each drop of titrant (alkali). Contents of other bottle were filtered with sintered crucible and the supernatant thus obtained was titrated with 0.05 M NaOH. The experiments were carried out in the same way for the 1× 10^{-2} M and 1× 10^{-3} M NaCl solutions respectively. Similar experiments were done using MnO_2 and Mn_3O_4 nps.

2.6. Oxidative decolorization of dyes by as-synthesized Mn-oxide nps

2.6.1. Adsorbate

A cationic dye, methylene blue, having molecular formula $C_{16}H_{18}N_3SCl.2H_2O$ and molecular mass as 355.89 g mol^{-1} was chosen as adsorbate. The MB was chosen in this study because of its known strong adsorption onto solids. In some experiments an anionic dye orange G was also used as adsorbate.

2.6.2. Adsorbent

Manganite, γ−MnOOH nps, which were synthesized from Mn(II) acetate solution incorporating MnO_2 sol was selected as an adsorbent to study MB and OG decolorization from aqueous solution. In some experiments MnO_2 and Mn_3O_4 nps were also used as adsorbent to compare decolorization capacity among these three Mn-oxides.

2.6.3. Decolorization of MB and OG using MnO_2 and Mn_3O_4 and γ−MnOOH nps

2.6.4. Preparation of dye solution

2.6.4(a). Preparation of MB (cationic dye) stock solution

Methylene blue (MB) (molecular mass=355.89 $gmol^{-1}$) was used in this study as an environmental pollutant. Stock solutions of MB dye were prepared by dissolving the required amount of MB in distilled water. Batch experimental solutions were obtained by diluting the dye stock solutions in accurate different initial concentrations. Calibration curves were prepared by serial dilutions (0.2 to 1.5×10^{-5} M). Typically, 1×10^{-3} M MB solution was prepared by dissolving 0.036g of solid MB in 100 mL double distilled water which was used as stock MB solution. Some solution having different concentrations was prepared simply by diluting the stock MB solution.

2.6.4(b). Preparation of OG (anionic dye) stock solution

A stock solution of OG (molecular mass is 452.38 $gmol^{-1}$) 1×10^{-3} M was prepared by dissolving 0.05 g of solid OG in 100 mL double distilled water. The experimental solutions were obtained by diluting the dye stock solution in accurate proportions to required initial concentrations.

2.6.5. Determination of the concentration of dye solutions

Concentration of the dye solution was measured spectroscopically by a double beam UV-vis spectrophotometer. The UV-vis spectral analysis of the sample solutions was employed a double beam spectrophotometer. Adsorption of the dyes was also studied spectroscopically by following the spectral change.

2.6.6. UV-visible spectrum of MB

The absorption spectrum of $1.0x10^{-5}$ M MB solution at pH = 6.99 is presented in **Fig.2.1**. The spectrum showed an absorption maximum at 664 nm which indicated the λ_{max} of MB.

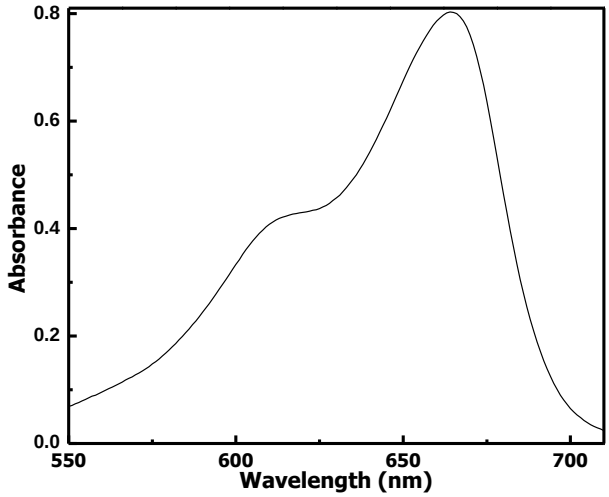

Fig.2.1: UV-spectrum of $1.0x10^{-5}$ M MB solution using water as reference.

2.6.7. UV-visible spectrum of OG

The UV-visible spectrum of $1x10^{-5}$ M OG at pH=6.92 is presented in **Fig.2.2**. The spectrum showed a typical band at 477 nm.

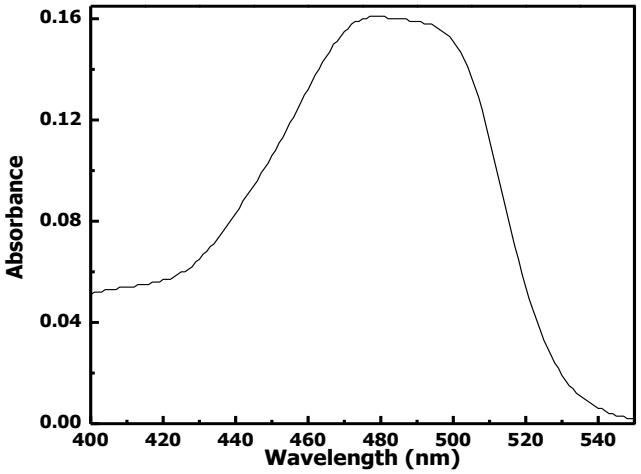

Fig. 2.2: Spectrum of an aqueous solution of 1.0 $\times 10^{-5}$ M OG at pH 6.92.

2.6.8. Determination of molar absorption co-efficient (ε) of MB

For this purpose, different concentration of MB solution was prepared as given in the **Table 2.1**. The corresponding absorbance of the MB solutions was then determined by the spectrophotometer (**Fig.2.3**). The absorbance values are depicted in table too. A plot of absorbance vs. MB concentration yielded a straight line passing through the origin which has well verified the Beer-Lambert law (**Fig.2.4**). For the slope of the line, the molar absorption co-efficient (ε) was calculated as below

$$A = \varepsilon C/$$

The molar absorption co-efficient (ε) was found to be under the experimental condition employed 77,449 L mol^{-1} cm^{-1}.

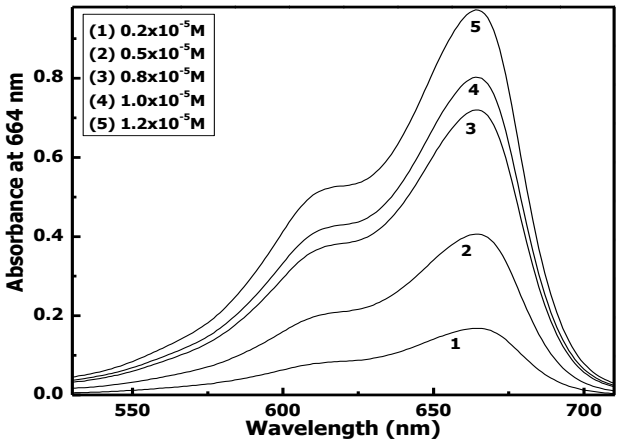

Fig. 2.3: UV-spectrum of MB solution at different concentrations using water as reference.

Table 2.1: Absorbance of MB solution at different concentrations

Reference: Water λ_{max} for MB Solution: 664 nm

Temperature: 28°C pH: 7.94

Run No	Concentration of MB $\times 10^5$ (mol dm^{-3})	Absorbance at 664 nm	molar absorption co-efficient (L $mol^{-1}cm^{-1}$)
1	0.2	0.168	
2	0.5	0.406	
3	0.8	0.720	77,449
4	1.0	0.803	
5	1.2	0.973	
6	1.5	1.168	

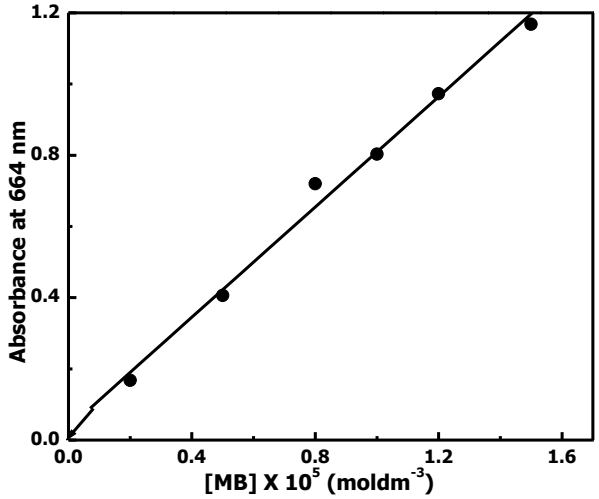

Fig.2.4: Determination of molar absorption coefficient of MB solution at 664 nm.

2.6.9. Determination of molar absorption co-efficient (ε) of OG

For this purpose, different concentration of MB solution was prepared as given in the **Table 2.2**. The corresponding absorbance of the OG solutions was then determined by the spectrophotometer. The absorbances at 477 nm values are depicted in table too. A plot of substrate vs. OG concentration is presented in the **Fig. 2.5**. The result produced a straight line passing through the origin which has well verified the Beer-Lambert law. For the slope of the line, the molar

absorption co-efficient was calculated as below the molar absorption co-efficient (ε) was found to be 16,168 L $mol^{-1}cm^{-1}$ under the experimental condition employed.

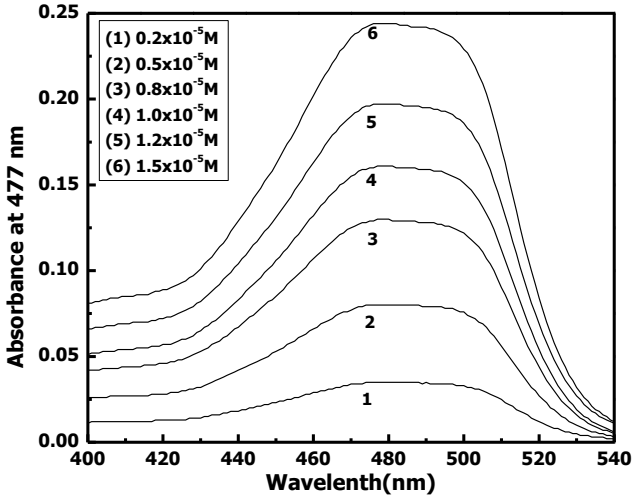

Fig.2.5: Spectrum of OG solution at different concentrations using water as reference.

Table 2.2: Absorbance of OG solution at different concentrations

Reference: Water λ_{max} for OG Solution: 477 nm

Temperature: 28°C pH: 8.27

Run No	Concentration of OG $\times 10^5$ (mol dm^{-3})	Absorbance at 477 nm	Molar absorption co-efficient (L $mol^{-1}cm^{-1}$)
1	0.2	0.035	
2	0.5	0.080	
3	0.8	0.130	16,168
4	1.0	0.161	
5	1.2	0.197	
6	1.5	0.244	

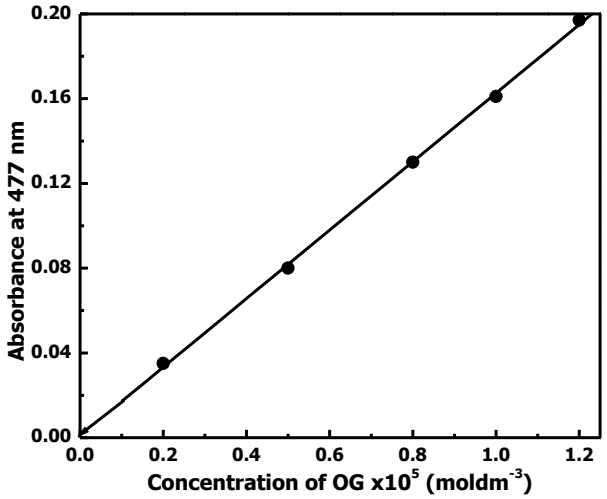

Fig.2.6: Determination of molar extinction coefficient of OG at 477 nm.

2.7. Decolorization kinetic experiments

Kinetic studies of decolorization were carried out at various concentrations of the MB and OG wherein the extent of adsorption was investigated as a function of time. For kinetic studies, solutions of (5-40) $x10^{-6}$ mol L^{-1} MB and OG, as the initial concentration each, were treated with 0.02 g Mn-oxide nps at a constant temperature of 300 K. The mixtures were then subjected to agitation using shaker incubator at 300 rpm for 3h. The working pH was that of solution and but in some cases pH of dye solution was controlled. After a definite interval of time (10, 15, 20, 30, 60, 120, 180, 240, 300 min) each bottle was withdrawn from the shaker and after centrifugation, the left out concentration in the MB and OG solution was estimated. Then, the amount of adsorbed at time t, q_t (mg/g), was calculated by

$$q_t = \frac{V\left(C_0 - C_t\right)}{W}$$

Where, C_0 and C_t are initial concentration, concentration at any time t of dye solution (mol/L), respectively, q_t is the amount of dye adsorbed onto Mn-oxide (mg/g), V is the volume of the solution (L), and W is the mass of adsorbent Mn-oxide (g).

2.8. Decolorization Equilibrium Experiments

For equilibrium studies, the batch technique was used because of its simplicity. In batch adsorption experiments, certain amounts of adsorbent Mn-oxide were added into several 50 mL bottles, each containing solution of MB and OG dyes with known concentration and pH. Then, the bottles were stirred at 300 rpm for 180 min using orbital shaker at room temperature. During this period, adsorption of the dye took place onto the Mn-oxide surface. After a definite interval of time, each bottle was withdrawn from the shaker. The supernatant of the bottle was transferred and centrifuged repeatedly until a clear liquid was obtained. The absorbance of the clear solution was measured by monitoring the absorbance changes at a wavelength of maximum absorbance (λ_{max} = 664 nm) for MB dye and at 477 nm for OG dye. The amount of dye uptake onto Mn-oxide at any time (q_t) was calculated using the mass balance equation:

$$q_t = \frac{V\left(C_0 - C_t\right)}{W}$$

At equilibrium $q_t = q_e$ and $C_t = C_e$; therefore, the amount of adsorbed dye (q_e) was calculated from

$$q_e = \frac{V\left(C_0 - C_e\right)}{W}$$

The dye percent removal (%) can be calculated using the following equation

$$Removal\% = \frac{\left(C_0 - C_t\right)}{C_0} \times 100$$

Where, C_0, C_t and C_e are initial concentration, concentration at any time t and equilibrium concentrations of dye solution (mg/L), respectively, q_e is the amount of dye adsorbed onto Mn-oxide (mg/g), V is the volume of the dye solution (L), and W is the mass of adsorbent Mn-oxide used (g) .

2.9. Kinetic Models Study

The decolorization kinetics shows the evolution of the decolorization capacity through time and it is necessary to identify the types of adsorption mechanism in a given system. Pseudo-first-order model, Pseudo-second-order model, Intra-particle diffusion model and Elovich models were used to describe the decolorization kinetics behavior of MB and OG by Mn-oxide surface.

2.10. Equilibrium Isotherm Modeling

Decolorization isotherms were determined by introducing 0.02g Mn-oxide to respective 50 mL of different dye concentrations at room temperature. The experimental data at equilibrium amount of adsorbed dye (q_e) on the adsorbent (Mn-oxide) and the concentration of dye in solution (C_e) at a constant temperature and pH were used to describe the optimum isotherm model. The linear forms of Langmuir, Freundlich, Temkin and Sips equations were used to describe the equilibrium data (**Table 2.3**). Applicability of these equations was compared by judging the correlation coefficients (R^2).

Table2.3: Different isotherm models used in this study and their linear forms

Isotherm	Nonlinear form	Linear form	Plot
Langmuir-II	$q_e = \frac{KLC_e}{1+KLC_e}$	$\frac{1}{q_e} = \left(\frac{1}{K_L q_m}\right)\frac{1}{C_e} + \left(\frac{1}{q_m}\right)$	$\frac{1}{q_e}$ VS. $\frac{1}{C_e}$
Freundlich	$q_e = K_F C_e^{1/n}$	$\log q_e = \log K_F + \frac{1}{n}\log C_e$	$\log q_e$ VS. $\log C_e$
Temkin	$q_e = \frac{RT}{b_T}\ln(K_T C_e)$	$q_e = \frac{RT}{b_T}\ln K_T + \frac{RT}{b_T}\ln C_e$	q_e VS. $\ln C_e$
Sips	$q_e = \frac{bq_m C_e^{1/n}}{1+bC_e^{1/n}}$	$\frac{C_e^{1/n}}{q_e} = \frac{1}{bq_m} + \frac{1}{q_m}C_e^{1/n}$	$\frac{C_e^{1/n}}{q_e}$ vs $C_e^{1/n}$

2.11. Effect of adsorbent mass

To investigate the effect of adsorbent mass, different mass of Mn-oxide (0.02 to 0.05 g) was introduced to a number of reagent bottles containing a specific

volume of a fixed MB and OG concentration at the same pH and at room temperature. Concentrations of MB and OG were measured at equilibrium.

2.12. Effects of initial Dye concentration (C_0) and contact time

To evaluate the effect of both contact time and decolorization kinetic, experiments were conducted at different periods using previously described system.

2.13. Antibacterial activities of MnO_2, Mn_3O_4 and γ−MnOOH nps

The antibacterial activity of MnO_2, Mn_3O_4 and γ−MnOOH nps was tested against the *Vibrio Cholerae*, *Escherichi Coli* and *S. Aureous* bacteria that cause cholera, dysentery, typhoid and diarrhea respectively using DMSO (7.5% v/v at which DMSO did not show antibacterial activity) media. The antibacterial experiments were performed following the standard conventional method by treating the MnO_2, Mn_3O_4 and γ−MnOOH nps suspension (10mg/10mL) to various pathogenic organisms. Bacteria such as *V. Cholerae, E. Coli* and *S. Aureous* were grown onto a Petri dish. 100µL of the MnO_2, Mn_3O_4 and γ−MnOOH nps suspension absorbed on a circular soaking paper was then placed into that dish. The reference antibiotic, tetracycline was also soaked on another similar soaking paper and placed into the same dish. The soaked papers were kept in contact with the bacteria for overnight and the antibacterial activity against the tested bacteria was predicted by measuring the zone diameter of inhibition both by the nanoparticles and the reference antibiotic.

CHAPTER III

RESULTS AND DISCUSSION

CHAPTER-III
RESULTS AND DISCUSSION

3. Synthesis and characterization

3.1. Synthesis of Mn-oxide

A novel and facile synthesis of MnO_2, Mn_3O_4 and γ−MnOOH nps with small particle size having large surface was synthesized which offers advantages like, simple and rapid preparative method, easy control of particle size and composition can be made in this method and also, there are various possibilities to modify the particle surface state and overall homogeneity. In all cases the concentration of $KMnO_4$, $MnSO_4$ and Mn(II) acetate solutions and the reaction temperature played an important role in the formation of Mn-oxide nanostructures with different morphologies and controlling particle properties.

3.1.1. Nanoparticle MnO_2 synthesis

The synthesis of MnO_2 nps was based on the method reported by Xiujuan Chu et al. with some modifications [125] using aqueous $KMnO_4$ and $MnSO_4$ solutions by co-precipitation method. Typically, to synthesize MnO_2 nps, 75 mL of 0.01 M $MnSO_4$ solution was taken in a 250 mL beaker and 50 mL of 0.01 M $KMnO_4$ solution was added dropwise by gentle stirring with magnetic stirring until completion at room temperature. The colour of the solution changed rapidly from purple to brown (indicating the onset of the formation of MnO_2 nps) and finally blackish brown. The resulting MnO_2 sol was continuously stirred for two hours and then kept for another 48 hours to ensure dispersion of MnO_2. The reaction taking place under these conditions may be written by stoichiometrically:

$$2MnO_4^-(aq) + 3MnSO_4(aq) + 2H_2O(aq) = 5MnO_2(aq) + 4H^+(aq) + 3SO_4^{2-}(aq)$$

The reaction product was collected by filtration, washed and then air dried at room temperature.

3.1.2. Nanoparticle Mn_3O_4 (husmannite) synthesis

Mn_3O_4 nps was prepared by forced hydrolysis of Mn(II) acetate by heating its aqueous solution. Typically, Mn(II) acetate (0.2 M 500 mL) solution was prepared in a 500 mL beaker. The solution was heated at about 80 ^{0}C in an oil bath for 2 hours and stirred with magnetic stirrer and then kept for another 48 hours at room temperature (28 ^{0}C).

$$Mn(CH_3COO)_2(aq) = Mn_3O_4(aq) + CH_3COOH(aq)$$

The resulting brown suspension was separated with centrifuged machine, washed with distilled water several times then dried in an electrical oven at 40^{0}C. A brown Mn_3O_4 nano powder was obtained in quantitative yield which was further kept in a desiccator.

3.1.3. Manganite synthesis

Manganite (γ−MnOOH) nps was synthesized by hydrothermal treatment. Typically, MnO_2 sol was prepared according to the procedure described in section **3.1.1.** Then 0.2 M Mn(II) acetate solution was taken a 1000 mL beaker and placed in an oil bath and heated at 80 ^{0}C with continuous stirring with magnetic stirrer. When Mn_3O_4 was supposed to form as observed brown solution which is the characteristic color of Mn_3O_4 nps, the previously prepared MnO_2 sol was transferred slowly into the beaker. The resulting mixture was heated at 80 ^{0}C for two hours and then kept for another 48 hours at room temperature (28 ^{0}C) for dispersion. The resulting dark steel grey suspension was separated with centrifuged machine, washed with distilled water several times then dried in an electrical oven at 40 ^{0}C. A dark steel grey nanopowder was obtained in quantitative yield which was further kept in a desiccator. The as prepared γ−MnOOH nps was used for analytical, oxidative and pathogenic activities.

3.2. Characterization of Mn-oxide nps

The prepared MnO_2, Mn_3O_4 and γ−MnOOH nano powder were characterized by FT-IR, X-Ray Diffraction (XRD), Energy-dispersive X-ray spectroscopy (EDX), Scanning Electron Microscopy (SEM), DLS, TG-DTA, pH_{PZC} and Specific Surface area (SSA). EDX provided the information about chemical composition. The oxides were characterized in terms of their particle size and morphology by SEM. In XRD analysis, the information about crystalline structure and particle size were found.

3.2.1. FT-IR spectral analysis

FT-IR spectral analysis provides some useful qualitative information on the identification of compounds. Both organic and inorganic substrates absorb IR light and thus IR active. Oxides and hydroxides of metal nanoparticles generally give absorption peak in the finger print region i.e. below wavelength of 1000 nm arising from inter-atomic vibrations. In order to get some insight about the structure of the synthesized oxides, FT-IR spectra of MnO_2, Mn_3O_4 and γ−MnOOH nps are presented in **Fig. 3.1 to 3.3.**

The FT-IR spectrum of black MnO_2 is presented in **Fig. 3.1**. The IR spectra did not have strong M–O stretching frequencies, however a weak peak was observed at ca. 571 and 535 cm^{-1} which corresponded to the Mn–O stretching frequencies [176, 177]. Broad absorption peaks centered at around 3400 cm^{-1} and 1630 cm^{-1} are caused by the absorbed water molecules and carbon dioxide because the nanocrystallines materials exhibit a high surface-to-volume ratio [178]. A peak due to Mn–O vibrations was observed at 715 cm^{-1} in the spectra of MnO_2. The band at 1060 cm^{-1} is absorption peak of the Mn-OH functional group, and band at 1400 cm^{-1} are associated with the hydration water of MnO_2. Therefore, the FT-IR spectrum further confirmed that the as-synthesized product is MnO_2.

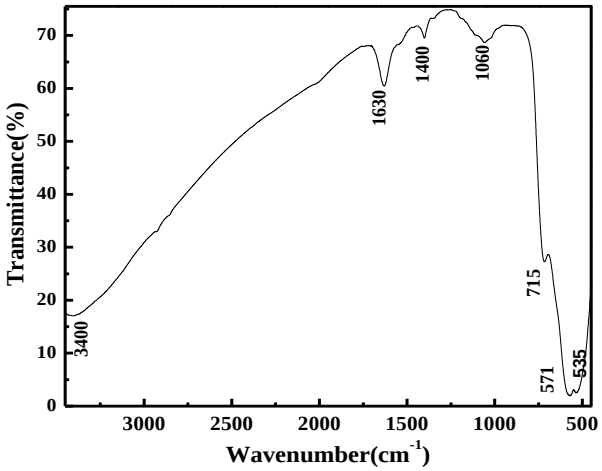

Fig. 3.1. FT-IR spectra of MnO_2 nps obtained by co-precipitation method by the reduction of $KMnO_4$ by $MnSO_4$ solution at room temperature.

FT-IR spectral analysis also provided useful qualitative information on the identification of the Mn_3O_4 compounds **(Fig. 3.2)**. The FT-IR spectrum of the present powder nps displayed three main bands at ca. 627, 526 and 411 cm^{-1} which are in agreement with the previous IR findings on Mn_3O_4 compounds [179, 180] suggesting that the bands at ca. 627 and 526 were associated with the coupling modes between the Mn–O stretching modes of tetrahedral and octahedral sites and the band at ca. 411 cm^{-1} was due to the band stretching mode of the octahedral sites. Moreover, the band at 1559 cm^{-1} corresponded to the O-H vibrating mode of the adsorbed water. Thus, the result further confirmed that the nanoparticle analyzed was Mn_3O_4.

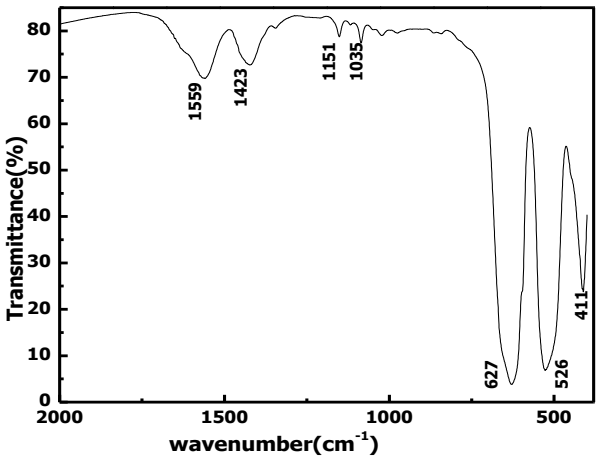

Fig.3.2. FT-IR spectra of Mn_3O_4 nps obtained by forced thermal hydrolysis of Mn(II) acetate solution at 80^0C for 2h.

The FT-IR spectrum of γ−MnOOH nps is presented in **Fig. 3.3**. The peaks at 447, 491 and 594 cm^{-1} corresponded to Mn–O stretching vibrations. The typical broad absorption in the wavelength ranges between 4,000 and 3,000 cm^{-1} are allocated both the stretching collision of H–O–H and hydroxyl absorption, while the peak detected at 1,564 cm^{-1} and 1423 cm^{-1} corresponded to the existence of large numbers of residual O-H groups, which implied the O-H vibrating mode of traces of adsorbed water. The simultaneous presence of both these peaks indicated the existence of adsorbed H_2O molecule for this sample. The broad band at 3400 cm^{-1} is believed to be associated with the stretching vibrations of hydrogen-bonded surface water molecules and hydroxyl groups. The peaks at 1,152 and 1085 cm^{-1} were attributed to OH-bending modes to γ−OH and d-1-OH respectively [181]. The broad peak at 2600-2700 cm^{-1} is the fundamental O-H stretching band related to the H-bond with an O-H....O length of about 2.60 A^0 in the structure of manganite. Another peak at 2074 cm^{-1}.was also observed in the study of Kohler et al [181]. This band could be considered as a combination band of the O-H stretching mode at 2666 cm^{-1} (f_1) and the excited lattice mode at 592 cm^{-1}(f_2). Thus, by $f = f_1 - f_2$, i.e., 2666-592 cm^{-1} = 2074 cm^{-1} , the value obtained is close to the reported 2060 cm^{-1} by Kohler et all [181]. The spectrum was consistent with typical reported reference about MnOOH [176].

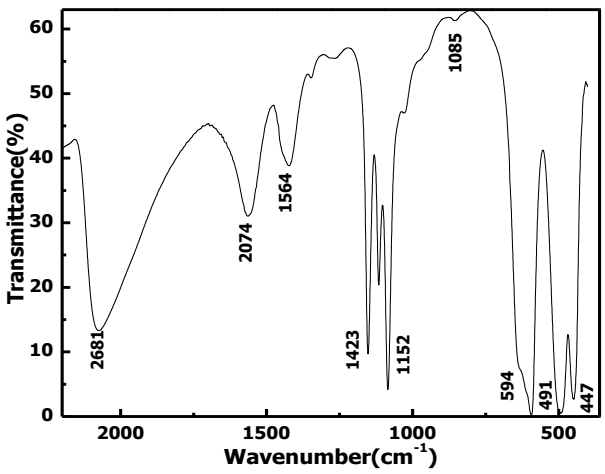

Fig. 3.3. FT-IR spectra of γ−MnOOH nps obtained by incorporation of MnO_2 sol into Mn(II) acetate solution at 80^0C for 2h.

3.2.2. X-ray diffraction (XRD) analysis

X-ray scattering technique is a non-destructive analytical technique which reveals information about the crystallographic structure, chemical composition, and physical properties of materials. This technique are based on observing the scattered intensity of an X-ray beam hitting a sample as a function of incident and scattered angle, polarization, and wavelength or energy. X-ray diffraction yields the atomic structure of materials and is based on the elastic scattering of X-rays from the electron clouds of the individual atoms in the system. The most comprehensive description of scattering from crystals is given by the dynamical theory of diffraction. Powder diffraction (XRD) is a technique used to characterize the crystallographic structure, crystallite size (grain size), and preferred orientation in polycrystalline or powdered solid samples. Powder diffraction is commonly used to identify unknown substances, by comparing diffraction data against a database maintained by the International Centre for Diffraction Data.

The XRD pattern of MnO_2, Mn_3O_4 and γ−MnOOH nps are given in the **Fig. 3.4, 3.5, and 3.6** respectively. The scattering pattern as a function of Bragg angle, 2θ at λ= 1.54056 nm for the studied samples powder present in those figures.

Fig.3.4 shows the XRD recorded for the chemical coprecipitation MnO_2 nps. It can be seen from the figure that the peak profile (Ref. Code 00-030-0820) is broad and most of the peaks (2θ = 23.5^0, 37.14^0, 42.48^0, 56.30^0) are indexable to tetragonal γ-MnO_2 phase (space group: I4/m) and a peak (2θ =66.84^0) of δ-MnO_2 phase. The broadness of the peaks indicates that the formed compound has predominantly nanophase. The content of our results matches with JCPDS (Joint Committee on Powder Diffraction Standard) card 044-014 on Annes-A indentifying the sample to be δ-MnO_2 nanoparticle. From XRD data it is clear that synthesized

MnO_2 nps was pure crystalline in nature. Average particle size of MnO_2 nps was found to be 3.0 to 10.0 nm.

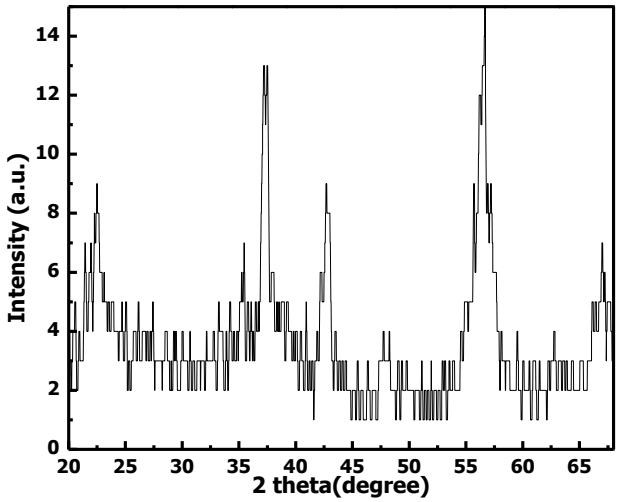

Fig. 3.4. XRD pattern of MnO_2 nps synthesized by co-precipitation method.

The XRD pattern of the powder Mn_3O_4 nanoparticles is shown in **Fig. 3.5**. The results of as synthesized Mn_3O_4 nanoparticles match with JCPDS pattern No. 00-024-0734. All diffraction peaks can be perfectly indexed to the Body-centered tetragonal hausmannite structure [67] (space group: I41/amd (141)) with strong ring patterns due to (1 0 1), (1 0 3), (2 1 1), (2 2 0), (2 2 4), and (4 0 0) planes. The Mn_3O_4 lattice constants obtained by refinement of the XRD data of the nanoparticles are a = b = 5.7630Å and c = 9.4560Å, which are consistent with standard values for bulk Mn_3O_4 [67], although the peaks were widened as a result of the small-size effects of the nanoparticles. No characteristic peaks of impurities, such as other forms of manganese oxides, were detected.

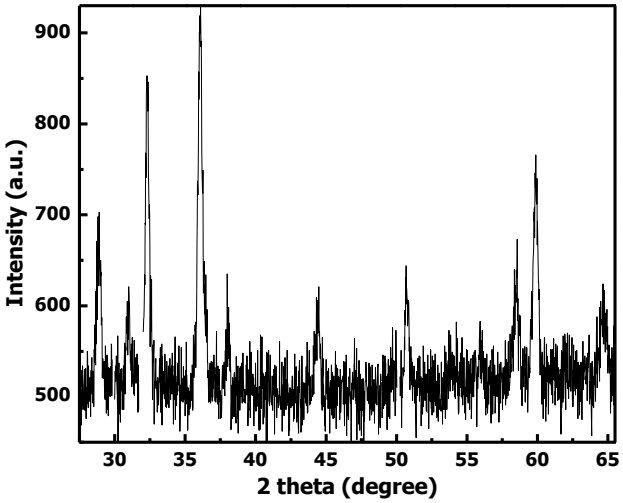

Fig. 3.5: XRD pattern of Mn_3O_4 nps by hydrothermal synthesis method.

All of the reflections of the XRD pattern **(Fig. 3.6)** of as synthesized γ–MnOOH nps were indexed to a pure monoclinic phase of γ–MnOOH (manganite, space group $p2_1/c$ (14)) with lattice parameters a= 5.307 A^0, b= 5.277 A^0 and c = 5.307 A^0 and β =114.38^0 (Ref. code 00-008-0099). The distinguishing lattice plane peaks are present in 110 (26.0°), 020(33.8°), 111(35.6°), 002 (37.1°), 121(39.5°) and 220 (51.4°). The peaks 100 and 110 are counterpart of JCPDS card 01-088-0649; 600, 440 and 448 are match with JCPDS card 361216; 104 is match with JCPDS card 730603. The XRD pattern shows the evidence that the γ–MnOOH nps was perfectly synthesized in the present work [181, 182].

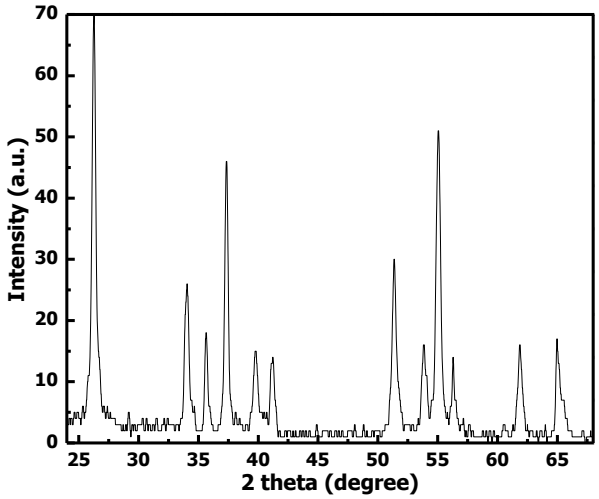

Fig.3.6: XRD pattern of γ–MnOOH nps obtained by hydrothermal synthesis method.

Crystallite size of MnO_2, Mn_3O_4 and γ–MnOOH nps

Crystallite size of manganese dioxide, Mn_3O_4 and γ–MnOOH nps was calculated by fitting the synchrotron XRD results usin the Scherrer equation,

$$D_p = \frac{0.94\lambda}{\beta_{1/2}\cos\theta}$$

Where, θ = Bragg angle, λ=1.5406 nm = wave length of X-ray, $\beta_{1/2}$ =Full Width Half- maxima (FWHM), D_p = crystallite size of particle.

The particle sizes of black MnO_2 measured from Peaks (101), (200), (111) and (210) was ca. 6.47 nm. The crystallite sizes measured from the four peaks (1 1 2), (1 0 3), (2 1 1), and (224) were averaged to obtain the Mn_3O_4 crystallite size was ca. 9.65 nm which is in agreement with the TEM observation of the Mn_3O_4 nanoparticles prepared by force hydrolysis of $Mn(OOCCH_3)_2$ solution at 80^0C for 2h [176].The particle size of γ–MnOOH nps was 8.61 nm. Therefore, it can be concluded from this result that the oxides that were prepared in this study were in the nano state.

3.2.3. Scanning electron microscopy (SEM) analysis

The scanning electron microscope (SEM) is a type of electron microscope that images the sample surface by scanning it with a high-energy beam of electrons in a raster scan pattern [40]. The electrons interact with the atoms that make up the sample producing signals that contain information about the sample's surface topography and composition. The black MnO_2 **(Fig.3.7)**, brown Mn_3O_4 **(Fig.3.8)** and γ–MnOOH nps **(Fig.3.9)** samples obtained were layered over steel plate for its SEM analysis. All the images display well-dispersed particles, however, with different morphologies and varying uniformity [41]. The average particle size distribution measured from SEM may be in higher range (10 nm to 100 nm) than the crystallite size measured from XRD. This is expected as

the XRD measurement is a mean of the actual crystallite size. Albeit, the particles were found to be highly crystallite according to the X-ray diffraction studies but from the SEM images a thick amorphous layer surrounding each particle was observed [42]. From these images it can be seen that particles are of needle shape but not well distributed. In all cases more than 80% particles are of nanometer level.

From SEM picture of MnO_2 nps (**Fig. 3.7)** it can be seen that they consist of rod-like nanostructures with an average diameter of 10-50 nm, an average length of 2µm and are present in a large quantity which is in good agreement with literature [133].

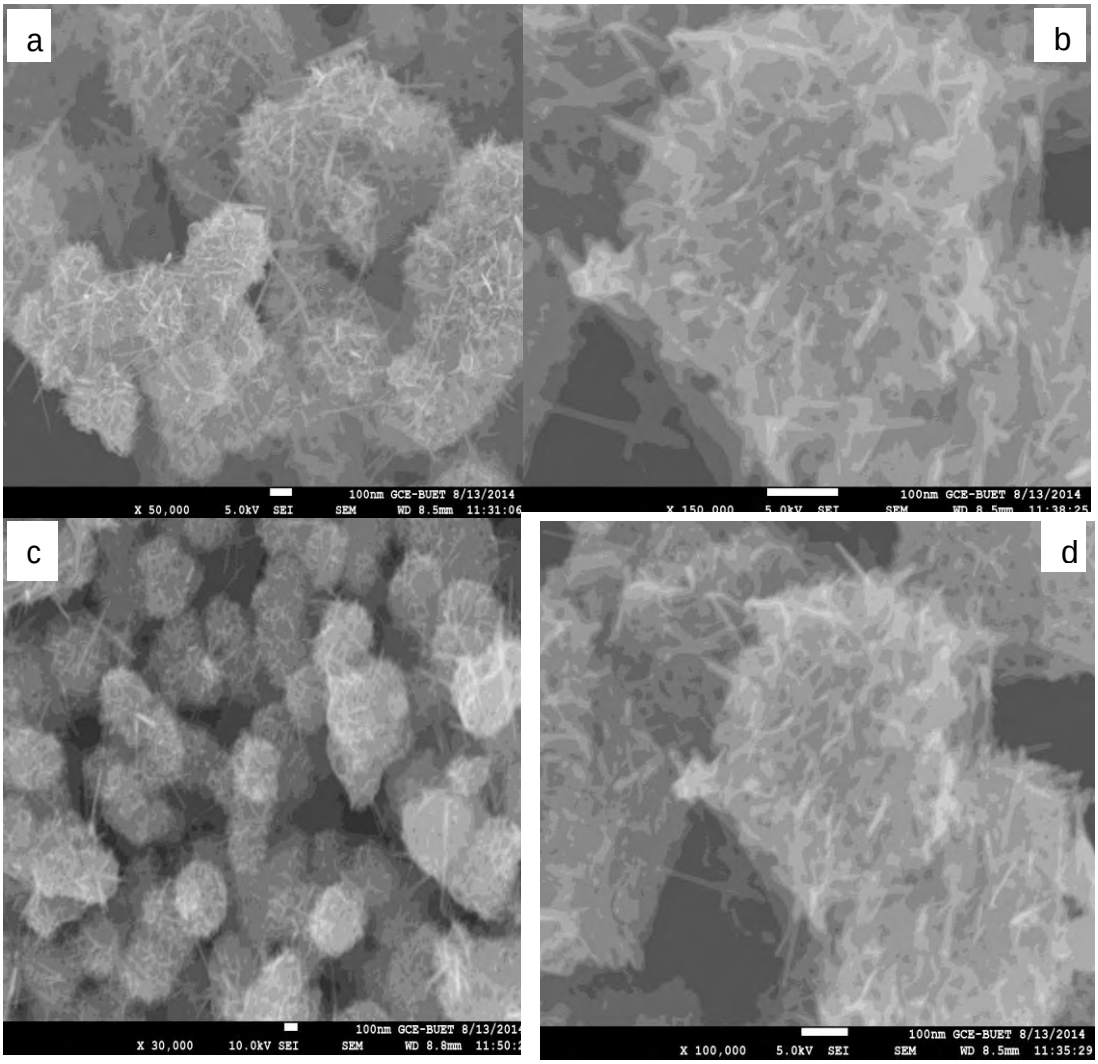

Fig. 3.7 (a-d): SEM micrograph of black MnO_2 nps at different pixels.

The morphology as-synthesized Mn_3O_4 nps is shown in **Fig.3.8. (a-d)**. Aggregated nanoparticles with octahedral shapes are observed and their diameter varies between 10 and 80 nm. The SEM results of the Mn_3O_4 nps agreed well with the XRD data [147].

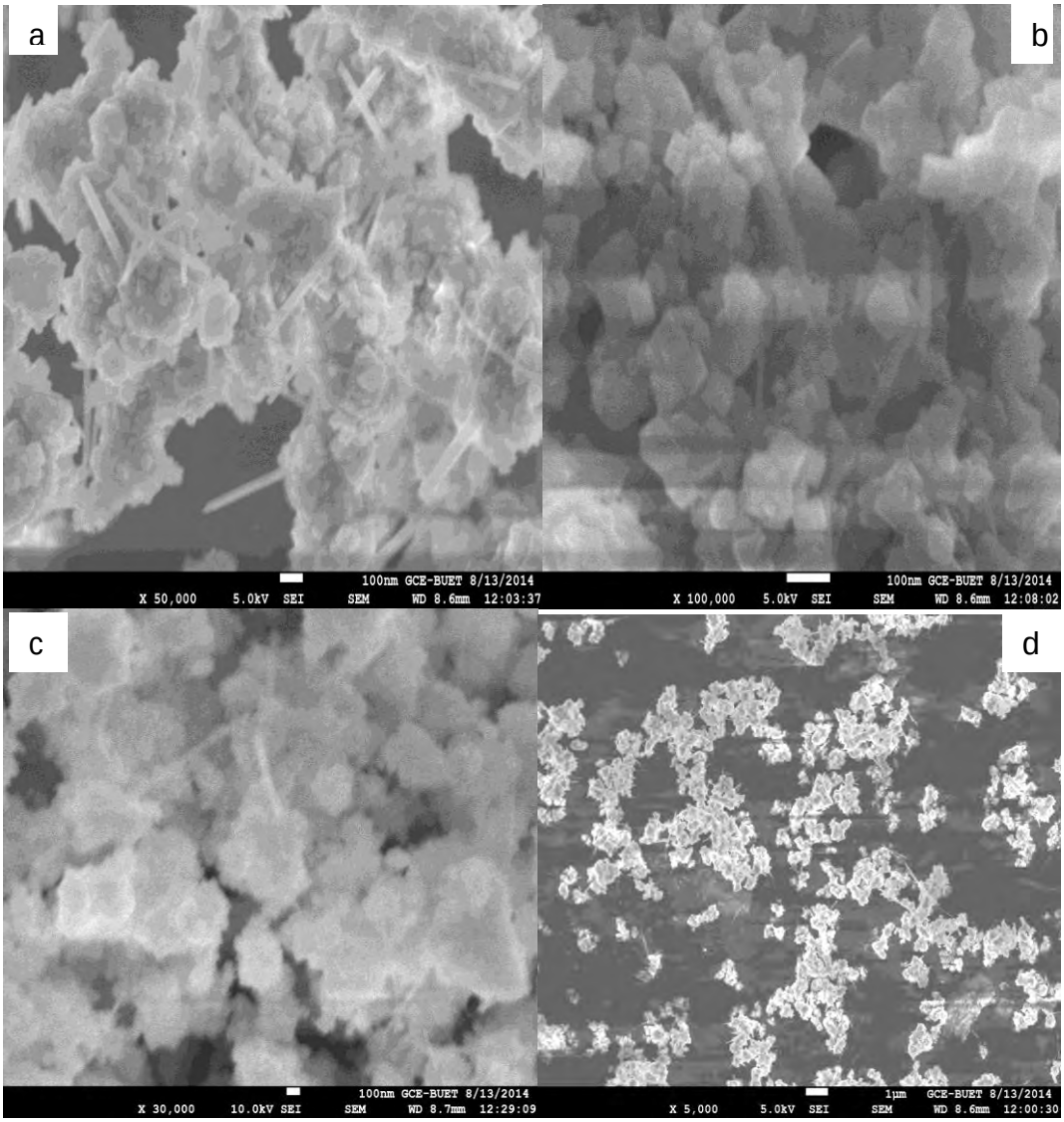

Fig. 3.8. (a-d): SEM micrograph of brown Mn_3O_4 nps at different pixels.

The SEM observations of γ–MnOOH nps (**Fig. 3.9)** show that particles are agglomerated but were not uniform in size and particle diameter varies between 6 to 30 nm and lengths of several micrometers. The particle morphology observed rod like with uneven shapes [182].

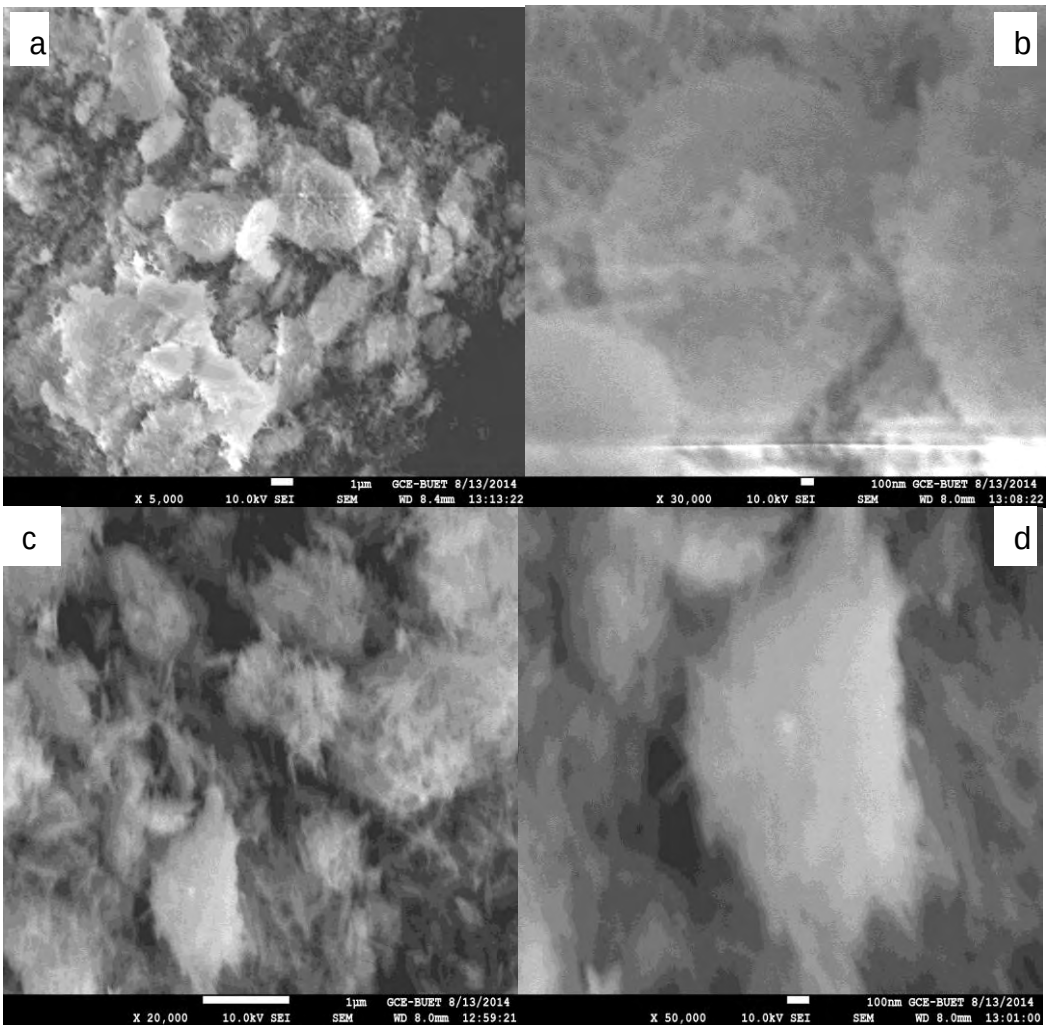

Fig. 3.9 (a-d): SEM micrograph of γ–MnOOH nps at different pixels.

3.2.4. Energy-dispersive X-ray (EDX) analysis

EDX is an analytical technique [43] used for the elemental analysis of a sample. It is one of the variants of X-ray fluorescence spectroscopy which relies on the investigation of a sample through interactions between electromagnetic radiation and matter, analyzing X-rays emitted by the matter in response to being hit with charged particles. Its characterization capabilities are due in large part to

the fundamental principle that each element has a unique atomic structure allowing X-rays that are characteristic of an element's atomic structure to be identified uniquely from one another.

To stimulate the emission of characteristic X-rays from a specimen, a high-energy beam of charged particles such as electrons or protons, or a beam of X-rays, is focused into the sample being studied. At rest, an atom within the sample contains ground state (or unexcited) electrons in discrete energy levels or electron shells bound to the nucleus. The incident beam may excite an electron in an inner shell, ejecting it from the shell while creating an electron hole where the electron was. An electron from an outer, higher-energy shell then fills the hole, and the difference in energy between the higher-energy shell and the lower energy shell may be released in the form of an X-ray. The number and energy of the X-rays emitted from a specimen can be measured by an energy-dispersive spectrometer. As the energy of the X-rays is characteristic of the difference in energy between the two shells, and of the atomic structure of the element from which they were emitted, this allows the elemental composition of the specimen to be measured.

EDX of black MnO_2

After selecting the excellent as-synthesized product, its chemical composition was analyzed by EDX (**Fig. 3.10)**. From EDX analysis it was found that the product was composed of Mn and O elements only. The peak of Cu was caused by the Cu microgrid on which the product was placed. The Mn peak observed at 5.894 keV and peak observed at 1.34 keV for K lines of the oxygen element. The percentage of Mn and O were determined from the intensity of the lines and the results are summarized further in **Table 3.1.**

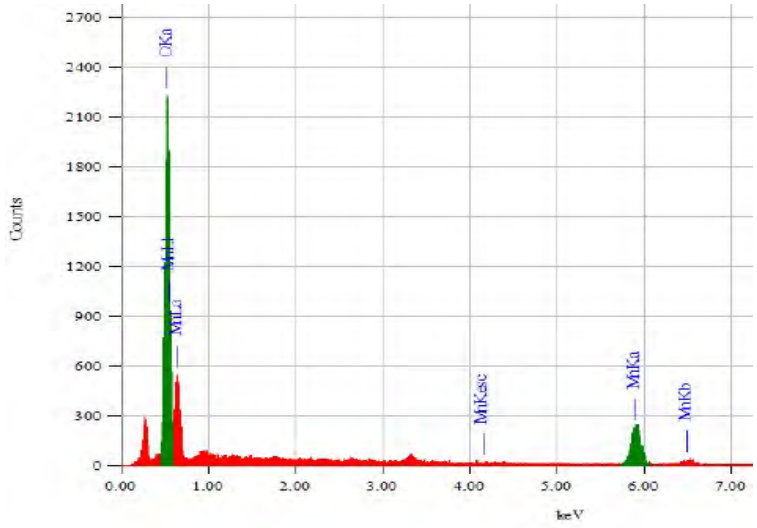

Element	(keV)	Mass%	Sigma	Atom%
O K	0.525	35.69	0.28	65.58
Mn K	5.894	64.31	1.38	34.42
Total		100.00		100.00

Fig. 3.10: Elemental analysis of as-synthesized MnO_2 at sample location 4.

Table 3.1: Elemental composition of MnO_2

Elements	Sample location 1	Sample location 5	Sample location 4	Average composition elements (%)	Average composition formula
Mn (%)	33.58	33.88	34.42	33.96	
O (%)	66.42	66.12	65.58	66.04	MnO_2

Therefore, from the chemical composition, it can be concluded that the composition of the prepared black sample is MnO_2 and no other phases were present [133].

EDX of brown Mn_3O_4

Elemental analysis of the powder brown Mn_3O_4 nps was achieved from the EDX spectra as presented in **Fig 3.11.** The Mn peak observed at 5.894 keV and 0.525 keV for k lines of the oxygen element and at 1.00 is for M lines of the copper element (that employed as reference substrate). The lines assigned to O and Mn agrees with those found in a previous report [31]. The average quantities of Mn and O in the prepared Mn_3O_4, according to the EDX spectrum are 34.37% and 65.63% respectively **(Fig.3.11)**. The percentage of Mn and O were determined from the intensity of the lines and the results are summarized further in **Table 3.2.**

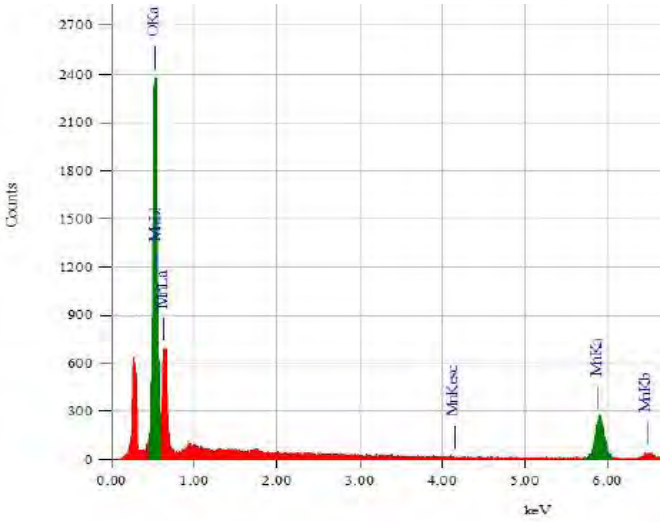

Fig.3.11. EDX analysis of the powder Mn_3O_4 nps prepared by heating 0.2M Mn(II) acetate solution at 80^0 C for 2 h at sample location 2.

Table 3.2: Elemental composition of brown Mn_3O_4

Elements	Sample location 2	Sample location 1	Sample location 3	Average composition elements (%)	Average composition formula
Mn (%)	34.37	33.52	36.08	34.65	
O (%)	65.63	66.48	63.92	65.34	Mn_3O_4

Thus, from the chemical composition obtained from the EDX spectrum, it can be calculated that the composition of the prepared sample is Mn_3O_4 and no foreign elements were present [67].

EDX analysis of γ−MnOOH nps

Elemental analysis of the prepared γ−MnOOH nps was performed by employing EDX method. The patterns of the EDX spectrums at different locations are presented in **(Fig. 3.12-14)**. The peaks observed at 5.894, 5.894 and 5.894 keV for K line of the Mn element and the peaks at 0.525, 0.525 and 0.525 keV for K series respectively for the oxygen element **(Fig.3.12-14)**. The percentage of Mn and O were determined from the intensity of the lines and the results are summarized further in **Table 3.4.**

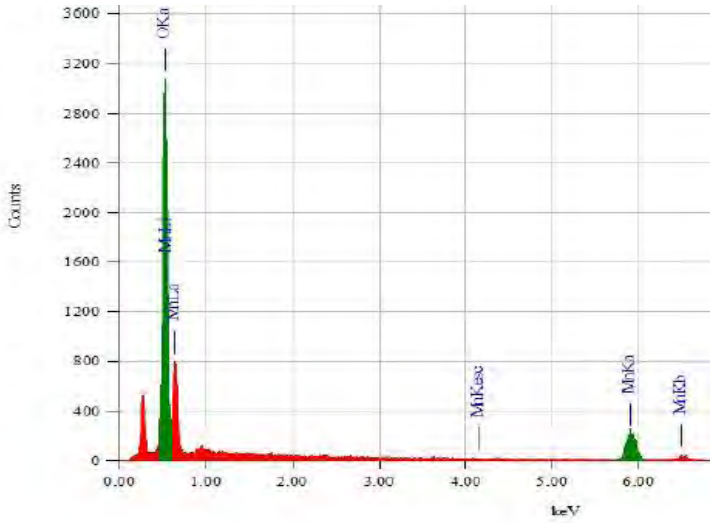

Element	(keV)	Mass%	Sigma	Atom%
O K	0.525	43.80	0.30	72.80
Mn K	5.894	56.20	1.23	27.20
Total		100.00		100.00

Fig. 3.12: Elemental analysis of γ−MnOOH nps at sample location 1.

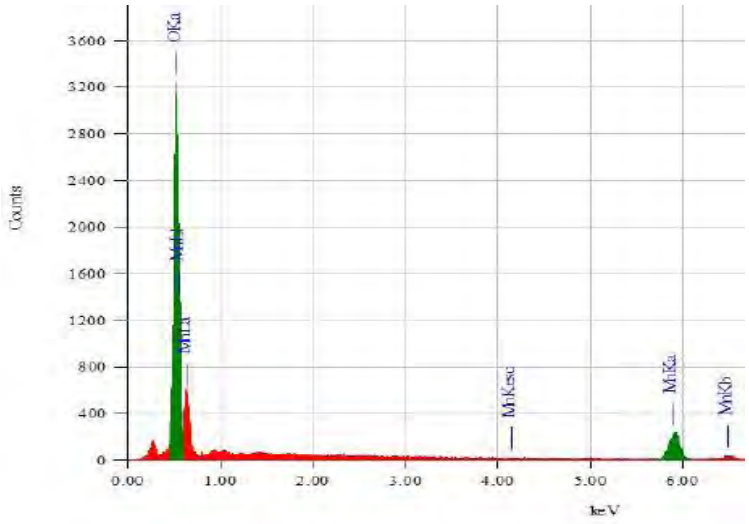

Element	(keV)	Mass%	Sigma	Atom%
O K	0.525	46.10	0.12	74.60
Mn K	5.894	53.90	0.62	25.40
Total		100.00		100.00

Fig. 3.13: EDX analysis of γ−MnOOH nps at sample location 3.

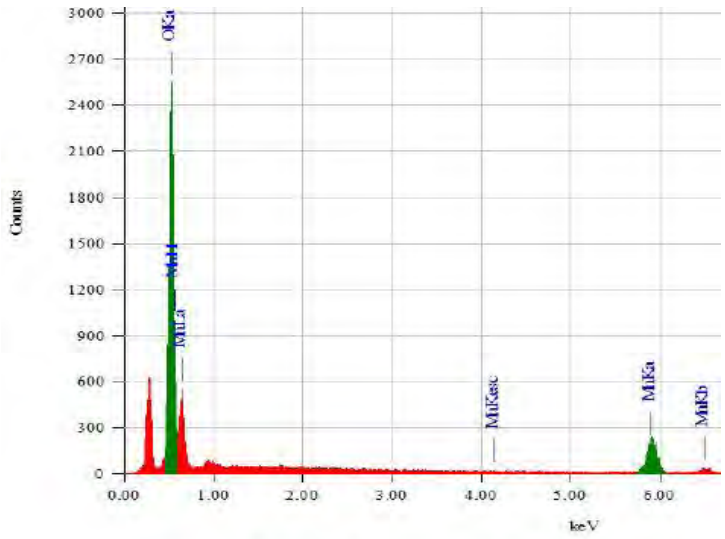

Element	(keV)	Mass%	Sigma	Atom%
O K	0.525	40.52	0.12	70.05
Mn K	5.894	59.48	0.68	29.95
Total		100.00		100.00

Fig. 3.14: EDX analysis of γ−MnOOH nps at sample location 4.

Table 3.3: Elemental composition of γ−MnOOH nps

Elements	Sample location 1	Sample location 3	Sample location 4	Average composition elements (%)	Average composition formula
Mn (%)	27.20	25.40	29.95	27.55	
O (%)	72.80	74.60	70.05	72.48	MnOOH

Thus, from the chemical composition obtained from the EDX spectrum, it can be calculated that the composition of the prepared sample is MnOOH and no impurity was found.

3.2.5. DLS analysis of as synthesized samples

DLS analysis of MnO_2

DLS spectra of black MnO_2 is given in **Fig. 3.15**. The hydrodynamic particle size, DLS data was taken over time. The DLS data indicated that the particles are in aggregate state, not individual particle size. The hydrodynamic diameter (Z-average) for MnO_2 was 809 nm with a polidisperse index of 0.089. Therefore, the particle is big and agglomerated [184].

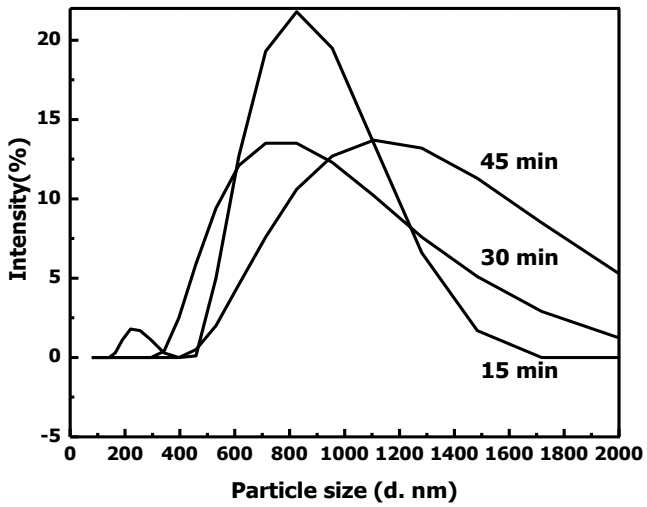

Fig.3.15: DLS spectra for black MnO_2 sample at three time interval.

DLS analysis of Mn_3O_4

DLS spectra of Mn_3O_4 are presented in **Fig. 3.16**. In this case hydrodynamic diameter is 392 nm with polydisperse index of 0.248. If any solution contains large aggregates (visible floating in solution or particles that settle with time) then the presence of the larger particles dominate the light scattering signal and mask the presence of the smaller particles. It is interpreted that the readings of sizes above 500 nm with PI >0.5 as "big and agglomerated" without giving much weight to the actual numbers. Thus, our synthesized sample Mn_3O_4 is big and agglomerated.

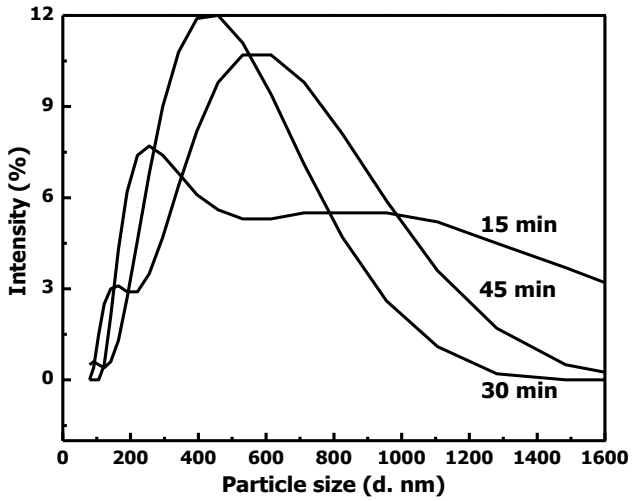

Fig. 3.16: DLS spectra for as-synthesized brown Mn_3O_4 nps.

DLS analysis of γ–MnOOH nps

DLS analysis of γ–MnOOH nps is presented in **Fig.3.17**. The hydrodynamic diameter is 183 nm with a polydispersity index of 0.137. If the DLS measured diameters is in the 100–300 nm range with a polydispersity index of 0.3 or below then it classified as polydisperse nanoparticle solutions or stable solutions of aggregated nanoparticles (no visible particulates and no particle settling). Thus, the as synthesized sample is polydisperse aggregated nanoparticles.

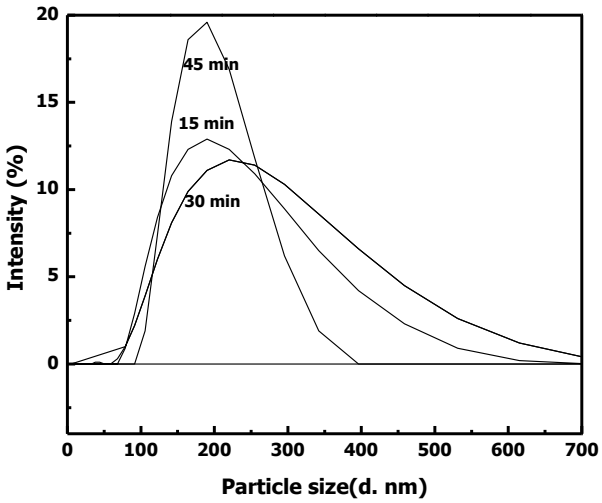

Fig. 3.17: DLS spectra for as-synthesized blackish brown γ–MnOOH nps.

3.2.6. Thermo gravimetric analysis (TG-TDA)

TG analysis of MnO_2, Mn_3O_4 and γ–MnOOH nps

The temperature of decomposition, crystallization and phase transformation of the as-prepared powder was studied using TGA measurement for the typical composition Mn-oxide in the temperature range 30 to 800^{0}C at a heating rate of 10^{0}C/min using alumina pan. TG curves for the dried sample of MnO_2, Mn_3O_4 and γ–MnOOH nps are presented in **Fig. 3.18**.

TG curve of MnO_2 indicated that the reduction in weight due to evaporation of contained water begins simultaneously with the start of temperature increase and the weight reduction continued until the sample is heated over 800^{0}C. Inspection of this curve also showed that major losses in weight around 450^{0}C and 750^{0}C. These abrupt reductions in sample weight indicated oxygen emitted by the sample reactions expressed in the following reactions:

$$2MnO_2 \longrightarrow MnO_2 + 1/2O_2$$

$$3MnO_2 \longrightarrow 2Mn_3O_4 + 1/2O_2$$

These decomposition reactions showed that MnO_2 cannot be heat dried at atmospheric pressure.

In case of Mn_3O_4 nps, thermal gravimetric (TG) were carried out between 30 and 800^{0}C (**Fig.3.18**). In the temperature range of 25–250^{0}C, the weight loss

of 9.15% can be related to the release of weakly adsorbed water molecules. The broad exothermic peak at about 350^0C, associated with the mass gain, is about 0.4% (**Fig. 3.18**). As confirmed by earlier studies [185–187], this thermal event can be corroborated by the fact that Mn_3O_4 (Mn_1^{+II}, Mn_2^{+III}) can be transformed into Mn_5O_8 (Mn_2^{+II}, Mn_3^{+IV}) in the temperature range of 300–450^0C [188]. The new (Mn_5O_8) phase is formed according to the following reaction:

$$Mn_3O_4 + \frac{2}{5}O_2 \longrightarrow \frac{3}{5}\,Mn_5O_8$$

Mn_5O_8 was observed during the decomposition of manganese oxalate [189] as well as in the transformation of hydrohausmannite into anhydrous hausmannite [190]. The oxidation of Mn^{3+} to Mn^{4+} in the temperature range of 300–450^0C leads to the crystallization of the Mn_5O_8 phase. After the exothermic peak at 350^0C the mass remains relatively constant.

The TG plot of γ–MnOOH nps indicated that the slight weight loss could be categorized into three segments. According to literature [191], the initial weight loss of about 2% below 120^0C is due to the removal of physically adsorbed water, in good agreement with previous observations. The following weight loss in the temperature range of 120-300^0C should correspond to the dehydroxylation. The third peak at 530-630^0C is due to deoxygenation of MnO_2 to Mn_2O_3 with a weight loss of about 5.5%.

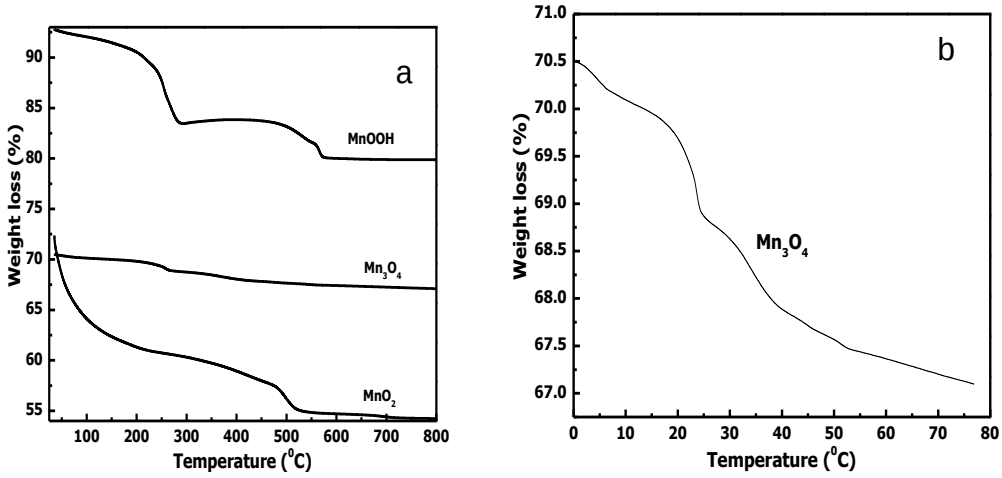

Fig.3.18. TG curves for MnO_2, Mn_3O_4 and γ–MnOOH nps (a) and Mn_3O_4 nps (b).

DTG analysis

DTG curves for the dried sample of MnO_2, Mn_3O_4 and γ–MnOOH nps are presented in **Fig. 3.19**. The DTG curve of γ–MnOOH nps recorded in N_2 atmosphere, curve showed that γ–MnOOH nps did not decompose, but weight loss was due to dehydrogenation and decarboxylation and yield final product at 585^0C. This weight loss and weight gained was very negligible. This weight change was in the range of 0.02 % only. These indicated that the synthesized powder was almost stable from the beginning.

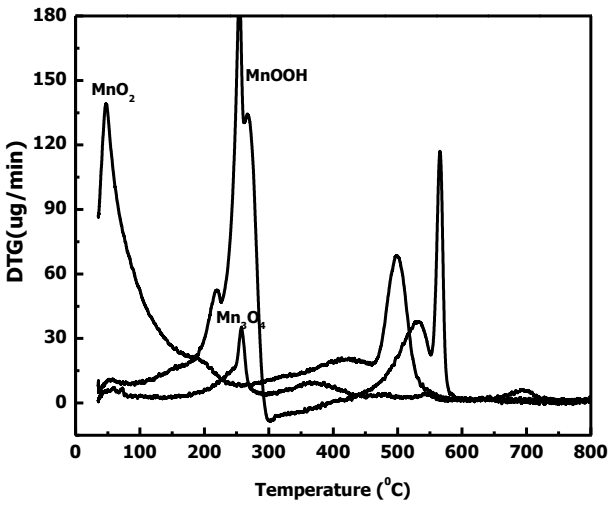

Fig.3.19. DTG curves for MnO_2, Mn_3O_4 and γ–MnOOH nps.

DTA curves analysis

DTA curves for MnO_2, Mn_3O_4 and γ–MnOOH nps are presented in **Fig. 3.20**. From TDA curve of MnO_2, it can be seen that a one to one correlation exists between these thermo analytical curves indicating that the thermal effects was accompanied by weight loss. There were two endothermic and one exothermic peak observed for MnO_2 decomposition. First step below 150^0C is ascribed to the vaporization of absorbed water. Second step is from 150 to 400^0C associated with

the residual matter. The third step above 400^0C is due to weight loss of as synthesized MnO_2.

In DTA curve of Mn_3O_4, the endothermic event at 575^0C associated with the weight loss of about 2% are related to the consequent release of oxygen due to the reduction of Mn_5O_8 to Mn_2O_3. The reaction scheme can be written as follows:

$$\frac{3}{5}Mn_5O_8 \longrightarrow \frac{3}{2}\ Mn_2O_3 + \frac{3}{20}O_2$$

The weight loss is still constant at temperature higher than 700^0C indicating the completion of the thermal decomposition of the intermediate phase (Mn_5O_8) and the beginning of the crystallization of Mn_2O_3 as a new phase.

The DTA curve of γ–MnOOH nps shows an endothermic peak near at 370°C, related to the oxidation reaction γ phase formation γ-MnOOH and β-MnO_2 (pyrolusite) according to the equation A. A second mass loss of about 1.3% is observed in the range 530-630° C in the presence of a small endothermic peak at this same interval on the phase transformation of β -MnO_2 for Mn_2O_3 according to the equation B. And finally a third peak is observed in the 740-820°C range, which corresponds to the transformation reaction of Mn_2O_3 for Mn_3O_4 (Equation C) with 1.7% weight loss in the TG curve [192, 193].

$$4\ MnOOH + O_2 \rightarrow 4\ MnO_2 + 2\ H_2O \qquad (A)$$

$$6\ MnO_2 \rightarrow 3\ Mn_2O_3 + 3/2\ O_2 \qquad (B)$$

$$3\ Mn_2O_3 \rightarrow 2\ Mn_3O_4 + 0{,}5\ O_2 \qquad (C)$$

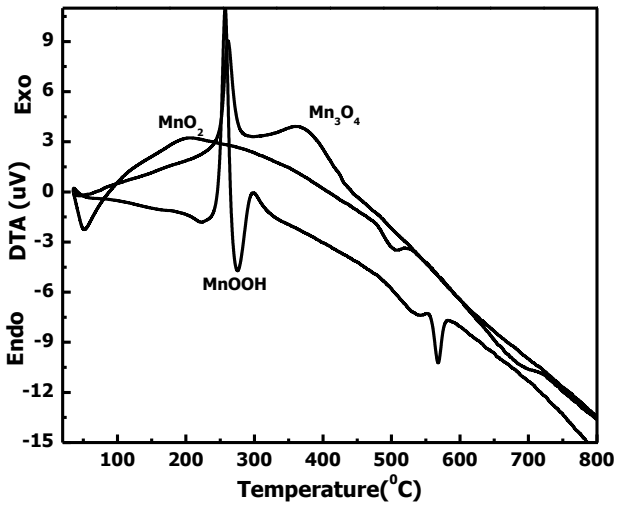

Fig. 3.20. DTA curves for MnO_2, Mn_3O_4 and γ−MnOOH nps.

3.2.7. Determination of point of zero charge (pH_{PZC}) of Mn-oxide nps

The point of zero charge of a solid substance (pH_{PZC}) means the pH at which the positive and negative charge in the surface are equal. pH_{PZC} has been determined by simple acid-base titration. It is described in section **2.3.7**. The pH metric titration data and the curves for three different concentration of NaCl solution are shown in **Fig.3.21-3.32 and Table 1 -6** in appendix.

3.2.7(a). Point of zero charge of γ−MnOOH nps

The net titration curves corresponding to three different ionic strengths are shown in **Fig.3.24** and data in **Table 2** in appendix. If the pH of the bulk is higher than pH_{PZC} surface then becomes negative and the lowering of the pH of the bulk than pH_{PZC} make the surface positive. It is seen from **Fig. 3.24,** the point of zero charge of γ−MnOOH nps surface was found to be 9.8 which is in agreement with literature [194].

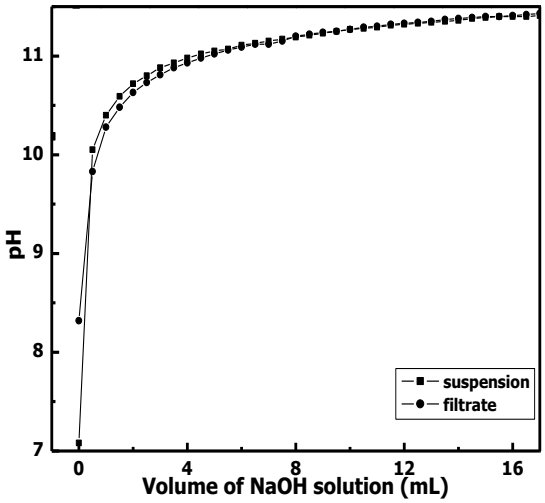

Fig. 3.21: pH metric titration curves for γ–MnOOH nps with 1×10^{-1}M NaCl.

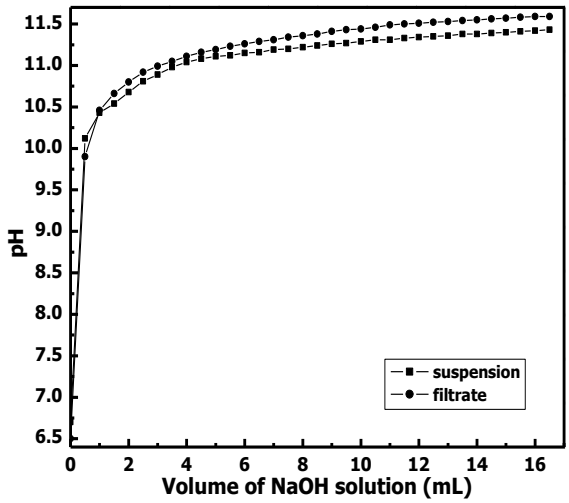

Fig. 3.22: pH metric titration curves for γ–MnOOH nps with 1×10^{-2}M NaCl.

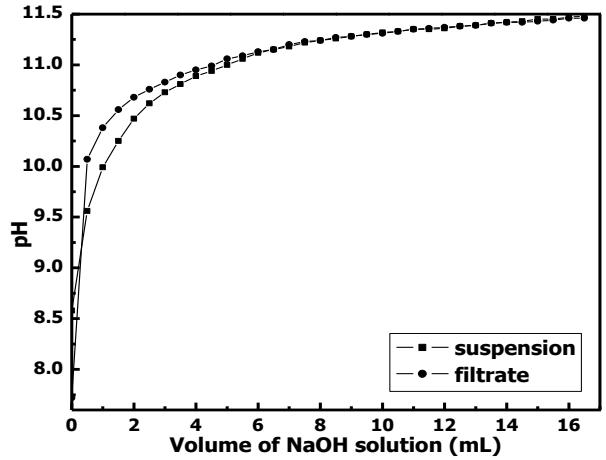

Fig. 3.23: pH metric titration curves for γ–MnOOH nps with 1×10^{-3} M NaCl.

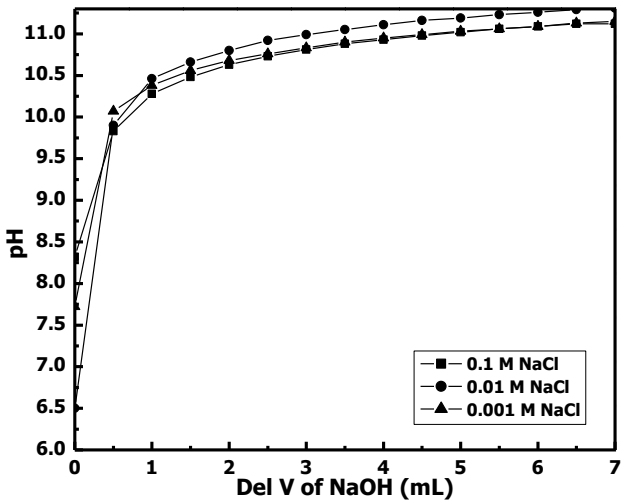

Fig.3.24: Net titration pH_{PZC} curve for γ–MnOOH nps in the presence of different concentrations of NaCl solution. These curves intersect at pHpzc.

3.2.7(b). Determination of point of zero charge (pH_{PZC}) of MnO_2

The pH metric titration data for MnO_2 and the curves for three different concentration of NaCl solution are shown in **Table 3-4** in appendix and **Fig.3.25-3.28**. The net titration curves corresponding to three different ionic strengths are shown in **Fig.3.28.** From **Fig.3.28,** the point of zero charge of MnO_2 nps surface was found to be 8.8 which is similar to previous report [134, 195]. They found pH_{PZC} for MnO_2 nanoparticles at 8.53 and for pyrolosite at 7.50.

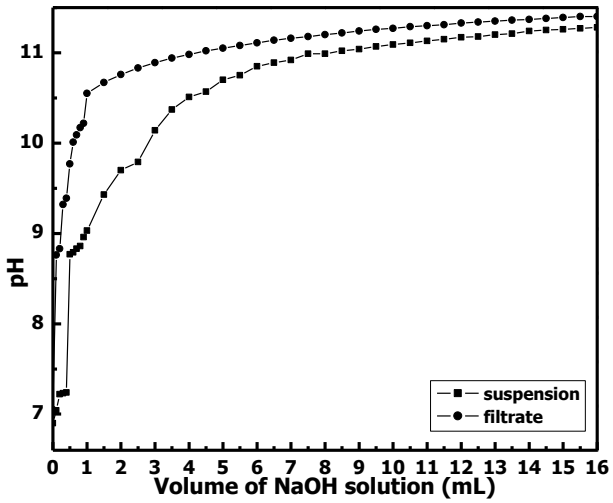

Fig. 3.25: pH metric titration curves for MnO_2 nps with 1×10^{-1}M NaCl.

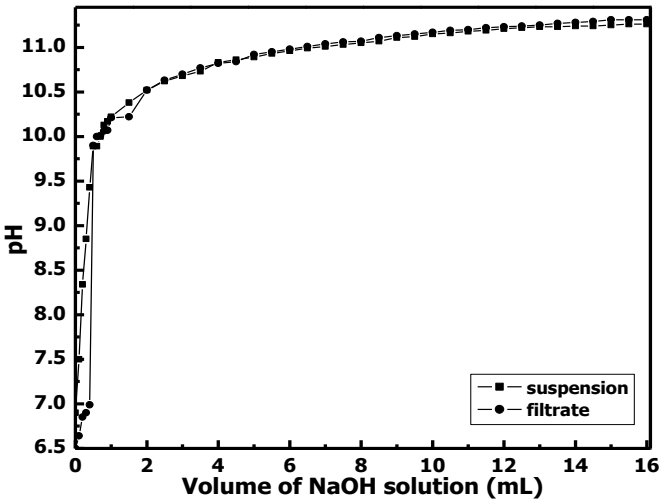

Fig.3.26: pH metric titration curves for MnO_2 nps with 1×10^{-2}M NaCl.

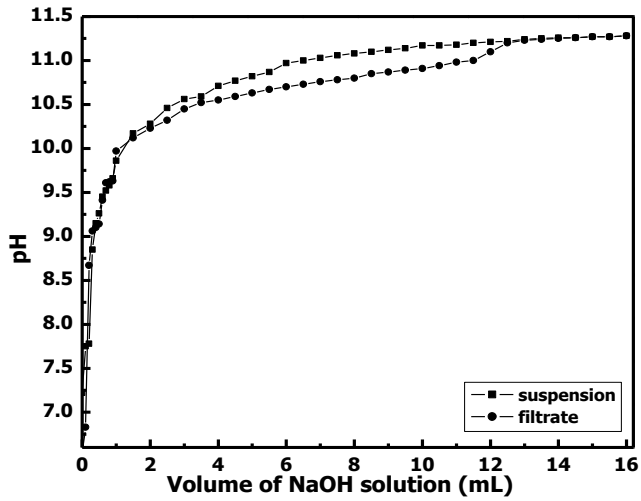

Fig. 3.27: pH metric titration curves for MnO_2 nps with 1×10^{-3} M NaCl.

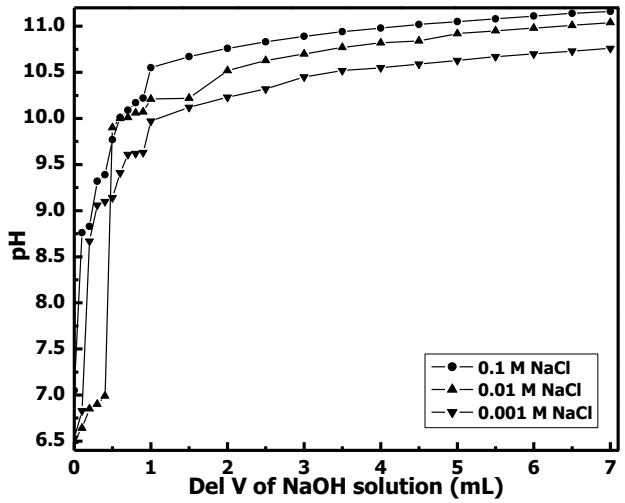

Fig.3.28: Net titration pH_{PZC} curve for MnO_2 nps in the presence of different concentrations of NaCl solution. These curves intersect at pHpzc.

3.2.8(c). Determination of point of zero charge (pH_{PZC}) of Mn_3O_4 nps

The pH metric titration data and the curves for three different concentration of NaCl solution are shown in **Table 5-6** in appendix and **Fig.3.29-3.32**. The net titration curves corresponding to three different ionic strengths are shown in **Fig.3.32**. From **Fig. 3.32**, the point of zero charge of Mn_3O_4 nps was found to be 8.75. This is also in agreement with literature [196].

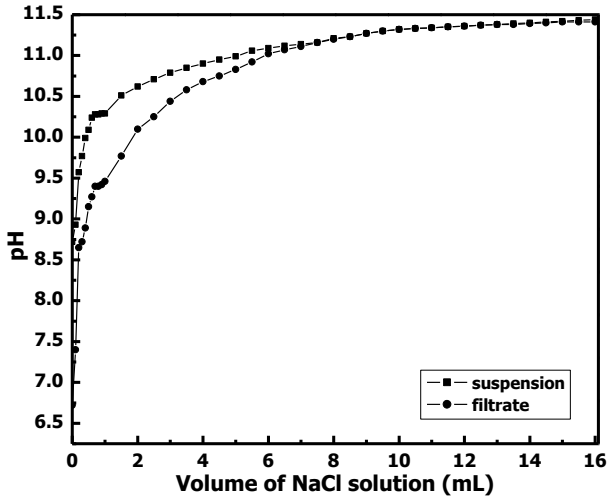

Fig. 3.29: pH metric titration curves for Mn_3O_4 with 1×10^{-1}M NaCl solution.

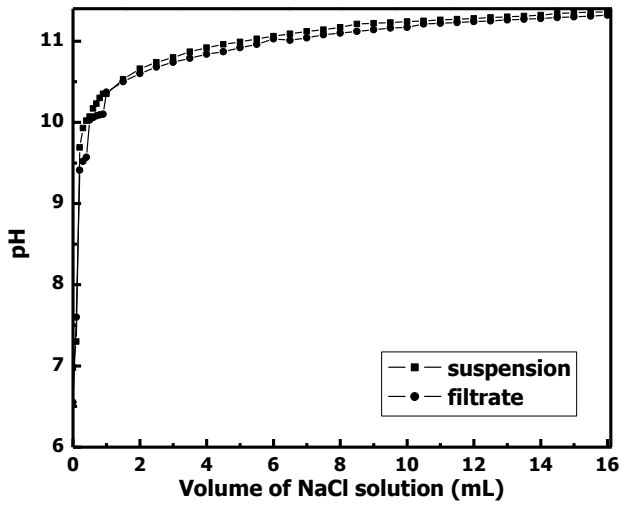

Fig. 3.30: pH metric titration curves for Mn_3O_4 with 1×10^{-2} M NaCl solution.

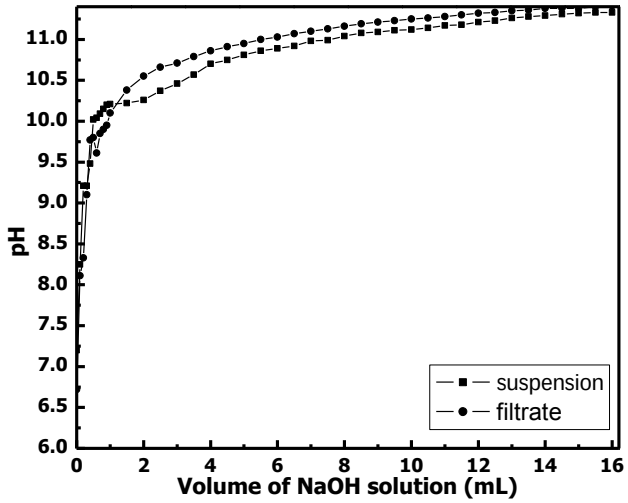

Fig. 3.31: pH metric titration curves for Mn_3O_4 with 1×10^{-3} M NaCl solution.

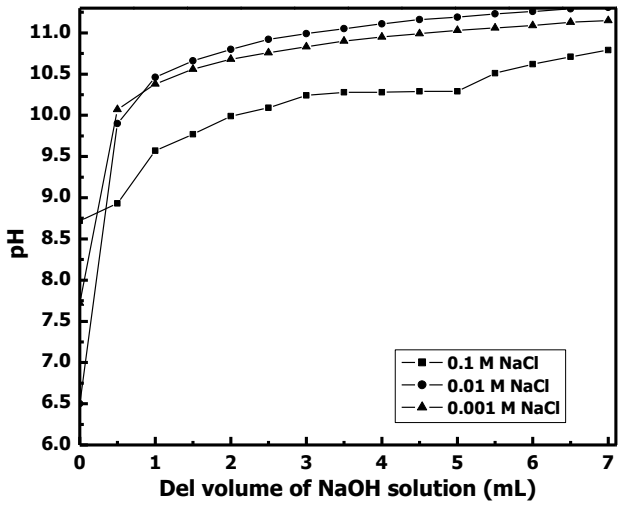

Fig.3.32: Net titration pH_{PZC} curve for Mn_3O_4 nps in the presence of different concentrations of NaCl solution. These curves intersect at pH_{pzc}.

3.3. Kinetics of MB and OG decolorization by Mn-oxide nps

Factors influencing dye oxidative decolorization via degradation could be quantitatively assessed using kinetic rate. Suitable rate expressions obtained from kinetic modeling can also allow insight into possible reaction mechanisms.

3.3.1. Effect of initial concentration and contact time for MB decolorization by γ−MnOOH nps

Table 3.4. Data for the influence of contact time for MB decolorization by γ−MnOOH nps at pH 7.20.

Amount of γ−MnOOH nps: 0.02g Volume of the solution: 10 mL

λ_{max} for MB solution: 664 nm Temperature: 27.8°C

Molar absorption coefficient=77,449 L $mol^{-1}cm^{-1}$ Reference: Water

Run No	Initial conc.$\times 10^5$ $C_0(molL^{-1})$	Time (min)	Absorbance at equilibrium	Equilibrium conc. $\times 10^6$ C_t $(molL^{-1})$	Adsorbed conc.$\times 10^6$ $q_m(molL^{-1})$	Amount adsorbed q_t (mg/g)
1	1.0	0	0.803	0.000	0.000	0.000
2		20	0.299	3.860	6.140	1.093
3		60	0.339	4.377	5.661	1.008
4		120	0.359	4.635	5.623	1.001
5		180	0.364	4.670	5.330	0.948
6		240	0.343	4.430	5.570	0.991
7		300	0.358	4.624	5.970	1.062
8		2880	0.384	4.958	5.042	0.897

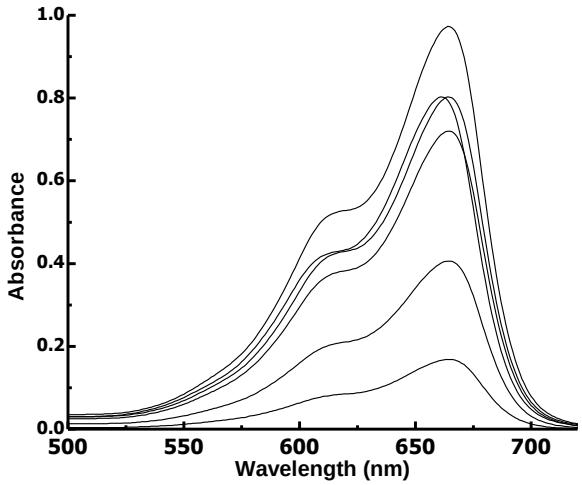

Fig. 3.33. UV–vis spectra of 1 x 10^{-5} M MB solution before and after charging γ–MnOOH nps at pH 7.20. The spectra taken at 20, 60, 120, 180, 240, 300 min and 48h after charging the nps (from upper).

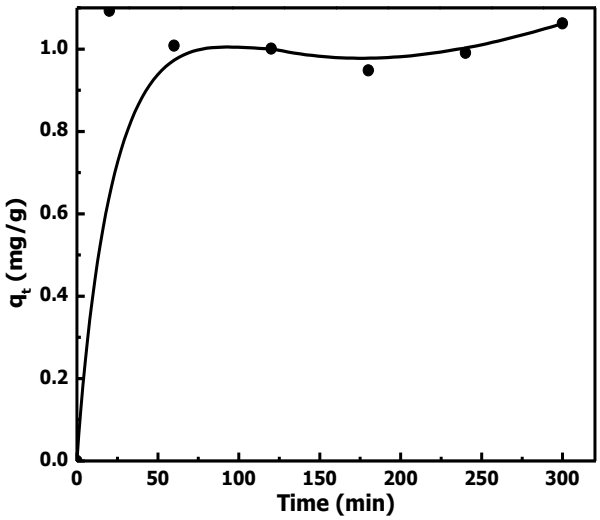

Fig.3.34. Effect of initial concentration and contact time for MB decolorization by γ–MnOOH nps (T = 300.8 K, pH_i = 7.20, amount of γ–MnOOH nps = 0.02g, $[MB]_i$ = 1.0×10^{-5} M and V= 0.01L).

3.3.2. Effect of contact time for OG decolorization by γ–MnOOH nps at pH 5.95.

Table-3.5. Data for the influence of contact time for OG decolorization by γ–MnOOH nps at pH 5.95.

Amount of γ–MnOOH nps: 0.02g Volume of the OG solution: 10 mL

λ_{max} for OG solution: 477 nm Temperature: 28°C

Molar absorption coefficient:16,168 L $mol^{-1}cm^{-1}$ Reference: Water

Run No	Initial conc.×10^5 ($molL^{-1}$)	Time (min)	Absorbance at 477 nm	Equilibrium conc.×10^5 C_t ($molL^{-1}$)	Adsorbed conc.×10^7 q_m(mol/L)	Amount adsorbed q_t (mg/g)
1	1.0	0	0.165	0.00	0.00	0.00
2		5	0.172	1.064	6.4	0.145
3		10	0.173	1.070	7.00	0.158
4		20	0.174	1.076	7.62	0.172

5		60	0.179	1.107	10.71	0.242
6		120	0.180	1.113	11.33	0.256
7		180	0.181	1.119	11.95	0.270
8		240	0.183	1.132	13.86	0.298
9		300	0.188	1.163	16.28	0.368

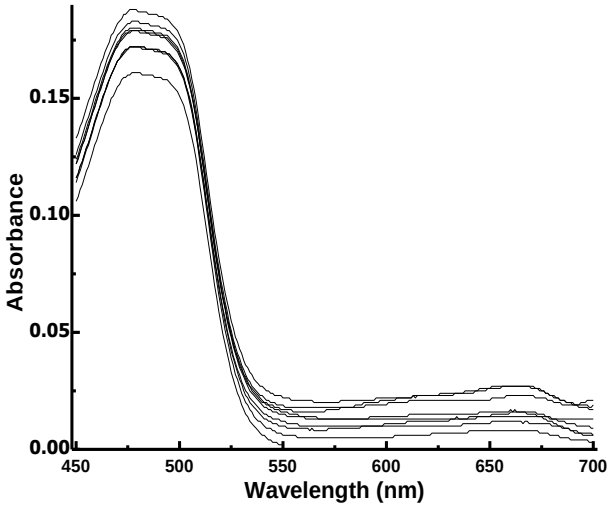

Fig. 3.35. UV–vis spectra of 1 x 10^{-5} M OG solution before and after charging the γ–MnOOH nps at pH 5.95. The spectra taken at different time intervals, *viz.,* 15, 30, 60, 90, 120, 150 min and 24 h after charging the nps (from upper).

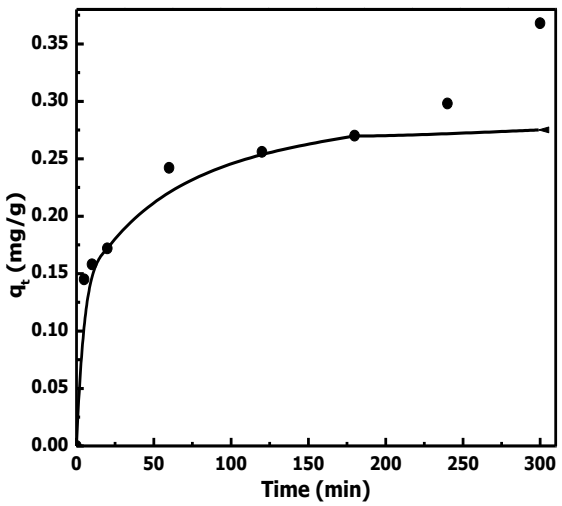

Fig. 3.36. Effect of initial concentration and contact time for OG decolorization in γ–MnOOH nps suspension (T = 301 K, pH_i = 5.95, γ–MnOOH nps dosage = 0.02g, $[OG]_i = 1.0\times10^{-5}$ M and V= 0.01L).

3.4. Kinetic models applied for dye decolorization in γ–MnOOH nps suspension

Several steps can be used to examine the controlling mechanism of adsorption process such as chemical reaction, diffusion control and mass transfer; kinetic data was used to test experimental data from the adsorption of MB and OG onto γ–MnOOH nps was required for selecting optimum operating conditions for the full-scale batch process. The kinetic parameters, which are helpful for the prediction of adsorption rate, give information designing and modeling the adsorption process. Thus, the kinetics for MB and OG decolorization by γ–MnOOH nps was analysis using pseudo-first order [73], pseudo-second order [75], intra-particle diffusion [197] and Elovich [198] kinetic models. The conformity between experimental data and model predicted values was expressed by the co-relation coefficients (R^2, values closed to equal to 1). The relative higher values are the applicable model to the kinetics for MB and OG decolorization by γ–MnOOH nps. The required derived data for these kinetics models is given below in **Table 3.6 and 3.7.**

Table 3.6. Derived data for various kinetic models for MB decolorization by γ–MnOOH nps

Dye	Time (t) (min)	Square root of contact time ($t^{1/2}$)	Adsorbed amount at time (t) q_t (mg/g)	Amount adsorbed at equilibrium time (q_{et}) (mg/g)	$\ln(q_{et} - q_t)$	t/ q_t min/(mg/g)
MB	20	4.472	1.093	1.062	-3.473	18.298
	60	7.745	1.008		-2.919	59.523
	120	10.954	1.001		-2.796	119.880
	180	13.412	0.948		-2.172	189.873

	240	15.492	0.991		-2.645	242.17
	300	17.321	1.062			
	2880	53.666	0.897			

Table 3.7. Derived data for various kinetic models for OG decolorization by γ–MnOOH nps

Dye	Time (t) (min)	$t^{1/2}$	Adsorbed amount at time (t) q_t (mg/g)	Amount adsorbed at equilibrium at time (q_{et}) q_{et} (mg/g)	$\ln(q_{et} - q_t)$	t/q_t
OG	5	2.24	0.145	0.270	-2.079	34.48
	10	3.16	0.158		-2.189	63.29
	20	4.47	0.172		-2.323	116.28
	60	7.75	0.242		-3.575	247.94
	120	10.95	0.256		-4.268	468.75
	180	13.42	0.270			
	240	15.49	0.298			
	300	17.32	0.145			

3.4.1. Pseudo-first- Order equation

The adsorption kinetics can be described by a pseudo-first order equation as suggested by Lagergren, which is the earliest known equation describing the adsorption rate based on the adsorption capacity:

$$\frac{dq}{dt} = k_1(q_e - q_t)$$

Where, k_1 (min^{-1}) is the rate constant of the pseudo-first order model, q_t (mg/g) denotes the amount of adsorbed at time t (min), and q_e (mg/g) is the amount of adsorption at equilibrium. After definite integration by application of the conditions t = 0 to t = t and q = 0 to q = q_e, the above equation becomes

$$\ln(q_e - q_t) = \ln q_e - k_1 t$$

Where, q_{et} and q_t are the adsorption capacity at equilibrium and at time t, respectively (mg/g), k_1 is rate constant of pseudo-first- order adsorption (L/mg).

In order to obtain the rate constants, the values of $\ln(q_{et}-q_t)$ were linearly correlated with t by plot of $\ln(q_{et}-q_t)$ versus t to give a linear relationship. k_1 and predicted q_{et} can be determined from the slope and intercept of the plot, respectively **[Fig.3.23 and 3.24]**. The variation in rate should be proportional to the first power and concentration for strict surface adsorption. However, the relationship between initial solute concentration and rate of adsorption will not be linear when pore diffusion limits the adsorption process.

Fig. 3.37 shows that the pseudo-first-order equation fits well for the first 60 min both MB decolorization process and thereafter the data deviate from theory. Thus, the model represents the initial stages where rapid adsorption occurs well but cannot be applied for the entire adsorption process. Furthermore, the correlation co-efficient R^2 are relatively low **(Table 3.8)**. This shows that MB decolorization by γ–MnOOH nps cannot be applied and the reaction mechanism is not a first order reaction.

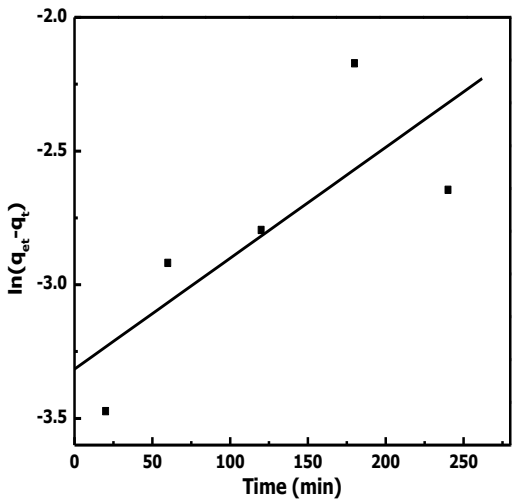

Fig.3.37. Pseudo first order kinetics for MB decolorization by γ–MnOOH nps for entire process.

On the other hand, pseudo first order kinetics for OG decolorization by γ–MnOOH nps fits well in about 30 min as shown in **Fig. 3.38** which is rapid process and cannot be applied. Therefore, reaction is not first order.

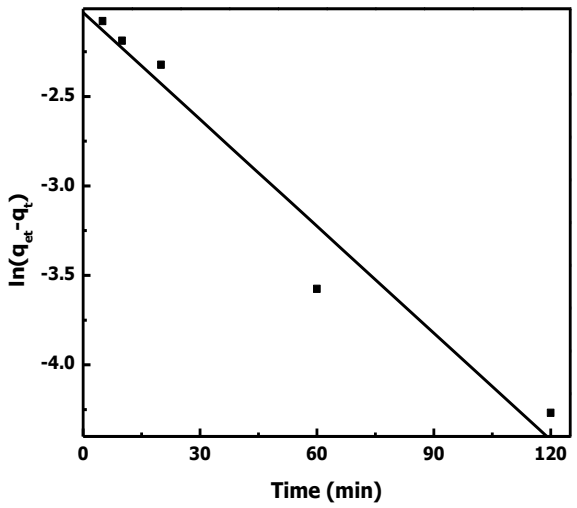

Fig. 3.38. Pseudo first order kinetics for OG decolorization by γ–MnOOH nps for entire process.

3.4.2. Pseudo-second-order equation

The adsorption kinetic may be described by the pseudo-second-order model.

The pseudo-second order equation developed by Ho can be written as

$$\frac{dq}{dt} = k_2(q_e - q_t)^2$$

Where; k_2 [g (mg min)$^{-1}$] is the rate constant of the pseudo second order. Integrating the equation for the boundary conditions t = 0 to t = t and q = 0 to q = q_e gives

$$\frac{1}{(q_e - q_t)} = \frac{1}{q_e} + k_2 t$$

The above equation is generally given as follows:

$$\frac{t}{q_t} = \frac{1}{k_2 q_e^{\,2}} + \frac{1}{q_e} t$$

K_2 and q_e can be obtained from the intercept and slope of t/q_t vs. t plot. If the pseudo-second-order kinetic [199] is applicable, then the plot of t/q_t versus t should show a linear relationship and the values of k_2 and equilibrium adsorption capacity q_{et} were calculated from the intercept and slope of the plots of q_t versus t. The linear plots of t/q_t versus t show good agreement between experimental and calculated q_{et} values for MB and OG decolorization by γ–MnOOH nps **(Fig. 3.39 and 3.40)**. The correlation coefficient for the pseudo-second-order kinetic model are very close to 1 that is 0.999 which led to believe that the pseudo-second-order kinetic model provided good correlation for OG decolorization by γ–MnOOH nps **(Table 3.8)**.

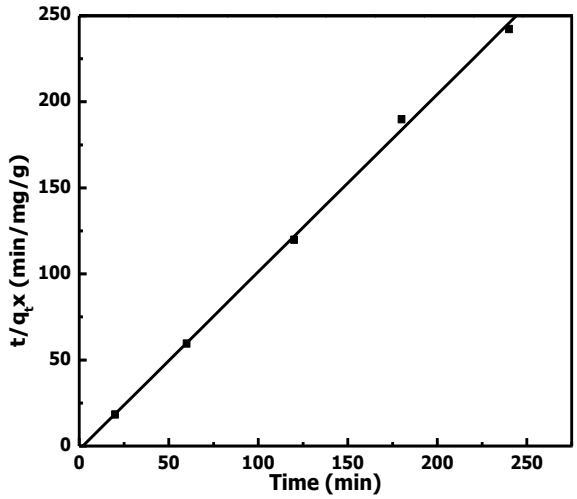

Fig. 3.39: A plot of pseudo-second- order- Kinetics for MB decolorization by γ–MnOOH nps.

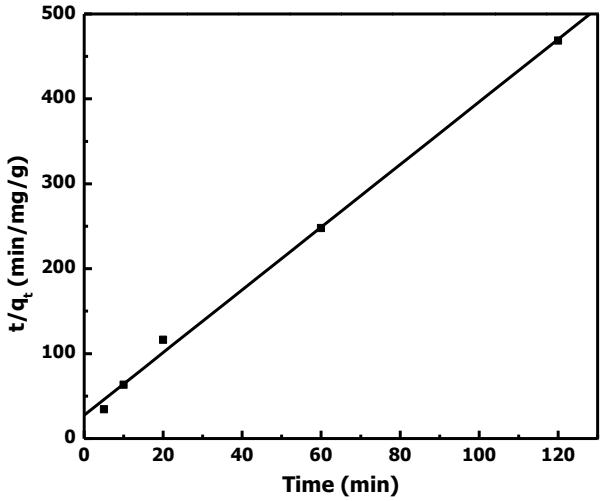

Fig.3.40: A plot of pseudo-second- order- Kinetics for OG decolorization by γ−MnOOH nps.

Table-3.8. Comparison of the first and second order rate constants and calculated and experimental q_{et} values for MB and OG decolorization by γ−MnOOH nps

Parameter→ Dye ↓	Experimental q_{et} (mg/g)	Pseudo-first-order kinetic model (Calculated)			Pseudo-second-order kinetic model (Calculated)		
		$k_1 \times 10^2$	q_{et} (mg/g)	R^2	$k_2 \times 10^2$	q_{et} (mg/g)	R^2
MB	1.062	4.20	0.0363	0.78	52.4	0.968	0.99
OG	0.270	1.99	0.131	0.98	27.1	0.494	0.99

3.4.3. Intra-particle diffusion model

The adsorbate species are most probably transported from the bulk of the solution into the solid phase through intra-particle diffusion or transport process [199], which is often the rate limiting step in many adsorption processes, especially in a rapidly stirred batch reactor. Since the dyes are probably transported from its aqueous solution to γ−MnOOH nps by intra-particle diffusion, so the intra-particle diffusion is another kinetic model should be used to study the rate for dye decolorization by γ−MnOOH nps. The possibility of intra-particle diffusion was explored by using the intra-particle diffusion model, which is commonly expressed by the following equation:

$$q_t = k_{diff}\ t^{1/2} + C$$

Where, C (mg/g) is the intercept and k_{diff} rate constant (mg/g $min^{1/2}$). The values of q_t were found to be linearly correlated with values of $t^{1/2}$ and rate constant k_{diff} directly evaluated from the slope of the regression line (**Fig. 3.41 and 3.42)**. The values of intercept C **(Fig. 3.41 and 3.42)** provide information about thickness of the boundary layer, the resistance to the external mass transfer increase as the intercept increase. The R^2 values given in **Table 3.9** are 0.84 for MB and 0.97 for OG indicating the application of this model. This may confirm

that the rate limiting step may be intra-particle diffusion process [82]. The linearity of the plots demonstrated the intra-particle diffusion played a significant role in the uptake of the adsorbate by adsorbent.

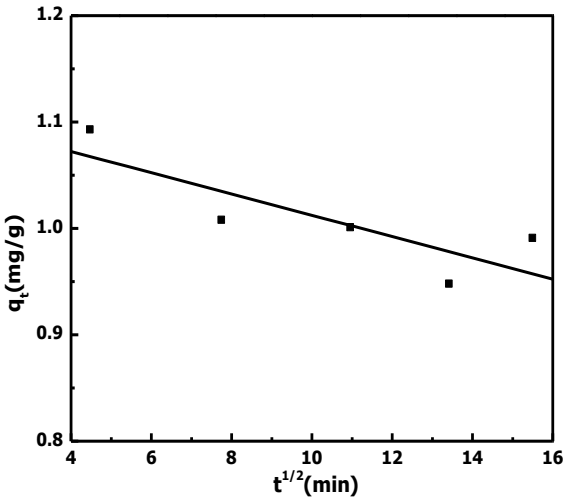

Fig.3.41: A plot of intra-particle diffusion model for MB decolorization by γ−MnOOH nps.

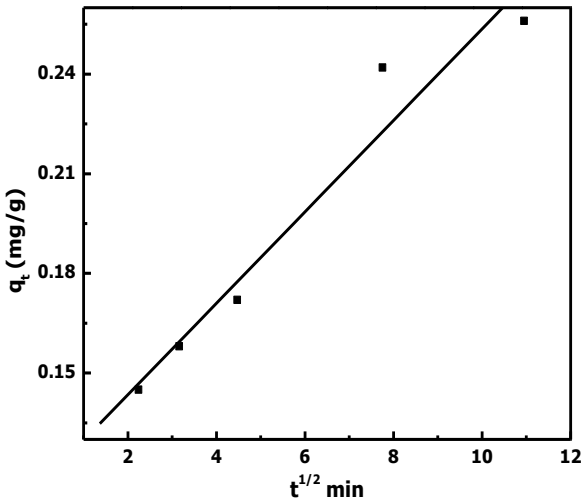

Fig. 3.42: A plot of intra-particle diffusion model for OG decolorization by γ−MnOOH nps.

Table 3.9: The parameters obtained from intra-particle diffusion model for MB and OG decolorization by γ–MnOOH nps

Dye	Parameters of intra-particle diffusion model		
	k_{diff} (mg/g $min^{1/2}$)	C (mg/g)	R^2
MB	0.010	1.11	0.84
OG	0.014	0.16	0.97

3.4.4. Elovich model

In reactions involving chemisorption of adsorbate on a solid surface without desorption of products, adsorption rate decreases with time due to an increased surface coverage. One of the most useful models for describing such 'activated' chemisorption is the Elovich equation. The Elovich equation can be written as:

$$q = \frac{1}{\alpha}\ln(\alpha\beta) + \frac{1}{\alpha}\ln t$$

Where, α is the initial adsorption rate, and β is the desorption constant during each experiment. **Fig. 3.43 and 3.44** show plots of Elovich for OG decolorization by γ–MnOOH nps. The linear regressions (R^2) values are relatively lower (0.51 and 0.31 for MB and OG respectively) (**Table 3.10**). Therefore, Elovich model is not applicable.

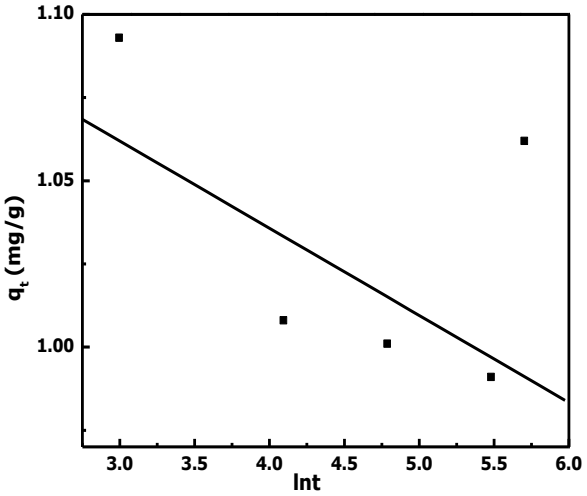

Fig. 3.43: A plot of Elovich model for MB decolorization by γ–MnOOH nps.

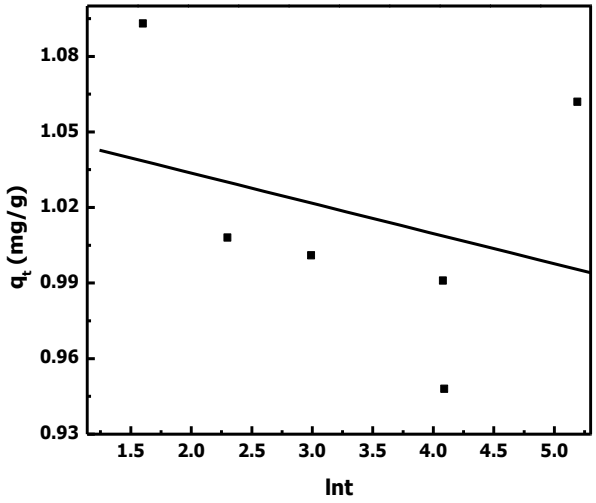

Fig. 3.44: A plot of Elovich model for OG decolorization by γ−MnOOH nps.

Table 3.10: The values of parameters and correlation coefficient of Elovich model for OG decolorization by γ−MnOOH nps

Dye	Parameters of Elovich model		
	α	β	R^2
MB	38.168	$2.106x10^{17}$	0.51
OG	83.333	$2.274x10^{36}$	0.31

3.5. Determination of specific surface area of γ−MnOOH nps in MB decolorization method

Analysis of monolayer capacity and surface area

In monolayer adsorption all the adsorbed molecules are in contact with the surface layer of the adsorbent. The monolayer capacity is defined as the amount of adsorbate which is needed to occupy all adsorption sites as determined by the structure of the adsorbent and by the chemical nature of the adsorbate and for physical adsorption, as the amount needed to cover the surface with a single monolayer of molecules in close –packed.

Monolayer capacity can be predicted from an experimental isotherm obtained by adopting adsorption process. In the present research, the adsorbate MB and

OG were allowed to decolorize by γ–MnOOH nps. The progress of MB and OG decolorization with time on the above mentioned adosrbent was monitored spectrophotometrically. Langmuir equation is applied to the experimental adsorption data to estimate the monolayer capacity.The surface area of an adsorbent can be determined by knowing the value of monolayer capacity and the cross sectional area of the adsorbed molecule. In order to evaluate the monolayer capacity and surface area of the γ–MnOOH nps, the results of MB adsorption at room temperature at different pH are presented in the **Table 3.11(a-c) and 3.12 and Fig.3.45-3.48** respectively.

3.5.1. Determination of monolayer capacity for MB decolorization by γ–MnOOH nps

Amount of γ–MnOOH nps: 0.02g Volume of each MB solution : 10 mL

Shaking time : 180 min Centrifuge time: 10 min

Molar absorption co-efficient : 77,449 L $mol^{-1}cm^{-1}$ Temperature: 28^0C

Table 3.11 (a): The amount of MB decolorized in γ–MnOOH nps suspension at equilibrium concentration of MB at pH 3.03

Initial conc.×10^6 C_0 ($molL^{-1}$)	Final abs	Equilibrium conc.×10^6 C_e ($molL^{-1}$)	Equilibrium conc. C_e (mg/L)	Adsorbed conc. C_o-C_e×10^6 ($molL^{-1}$)	Amount adsorbed q_e(mg/g)	C_e/q_e g/L
5.0	0.351	4.532	1.613	4.679	0.833	1.936
8.0	0.450	5.810	2.068	2.189	0.389	5.312
10.0	0.594	7.502	2.670	2.498	0.444	6.012
15.0	0.793	10.239	3.644	4.761	0.847	4.300
20.0	0.992	12.808	4.558	7.192	1.595	2.858
25.0	1.429	18.451	6.566	6.549	1.279	5.134
30.0	1.679	21.679	7.715	8.321	1.481	5.210
40.0	2.169	28.008	9.967	11.994	2.134	4.670

Table 3.11(b): The amount of MB decolorized by γ−MnOOH nps at equilibrium concentration of MB at pH 7.92

Initial conc.×10^6 ($molL^{-1}$)	Final Abs	Equilibrium conc.×10^6 ($molL^{-1}$)	Equilibrium conc. (mgL^{-1})	Adsorbed conc.×10^6 ($molL^{-1}$)	Amount adsorbed q_e(mg/g)	C_e/q_e (g/L)
5.0	0.285	3.679	1.309	0.967	0. 172	7.601
8.0	0.434	5.603	1.994	1.682	0.299	6.662
10.0	0.498	6.430	2.292	3.569	0.635	3.602
15.0	0.838	10.820	3.851	4.179	0.743	5.179
20.0	1.087	14.035	4.995	5.964	0.107	4.707
25.0	1.383	17.857	6.355	7.143	1.271	4.999
30.0	1.644	21.226	7.554	8.773	1.561	4.839
40.0	2.235	28.857	10.269	11.142	1.983	5.179

Table 3.11(c): The amount of MB decolorized by γ−MnOOH nps at equilibrium concentration of MB at pH 11.36

Initial conc.×10^6 ($molL^{-1}$)	Final Abs	Equilibrium conc.×10^6 ($molL^{-1}$)	Equilibrium conc. (mgL^{-1})	Adsorbed conc.×10^6 ($molL^{-1}$)	Amount adsorbed (q_e)(mg/g)	C_e/q_e (g/L)
5.0	0.230	2.969	1.056	2.031	1.016	1.039
8.0	0.362	4.674	1.663	3.326	1.663	1.000
10.0	0.483	6.236	2.219	3.764	1.881	1.179
15.0	0.729	9.413	3.349	5.587	2.794	1.198
20.0	0.938	12.111	4.310	7.889	3.944	1.093
25.0	1.148	14.822	5.275	10.177	5.088	1.036
30.0	1.523	19.665	6.998	10.335	5.167	1.354
40.0	1.867	24.106	8.579	15.894	7.947	1.079

3.5.2. Determination of monolayer capacity for OG decolorization by γ−MnOOH nps

Table 3.12: The amount of OG decolorized by γ−MnOOH nps at equilibrium concentration of OG at pH 5.95

Amount of γ−MnOOH nps: 0.02g Volume of each solution : 10 mL

Shaking time : 120 min Centrifuge time: 10 min

Molar absorption co-efficient: 16,168 L mol^{-1} cm^{-1} Temperature: 28^0C

Initial conc.$\times10^6$ ($molL^{-1}$)	Final abs	Equilibrium conc.$\times10^6$ ($molL^{-1}$)	Equilibrium conc. (mgL^{-1})	Adsorbed conc.$\times10^7$ ($molL^{-1}$)	Amount adsorbed (q_e)(mg/g)	C_e/q_e (g/L)
5.0	0.087	5.381	2.434	3.810	0.0862	28.237
8.0	0.128	7.917	3.581	8.313	0.0188	190.478
10.0	0.165	10.205	4.617	2.053	0.0464	99.504
15.0	0.225	13.916	6.295	10.84	0.2451	25.683
20.0	0.313	19.359	8.757	6.408	0.1449	8.612
25.0	0.391	24.183	10.939	8.164	0.1847	59.227
30.0	0.475	29.379	13.290	6.209	0.1405	94.591
40.0	0.645	39.894	18.047	1.064	0.0241	748.838

3.6. Equilibrium isotherm analysis

The parameters obtained from the different kinetic models provided important information on the adsorption mechanism and the surface properties and affinities of the adsorbent. The most widely accepted surface adsorption models for single solute systems are the Langmuir, Freundlich, Temkin and Sips models. The correlation with the amount of adsorption and the liquid-phase concentration was tested with the Langmuir, Freundlich, Temkin and Sips equations. Linear regression (R^2) was used to determine the best-fitting isotherm, and the applicability of isotherm equations was compared by judging the correlation coefficients.

3.6.1. Langmuir isotherm

The Langmuir isotherm model is used to predict the sorption of aqueous compounds onto a solid phase. This mechanistic model assumes that a monolayer of adsorbed material (in liquid, such as MB) is adsorbed over a uniform adsorbent surface (a flat surface of solid phase, such as Mn-oxide) at a constant temperature and that the distribution of the compound between the two phases is

controlled by equilibrium constant. Hence, at equilibrium both rates of adsorption and desorption are equal.

The theoretical Langmuir isotherm is valid for adsorption of a solute from a liquid solution as monolayer adsorption on a surface containing a finite number of identical sites. Langmuir isotherm model assumes uniform energies of adsorption onto the surface without transmigration of adsorbate in the plane of surface [200]. Therefore, the Langmuir isotherm model was chosen for estimation of the maximum adsorption capacity corresponding to complete monolayer coverage on the adsorbent surface. The Langmuir equation is derived as:

$$q_e = \frac{q_m K_L C_e}{1 + K_L C_e}$$

Where, C_e is the equilibrium concentration (mg/L); q_e is the amount adsorbed (mg/g); q_m is a constant and reflects a complete monolayer (mg/g), k_L is a adsorption equilibrium constant (L/mg) that is related to the apparent energy of adsorption. Both q_m and K_L will greatly impact the conclusions made about the experimental data and can be determined by a simple method of equation optimization by linear regression. That is to transform the isotherm variables to a linear form and then to apply the linear regression analysis of known q_e and q_e values as described by Line-weaver-Burk (Langmuir-II). The linear form of Langmuir equation is commonly expressed as followed:

$$\frac{1}{q_e} = \left(\frac{1}{K_L q_m}\right)\frac{1}{C_e} + \left(\frac{1}{q_m}\right)$$

A plot of C_e/q_e versus C_e should indicate a straight line slope of $1/q_m$ and intercept $1/K_L q_m$.

Separation factor for Langmuir isotherm

For the Langmuir equation the favorable nature of adsorption can be expressed in terms of dimensionless separation factor of equilibrium parameter, which is defined by:

$$R_L = \frac{1}{1 + K_L C_0}$$

Where, K_L is the Langmuir constant and C_0 is the initial concentration of the adsorbate in solution. The values of R_L indicates the type of isotherm to be irreversible (R_L = 0), favorable ($0<R_L< 1$), linear (R_L =1) or unfavorable ($R_L>1$). R_L values for methylene blue adsorption onto mixed Mn-oxide at different temperature were less than 1 and greater than zero indicating favorable adsorption.

Fig. 3.47-50 shows Langmuir isotherm and linear plots for MB decolorization by γ−MnOOH nps at different pH.

The results obtained from the Langmuir model are shown in **Table 3.13.** The correlation coefficients showed evidence on for MB decolorization by γ−MnOOH nps did not follow the Langmuir isotherm well (**Table 3.13**). The applicability of the linear form of Langmuir model to γ−MnOOH nps was proved by the lower correlation coefficients. This suggests that the Langmuir isotherm did not provide a good model of the adsorption system. The maximum monolayer capacity q_m obtained from the Langmuir isotherm are also shown in **Table 3.13** for MB and OG.

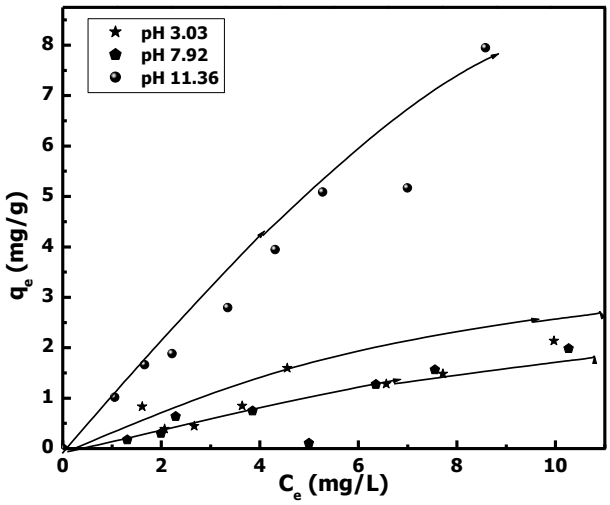

Fig. 3.45: Langmuir isotherm for MB decolorization by γ−MnOOH nps at different pH.

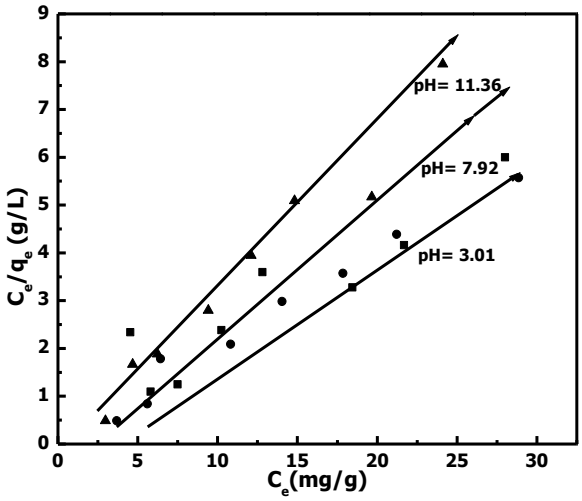

Fig. 3.46: Linear plot of C_e/q_e vs. Ce for for MB decolorization by γ–MnOOH nps.

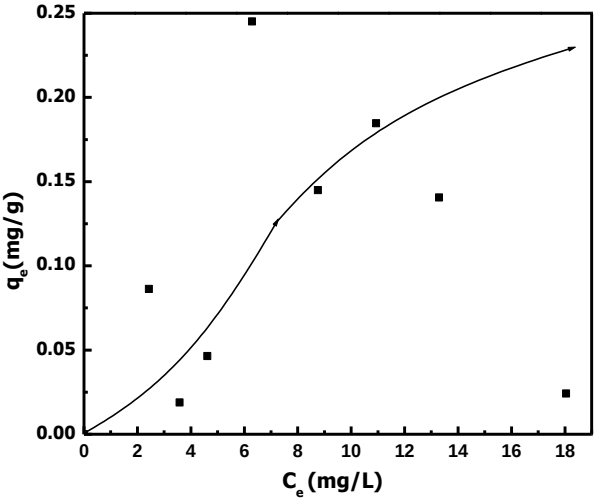

Fig. 3.47. Langmuir isotherm for OG decolorization by γ–MnOOH nps.

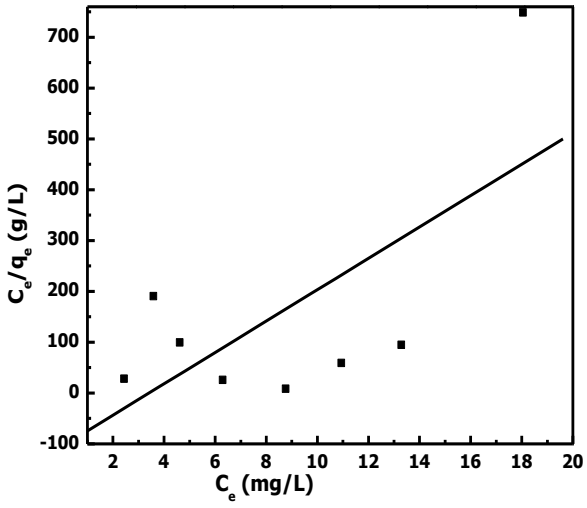

Fig.3.48. Linear plot of Ce /q_e vs. Ce for OG decolorization by γ–MnOOH nps.

Table-3.13. Langmuir parameters for MB and OG decolorization by γ–MnOOH nps

Dye	pH	q_m (mg/g)	k_L (L/mg)	R^2	R_L
MB	3.01	8.296	0.0313	0.30	0.999
	7.92	18.89	0.0087	0.35	0.999
	11.36	64.98	0.0052	0.38	0.999
OG	5.95	0.032	0.293	0.67	0.999

Calculation of surface area of γ–MnOOH nps surface

The adsorption of MB onto γ–MnOOH nps follows Langmuir–Hinshelwood isotherm at pH 11.36 at room temperature (R^2= 0.35). From the Langmuir-Hinshelwood plot of C_e/q_e vs. Ce, it has been found that monolayer capacity q_m = 64.98 mg/g that obtained from the slope and adsorption constant K_L =0.0052 L/mg that obtained from the intercept. Then the specific surface area (S_{MB}) of γ–MnOOH nps was calculated from the equation

$$S_{MB} = (q_m /M) \times N_a \times A_{MB} \times 10^{-20}\ m^2\ g^{-1}$$

Where, N_a = Avogadro's number = 6.023× 10^{23},

A_{MB} = Cross sectional area of MB = occupied surface area of one molecule of MB.

q_m = Monolayer capacity= number of molecules of MB adsorbed at the monolayer of γ–MnOOH nps in mg/g = 64.98 mgg^{-1} = 64.98 × 10^{-3}

Molecular mass of MB, M = 355.89 $gmol^{-1}$

(i) Cross sectional area of MB (A_{MB})= 130 A^{02} BET with N_2

(ii) Cross sectional area of MB (A_{MB})= 178 A^{02} BET with N_2

Specific surface area, S_{MB} =?

(i) $S_{MB} = (64.98 \times 10^{-3} / 355.89) \times 6.023 \times 10^{23} \times 130 \times 10^{-20} = 142.96\ (m^2 g^{-1})$

(ii) $S_{MB} = (64.98 \times 10^{-3} / 355.89) \times 6.023 \times 10^{23} \times 178 \times 10^{-20} = 195.75\ (m^2 g^{-1})$

The specific surface area of γ–MnOOH nps at pH 7.92 and room temperature are found to be 142.96 and 195.75 ($m^2 g^{-1}$) respectively.

3.6.2. Freundlich isotherm

The Freundlich isotherm model [201] is the earliest known equation describing the adsorption process. It is an empirical equation and can be used for non-ideal sorption that involves heterogeneous adsorption. The Freundlich isotherm can be derived assuming a logarithmic decrease in the enthalpy of adsorption with the increase in the fraction of occupied sites and is commonly given by the following linear equation:

$$q_e = K_F C_e^{\frac{1}{n}}$$

$$\text{Or, } \ln q_e = \ln k_F + \frac{1}{n} \ln C_e$$

Where, K_F is a constant for the system, related to the bonding energy. K_F can be defined as the adsorption or distribution coefficient and represents the quantity of dye adsorbed onto adsorbent for unit equilibrium concentration. $1/n$ is indicating the adsorption intensity of dye onto the adsorbent or surface heterogeneity, becoming more heterogeneous as its value gets closer to zero. A value for $1/n$ below 1 indicates a normal Langmuir isotherm while $1/n$ above 1 is indicative of cooperative adsorption.

The applicability of the Freundlich adsorption isotherm was analyzed, using the same set of experimental data, by plotting $\ln q_e$ versus $\ln C_e$ as shown in **Fig.3.49 and 3.50**. The data obtained from linear Freundlich isotherm plots for MB and OG decolorization in γ−MnOOH nps suspension is presented in **Table 3.14**. The correlation coefficients (R^2) showed that the Freundlich model is comparable to the Langmuir model. The $1/n$ is lower than 1.0, indicating that MB and OG are favorably decolorized in γ−MnOOH nps.

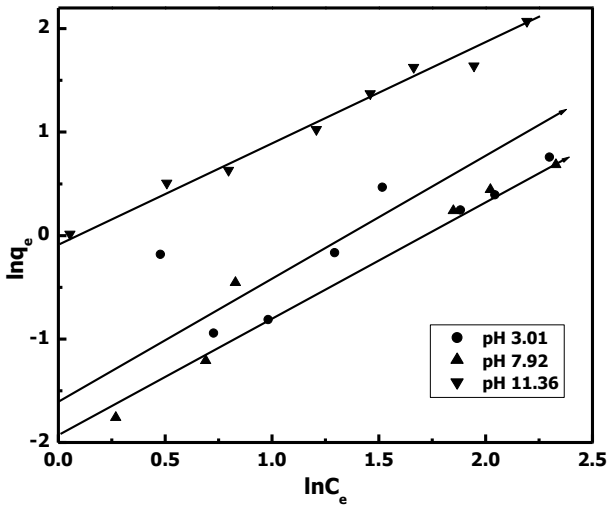

Fig. 3.49: Freundlich isotherm for MB decolorization by γ−MnOOH nps at different pH.

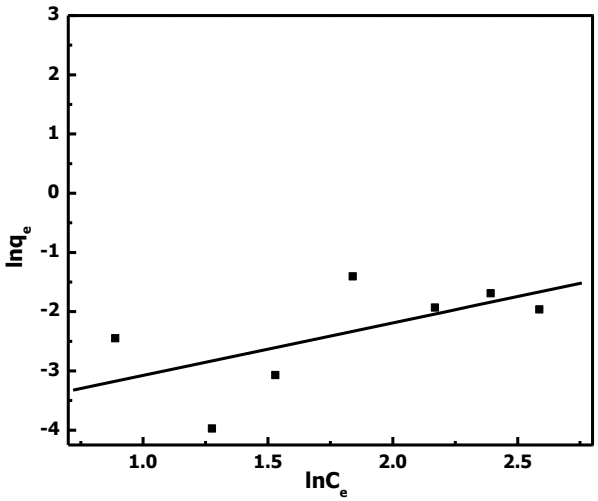

Fig. 3.50: Freundlich isotherm for OG decolorization by γ−MnOOH nps.

Table 3.14. Freundlich parameters for the adsorption of MB onto γ–MnOOH nps surface

Dye	pH	K_F (L/mg/g)	R^2	1/n
MB	3.01	0.331	0.82	0.77
	7.92	0.114	0.60	1.00
	11.36	0.966	0.99	0.93
OG	5.95	0.019	0.61	0.89

3.6.3. Temkin Isotherm

Temkin isotherm model was used also to test the decolorization potential of γ–MnOOH nps to MB and OG. This model is taking into account the effects of indirect adsorbate/adsorbate interactions on the adsorption process. Furthermore, the model is assuming that the heat of adsorption of all molecules in the layer decreased linearly by increase the coverage. The linear form of Temkin is given as follows:

$$q_e = \frac{RT}{b_T}\ln K_T + \frac{RT}{b_T}\ln C_e$$

It can be also written as

$$q_e = \frac{RT}{b}\ln(K_T C_e)$$

This may be written as

$$q_e = B_1 \ln(K_T C_e)$$

Where, R is universal gas constant, T is the absolute temperature, $1/b_T$ is the Temkin constant related to the heat of adsorption (kJ/mol) which indicates the adsorption potential (intensity) of the adsorbent and K_T (L/g) is the Temkin constant related to adsorption capacity. The linear plots of q_e vs. $\ln C_e$ enable to determine the constants $1/b_T$ and K_T from the slope and intercept respectively.

Temkin adsorption isotherm was chosen to fit with the equilibrium adsorption data. The linear plot of the Temkin isotherm at 303 K was illustrated in **Fig. 3.51 and 3.52**. The parameters, T_K and b_T of the Temkin equation have been calculated for MB and OG (**Table3.15**). The values of both adsorption capacity,

K_T and b_T are lower but linear regressions were higher. Therefore, the data of equilibrium isotherms for dye decolorization in γ−MnOOH nps suspension was well described by the Temkin model. But in case of OG both K_T and b_T were higher but linear regressions were lower. Therefore, the data of equilibrium isotherms for OG decolorization by γ−MnOOH nps was poorly described by the Temkin model.

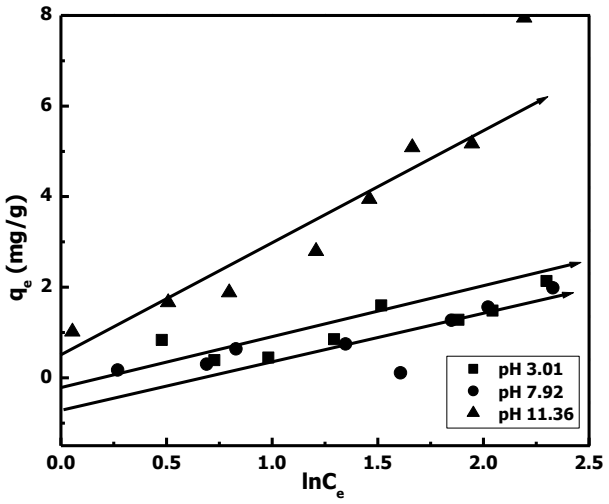

Fig.3.51. Temkin adsorption isotherm for MB decolorization by γ−MnOOH nps. (T= 303K, γ−MnOOH nps = 0.02g, $[MB]_i$ = 5-40×10^{-6} molL^{-1}, pH_i = 3.01, 7.92 and 11.36).

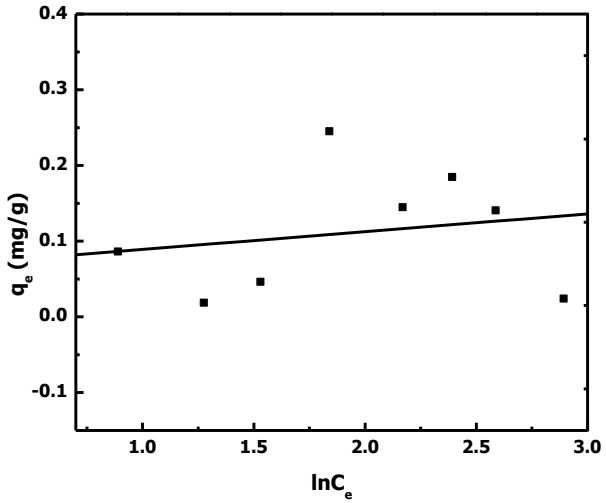

Fig.3.52. Temkin adsorption isotherm for OG decolorization by γ–MnOOH nps (T= 303K, γ–MnOOH nps = 0.02g, $[OG]_0$ = 5-40×10^{-6} $molL^{-1}$, pH = 5.95).

Table-3.15. Temkin parameters for OG decolorization by γ–MnOOH nps

Dye	pH	K_T (Lmg^{-1})	R^2	B_T ($kJmol^{-1}$)
MB	3.01	1.016	0.86	1.26
	7.92	1.167	0.99	0.91
	11.36	1.36	0.99	0.89
OG	5.95	16.32	0.20	42.57

3.6.4. Sips isotherm

Sips isotherm [198] is a combination of the Langmuir and Freundlich isotherm type models and expected to describe heterogeneous surfaces much better. At low adsorbate concentrations it reduces to a Freundlich isotherm, while at high adsorbate concentrations it predicts a monolayer adsorption capacity characteristic of the Langmuir isotherm. The model can be written as

$$q_e = \frac{q_m a_s C_e^{\frac{1}{n}}}{1 + a_s C_e^{\frac{1}{n}}}$$

Where, q_m is monolayer adsorption capacity (mg g^{-1}) and a_s is Sips constant related to energy of adsorption and parameter n could be regarded as the parameter characterizing the system heterogeneity.

The linear form of the equation is

$$C_e^{1/n}/q_e = 1/a_s q_m + C_e^{1/n}/q_m$$

A plot of $C_e^{1/n}/q_e$ vs. $C_e^{1/n}$ should yield a straight line and the values of a_s and q_m can be calculated from intercept and slope. **(Fig. 3.53 and 3.54)** showed that the plots are not linear **(Table 3.16)**. Therefore, Sips isotherm cannot be applied for MB and OG decolorization by γ–MnOOH nps.

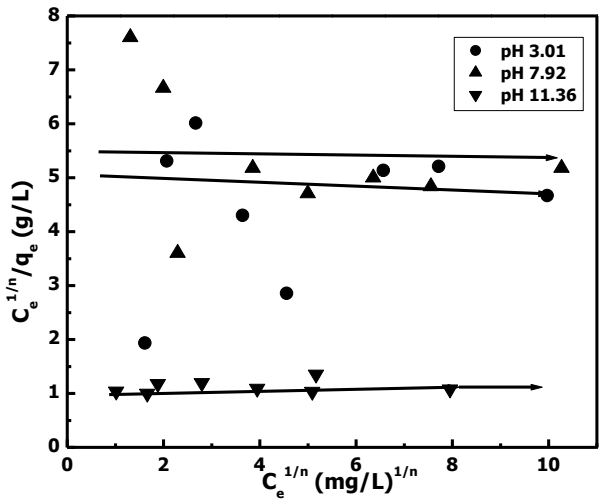

Fig.3.53. Sips isotherm for MB decolorization by γ–MnOOH nps (T= 303K, γ–MnOOH nps = 0.02g, $[MB]_0$ = 5-40×10^6 molL^{-1}, pH = 3.01).

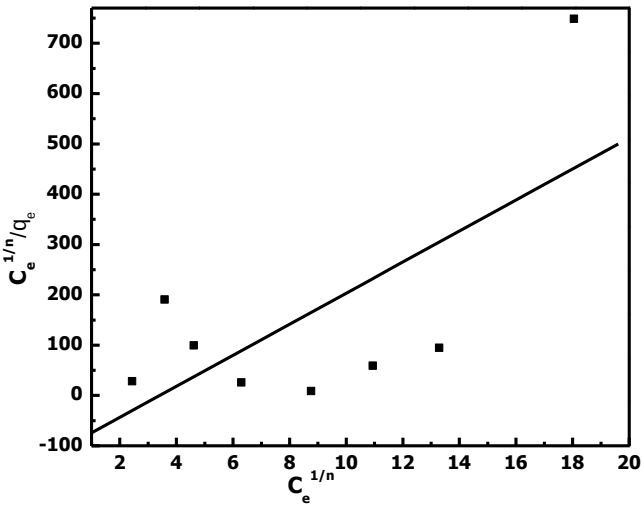

Fig.3.54. Sips isotherm for OG decolorization by γ–MnOOH nps (T= 303K, γ–MnOOH nps = 0.02g, $[OG]_0$ = 5-40×10^{-6} molL^{-1}, pH = 3.01).

Table 3.16. Sips parameters for MB and OG decolorization in γ−MnOOH nps

Dye	pH	q_m (mg/g)	a_s	R^2	n
MB	3.01	8.296	0.0313	0.30	0.376
	7.92	6.720	0.0255	0.38	0.345
	11.36	27.716	0.0361	0.35	0.245
OG	5.95	0.0324	0.2932	0.67	0.152

3.7. Effect of pH for MB and OG decolorization by γ−MnOOH nps

The pH of the solution may also affect decolorization of MB and OG. The effect of pH on the rate of decolorization of MB and OG was investigated in the pH range 3.0-12.0. Solutions were irradiation by UV light for given time interval and the percentage of removal was determined [62]. Initial pH was adjusted by adding HCl and NaOH (0.05M).The results are reported in **Table 3.17 and 3.24.**

3.7.1. Effect of pH for MB decolorization by γ−MnOOH nps

Table-3.17. Data for the influence of pH for MB decolorization by γ−MnOOH nps

Reference: Water Amount of γ−MnOOH nps: 0.02g

Volume of the solution: 10mL Temperature: 28°C

Shaking time: 300 min Molar adsorption co-efficient: 77,449 $Lmol^{-1}cm^{-1}$

Run No	Initial conc.×10^5 ($molL^{-1}$)	pH	Absorbance at 664 nm	Equilibrium conc.×10^6 q_e $molL^{-1}$	Adsorbed conc.×10^6 q_m $molL^{-1}$	Amount Adsorbed q_e (mg/g)	% of MB Removal
1	1.0	3.01	0.594	7.502	2.498	0.445	24.98
2		7.92	0.498	6.430	3.569	0.635	35.69
3		11.36	0.483	6.236	3.764	0.669	37.64

The pH of the system exerts profound influence on the adsorptive uptake of adsorbate molecules presumably due to its influence on the surface properties of the adsorbent and ionization or dissociation on the adsorbate molecule. Despite of the importance of pH, pH control is not easily maintained. **Fig.3.55** shows the variations on the removal of dyes from synthetic solution at different pH. From the figure it is evident that the amount of adsorbed MB dye per gram adsorbent is the highest at pH 11.36 **(Table 3.17)**. The amount of adsorbed cationic dye (MB) per gram adsorbent is low in acidic condition. This indicates the strong force of attraction between the dyes and γ−MnOOH nps during the adsorption process. In the study of effect of variation of pH, it was found that as pH of the reaction mixture was raised, the rate of adsorption also increases. The rate of adsorption of MB was found increased with increase in pH [63].

The formation of surface precursor complex, one of kinetic rate-limiting steps in heterogeneous oxidative degradation of organic pollutants, is closely related to the nature of surface charge. The amount of surface charge on the γ−MnOOH is deter-mined by protonation or deprotonation process, depending on suspension pH. In the present study, pH at zero point of charge (pH_{zpc}) of the γ−MnOOH was determined to be 9.8 using a simplified method [117]. Theoretically, at pH higher than 9.8, the surface is negatively charged due to deprotonation and negative surface charge increases with increasing suspension pH, which is conducive to the formation of surface precursor complex. Although low pH impeded the formation of surface precursor complexes, high H^+ concentration, how-ever, could improve reducing potential of the system according to the Nernst Equation. An increase in suspension pH would decrease oxidizing power of the system. On the other hand, the increase in formation of surface precursor complex due to pH increase could compensate for the reduction in oxidizing power of the system to some extent. One may conclude that suspension pH exerted two double-edged effects on MB decolorization [202].

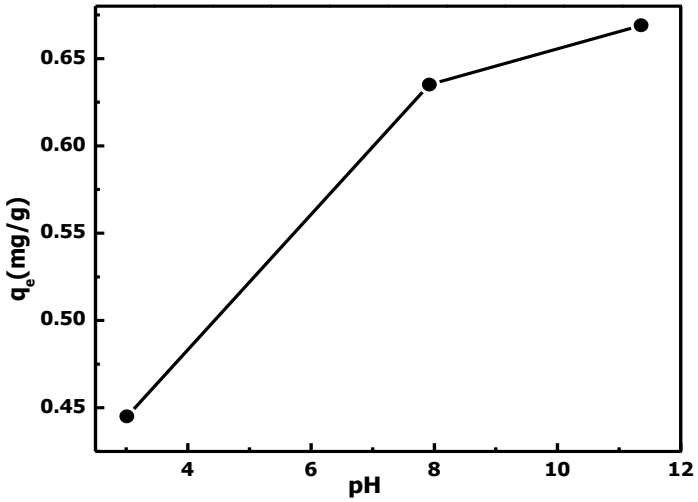

Fig.3.55. Effect of initial solution pH for MB decolorization by γ–MnOOH nps.

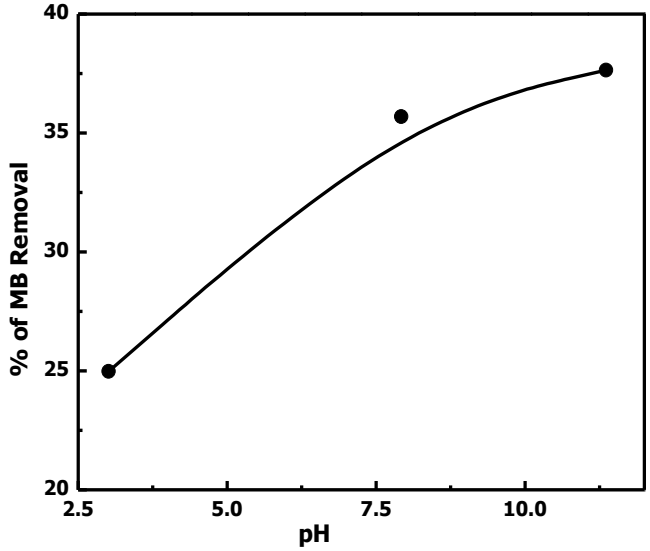

Fig. 3.56. Effect of pH for % decolorization for MB by γ–MnOOH nps.

3.7.2. Effect of pH for OG decolorization by γ–MnOOH nps

Table 3.18. Data for the influence of pH for OG decolorization by γ–MnOOH nps

Amount of γ–MnOOH nps: 0.005g Volume of the solution: 10 mL

Molar adsorption co-efficient: 16,168 L $mol^{-1}cm^{-1}$ Temperature: 28°C

Shaking time: 120 min

Initial conc.×10^5 ($molL^{-1}$)	pH	Absorbance at 477 nm	Equilibrium conc.×10^6 q_e $molL^{-1}$	Adsorbed conc.×10^6 q_m $molL^{-1}$	Amount adsorbed q_e (mg/g)	% of OG Removal
1.0	1.95	0.143	8.844	1.155	1.045	11.55
	5.95	0.284	17.565	7.565	6.845	75.65
	8.42	0.180	0.111	1.133	1.025	11.33
	10.02	0.175	0.108	0.824	0.745	8.24

To study the influence of solution pH for MB decolorization by γ–MnOOH nps at equilibrium conditions, experiments were carried out using various initial pHs varying from 1.95 to 10.02. As shown in **Fig. 3.57**, the amount of adsorption of solute increased as the pH was decreasing. When the pH was changed from 5.95 to 10.02, the adsorption decreased from 6.845 mg/g to 0.745 mg/g. Higher adsorptions at lower pH values could be well explained by protonation properties of the adsorbent. At low pH, *i.e.*, higher hydrogen ion concentration, the negative charges at the surface of internal pores are neutralized and some more new adsorption sites are developed as a result the surface provides a positive charge for anionic OG dye to get adsorbed. A similar type of behavior is also reported for the adsorption of the dye at different adsorbents [73].

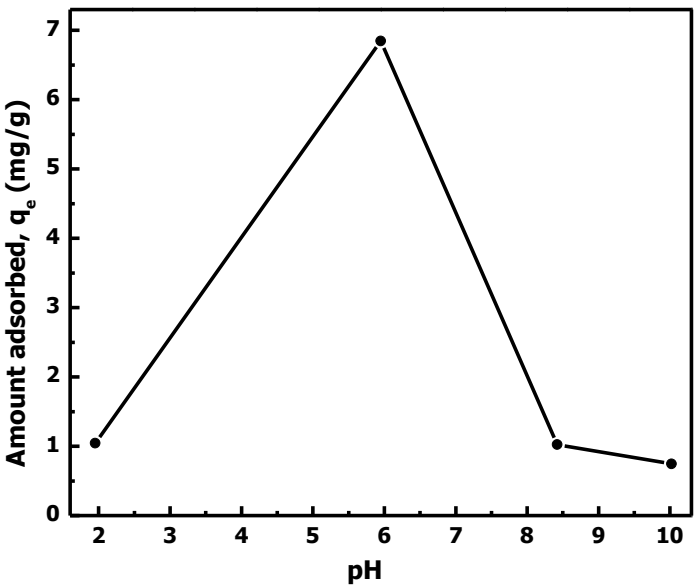

Fig.3.57. Effect of initial solution pH for the decolorization of OG by γ–MnOOH nps.

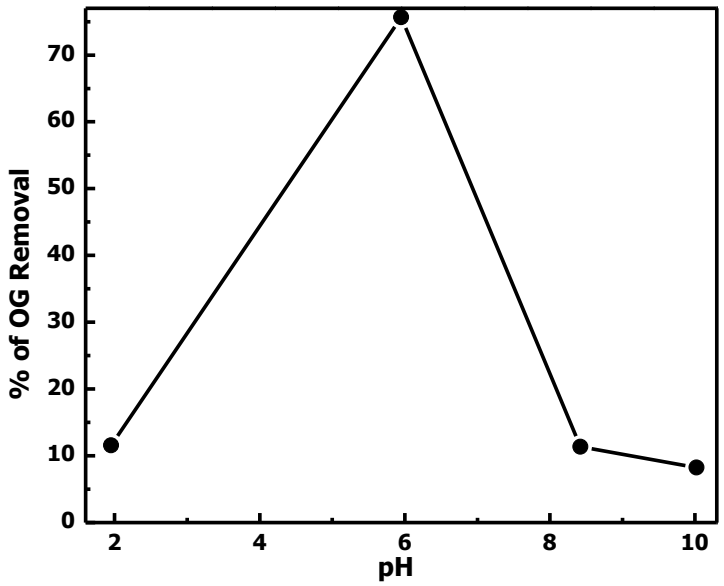

Fig. 3.58: Effect of pH for % decolorization for OG by γ–MnOOH nps.

3.7.3. Effect of amount of MnOOH nps for MB decolorization

Table 3.19. Data for the effect of amount of γ–MnOOH nps on MB decolorization

Volume of the solution: 10 mL Time: 180 min

Temperature: 28°C pH: 11.36

Initial conc.×10^5 q_0(molL^{-1})	Amount of dose (g)	Abs.	Equilibrium conc.×10^6 q_m(molL^{-1})	Adsorbed conc.×10^6 (q_0-q_m) (molL^{-1})	Amount Adsorbed q_e (mg/g)	% of MB removal
1.0	0.01	0.453	5.849	4.151	1.478	41.51
	0.02	0.488	6.301	3.699	0.658	36.99
	0.03	0.390	5.035	4.965	0.589	49.65
	0.05	0.306	3.951	6.049	0.431	60.49

The adsorbent dose is an important parameter in adsorption studies because it determines the capacity of adsorbent for a given initial concentration of dye solution. The dependence of MB adsorption on adsorbent dose with varying

amounts of γ–MnOOH nps has been examined and the detail results are presented in **Table 3.19**. It was found that MB removal by adsorbents depends strongly on the adsorbent dose, indicating that adsorption is dependent on the availability of the bonding sites [203]. When the adsorbent dose of adsorbents was increased from 0.01 to 0.05 g/10mL the MB binding capacity was increased dramatically. The capacity was further increased, but the magnitude of the increase is proportionally less significant with each successive increase. It is postulated that at low adsorbent doses, all types of sites are entirely exposed for adsorption, and the surface may become saturated faster; whereas at higher adsorbent dosages the availability of higher energy sites may decrease [204]. However, when increase the amount of dose percent of removal of MB increased (**Fig.3.59)** which indicated optimization of adsorbent dose was necessary before adsorption because of effective use of synthesized particles.

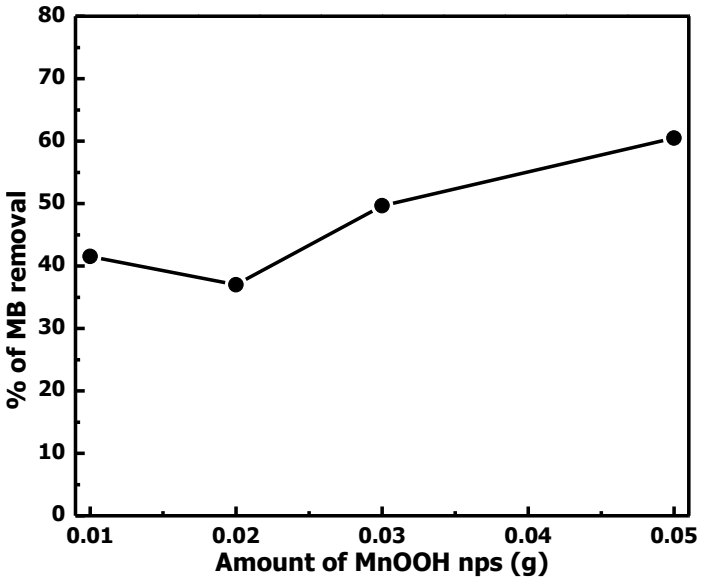

Fig.3.59: Effect of γ–MnOOH dose on % decolorization of MB.

3.8. Comparative kinetics for MB decolorization by Mn-oxide nps

MnO_2, Mn_3O_4 and γ–MnOOH nps have been synthesized in the present study. One important application of these substances is their use as decolorizer.

To observe the decolorization process of these substances, MB was used as adsorbate at different periods using previously described system.

3.8.1. Decolorization of MB by MnO_2, Mn_3O_4 and γ−MnOOH nps

Amount of Mn-oxide: 0.005 g Volume of the solution: 10 mL

λ_{max} for MB solution: 664 nm Temperature: 27.8°C

Molar absorption coefficient=77,449 L $mol^{-1}cm^{-1}$ Reference: Water

Initial concentration of MB, $C_0=1.0\times10^5$ ($molL^{-1}$) pH = 11.36.

Table 3.20(a): Data for decolorization of MB by MnO_2 at different time interval

Time (min)	Absorbance at equilibrium	Equilibrium conc. $\times10^6$ C_t ($molL^{-1}$)	Adsorbed conc.$\times10^6$ q_m($molL^{-1}$)	Amount adsorbed q_t (mg/g)
0	0.463	0.0	0.0	0.0
15	0.327	4.22	5.778	4.113
30	0.298	3.85	6.152	4.379
45	0.333	4.29	5.710	4.057
60	0.301	3.89	6.110	4.349
90	0.285	3.68	6.320	4.498
120	0.311	4.02	5.984	4.260

Table 3.20(b): Data for decolorization of MB by Mn_3O_4 at different time interval

Time (min)	Absorbance at equilibrium	Equilibrium conc. $\times10^6$ C_t ($molL^{-1}$)	Adsorbed conc.$\times10^6$ q_m($molL^{-1}$)	Amount adsorbed q_t (mg/g)
0	0.463	0.0	0.0	0.0
15	0.339	4.377	5.623	4.002
30	0.357	4.609	5.391	3.837
45	0.355	4.584	5.416	3.855
60	0.360	4.648	5.352	3.809
90	0.339	4.377	5.623	4.002
120	0.334	4.313	5.687	4.048

Table 3.20(c): Data for decolorization of MB by γ−MnOOH nps at different time interval

Time (min)	Absorbance at equilibrium	Equilibrium conc. $\times 10^6$ C_t ($molL^{-1}$)	Adsorbed conc.$\times 10^6$ q_m($molL^{-1}$)	Amount adsorbed q_t (mg/g)
0	0.463	0.0	0.0	0.0
15	0.330	4.261	5.739	4.085
30	0.354	4.571	5.429	3.864
45	0.338	4.364	5.636	4.011
60	0.345	4.454	5.545	3.947
90	0.360	4.648	5.352	3.809
120	0.371	4.790	5.230	3.708

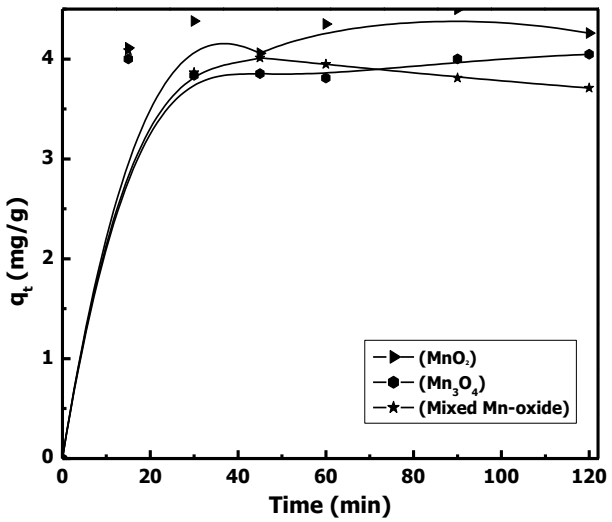

Fig.3.60. Amount of MB decolorized by MnO_2, Mn_3O_4 and γ−MnOOH nps vs. time. (T = 300.8 K, pH_i = 11.36, adsorbent dosage = 0.005g, $[MB]_i = 1.0\times10^{-5}$ mol L^{-1} and V= 0.01L).

3.8.2. Determination of monolayer capacity for decolorization of MB by MnO_2, Mn_3O_4 and γ−MnOOH nps

Amount of Mn-oxide: 0.005 g Volume of the solution: 10 mL

Temperature: 27.8°C pH = 11.36 shaking time: 120 min

Molar absorption coefficient =77,449 L mol^{-1} cm^{-1}

Table 3.21(a): Data for the decolorization of MB by MnO_2 nps at different initial concentration of MB solution

Initial conc.×10^6 ($molL^{-1}$)	Absorbance at equilibrium	Equilibrium conc. (mg/L)	Adsorbed conc.×10^6 ($molL^{-1}$)	Amount adsorbed q_e (mg/g)	C_e/ q_e (g/L)
5.0	0.075	0.344	4.032	2.869	0.119
8.0	0.149	0.685	6.076	4.325	0.158
10.0	0.188	0.864	7.573	5.390	0.160
15.0	0.313	1.438	10.958	7.800	0.184
20.0	0.401	1.842	20.000	10.550	0.176
25.0	0.563	2.587	17.731	12.620	0.204

Table 3.21(b): Data for decolorization of MB by Mn_3O_4 at different initial concentration of MB solution

Initial conc.×10^6 ($molL^{-1}$)	Absorbance at equilibrium	Equilibrium conc. C_e(mgL^{-1})	Adsorbed conc.×10^6 ($molL^{-1}$)	Amount adsorbed q_e (mg/g)	C_e/q_e (g/L)
5.0	0.127	0.584	3.360	2.392	0.244
8.0	0.177	0.813	5.715	4.068	0.120
10.0	0.22	1.011	7.159	5.096	0.199
15.0	0.278	1.277	11.411	8.122	0.157
20.0	0.452	2.077	14.164	10.082	0.206
25.0	0.592	2.720	17.356	12.354	0.220

Table 3.21 (c): Data for decolorization of MB onto γ−MnOOH nps at different initial MB concentration

Initial conc.×10^6 C_0($molL^{-1}$)	Absorbance at equilibrium	Equilibrium conc. C_e (mg/L)	Adsorbed conc.×10^6 q_m($molL^{-1}$)	Amount adsorbed q_e (mg/g)	C_e/q_e (g/L)
5.0	0.188	0.864	2.573	1.831	0.472
8.0	0.193	0.887	5.508	3.921	0.226
10.0	0.218	1.001	7.185	5.114	0.196
15.0	0.351	1.612	10.468	7.451	0.216
20.0	0.463	2.128	14.021	9.980	0.213
25.0	0.634	2.913	16.813	11.967	0.243

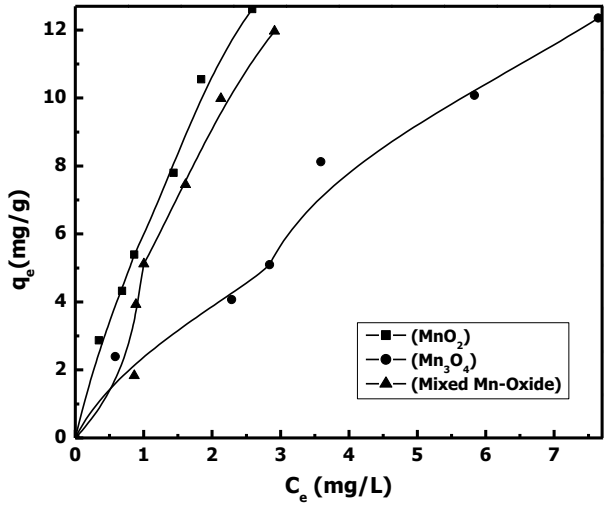

Fig.3.61. Langmuir isotherm for decolorization of MB by MnO_2, Mn_3O_4 and γ–MnOOH nps. (T = 300.8 K, pH_i = 11.36, adsorbent dosage = 0.005g, $[MB]_i$ = (5.0-25.0)×10^{-6} mol L^{-1} and V= 0.01L).

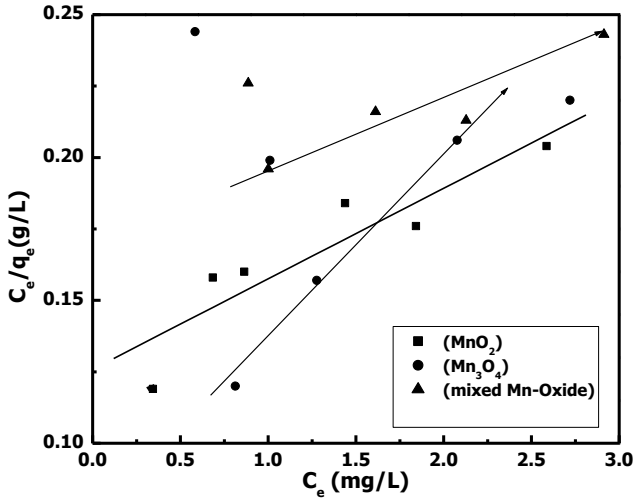

Fig.3.62. Linear plots for decolorization of MB by MnO_2, Mn_3O_4 and γ–MnOOH nps.

Comparison of the specific surface area of the substrates

Table 3.22: Comparison of surface area among MnO_2, Mn_3O_4 and γ–MnOOH nps (Cross sectional areas of MB (AMB) are 130 A^{02} and 178 A^{02} respectively)

Mn-oxides	Monolayer capacity, q_m	Specific surface area (m^2/g)	Adsorption coefficient K_L	R^2	Separation factor R_L

	(mg/g)		(L/mg)		
MnO_2	31.575	71.855 98.366	0.252	0.91	0.99
Mn_3O_4	23.078	50.774 69.521	0.137	0.81	0.99
γ−MnOOH	75.585	166.293 227.695	0.0674	0.65	0.99

From the above Table, it is seen that γ−MnOOH nps has higher SSA than others.

3.9. Effect of concentration and contact time for decolorization of MB by MnO_2

Amount of MnO_2: 0.005 g Volume of the solution: 10 mL

λ_{max} for MB solution: 664 nm Temperature: 27.8°C

Molar absorption coefficient=77,449 L $mol^{-1}cm^{-1}$ pH = 11.36

Table 3.23(a): Data for the decolorization of MB by MnO_2 at different time interval

Initial conc.×10^5 C_0($molL^{-1}$)	Time (min)	Absorbance at equilibrium	Equilibrium conc. ×10^6 C_t ($molL^{-1}$)	Adsorbed conc.×10^6 q_m($molL^{-1}$)	Amount adsorbed q_t (mg/g)
1.0	0	0.463	0.0	0.0	0.0
	15	0.327	4.22	5.778	4.113
	30	0.298	3.85	6.152	4.379
	45	0.333	4.29	5.710	4.057
	60	0.301	3.89	6.110	4.349
	90	0.285	3.68	6.320	4.498
	120	0.311	4.02	5.984	4.260

Table 3.23(b): Data for the decolorization of MB by MnO_2 at different time interval

Initial conc.×10^5 C_0($molL^{-1}$)	Time (min)	Absorbance at equilibrium	Equilibrium conc.×10^6 C_t ($molL^{-1}$)	Adsorbed conc.×10^6 q_m($molL^{-1}$)	Amount adsorbed q_t (mg/g)
0.5	0	0.463	0.0	0.0	0.0
	15	0.122	1.575	3.424	2.438

	30	0.152	1.963	3.037	2.162
	45	0.152	1.963	3.037	2.162
	60	0.164	2.118	2.882	2.052
	90	0.161	2.078	2.921	2.079
	120	0.157	2.027	2.972	2.116

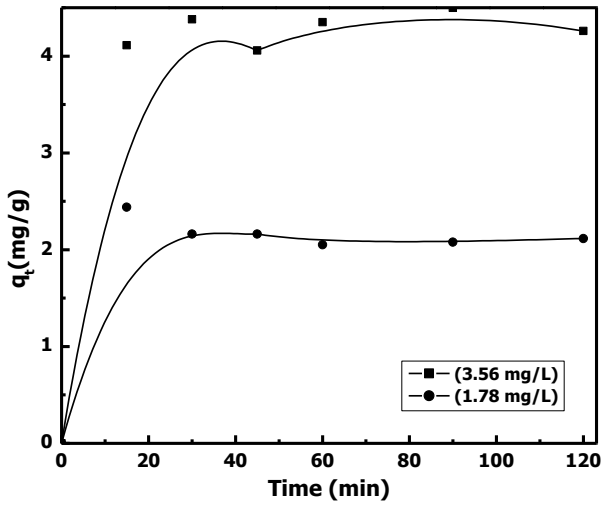

Fig.3.63. Effect of contact time and concentration for decolorization of MB by MnO_2 (T = 301 K, pH_i = 11.36, MnO_2 dosage = 0.005g, $[MB]_i$ = (1.78-3.56) mg L^{-1} and V= 0.01L).

3.10. Antibacterial activity of MnO_2, Mn_3O_4 and γ−MnOOH nps

Antibacterial activity of MnO_2, Mn_3O_4 and γ−MnOOH nps (10mg/10mL) against various pathogenic organisms was tested. The results are presented in **Table 3.30 and Fig. 3.64**. The bacteria tested are *V. Cholerae* causing cholera, *E. Coli* causing diarrhea and *S. Aureous*. In order to assess the antibacterial activity, zone diameter of inhibition observed by both the Mn-oxide and the control tetracycline antibiotic were measured. It can be seen from the result given in **Table 3.24.** Whatever the mechanism might be, this result implied that Mn-oxide nps could not kill some bacteria and interacts with them relatively strongly.

Table 3.24: Antibacterial activity of MnO_2, Mn_3O_4 and γ−MnOOH nps suspension (10mg/10mL) against different pathogenic organisms.

Bacteria	Zone diameter of inhibition (mm)			
	MnO_2	Mn_3O_4	γ−MnOOH	Control (Tetracycline)
Vibrio cholerae	R*0.0	R*0.0	R*0.0	S*17
S. aureous	R*0.0	R*0.0	R*0.0	S*13
Escherichia coli	R*0.0	R*0.0	R*0.0	S*6

Where, S* and R* stand for sensitive and resistant, respectively.

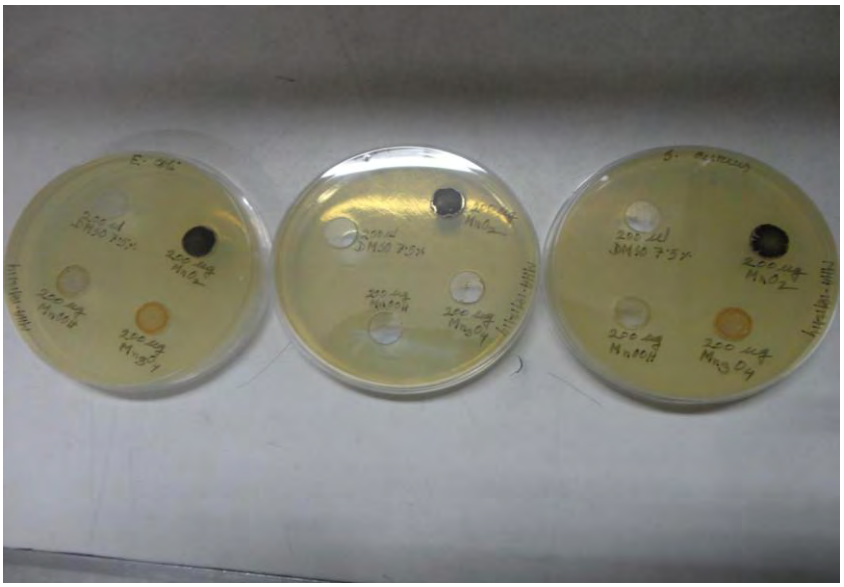

Fig.3.64: Antibacterial activity of MnO_2, Mn_3O_4 and γ−MnOOH nps suspension in 7.5% (v/v) DMSO against different pathogenic organisms.

CONCLUSION

Conclusion

Mn-oxide nanomaterials have become very attractive because of their wide potential applications in various technologically important fields. The proposed method of obtaining MnO_2, Mn_3O_4 and manganite was adequate, based on its simplicity and reproducibility.

The chemically and structurally well defined particles lead to a better understanding of structural properties which help in designing their potential applications.

The FT-IR spectra showed the characteristics signals of MnO_2, Mn_3O_4 and γ−MnOOH nps and confirmed the presence of the components in each substrate. The obtained average crystallite size of Mn-oxides indicated that the as-synthesized Mn-oxides were in the nanophase. The particles were observed to be highly crystalline. The SEM images showed aggregating the particulate in the substrate. EDX indicated the presence of Mn and O only and no other impurity. DLS indicated the samples were polydisperse aggregated nanoparticles. TG-DTA revealed that samples were thermally stable. pH_{PZC} were 8.8, 8.75 and 9.8 respectively for MnO_2, Mn_3O_4 and γ−MnOOH MnOOH nps.

The as-synthesized MnO_2, Mn_3O_4 and γ−MnOOH nps gave attractive surface area and hence should have a potential application as adsorbent. Consequently, decolorization of MB by γ−MnOOH nps was found to be significantly higher than that of OG. γ−MnOOH nps seems to be a specific excellent adsorbent for the removal of cationic MB dye from water. A detailed decolorization characteristic of the Mn-oxide was successfully demonstrated.

In this work, OG as a model azo dye in aqueous solution was successfully decolorized by Mn-oxides and it was found that OG decolorization followed the pseudo second-order kinetic model. The highest pH for MB and OG decolorization was 11.36 and 5.95 respectively. Kinetic studies were also performed to investigate the rate of adsorption process. Experimental data fitted well the pseudo-second-order kinetic model while the first order kinetic model was not

found valid for the whole range of adsorption process. Other than that, intra-particle diffusion was found to be prominent at a certain stage of decolorization but it would not be the only limiting step that controlled the adsorption dynamic.

Batch equilibrium data for MB and OG decolorization also found to have a good agreement with Freundlich isotherm model. The analysis of isotherm showed that decolorization was favorable by Mn-oxide nps. Temkin model was applicable for MB decolorization. Adsorbent doses were necessary to optimize for effective use of adsorbent.

Our as-synthesized nps did not show potential antibacterial activity towards both gram-positive and gram-negative bacteria.

REFERENCES

REFERENCES

1. B. J. Clapsaddle, D. W. Sprehn, A. E. Gash, Joe H. Satcher Jr. and Randall L. Simpson, 'A versatile sol-gel synthesis route to metal-silicon mixed oxide nanocomposites that contain metal oxides as the major phase", *Non-crystalline Solids*, **2004,** 350, 173-181.
2. Nakamura, M. Saitoh, H. Maejima, M. Yamagiwa and S. Kaneko, *Fresenius Z Anal Chem.,* **1989**, 335**,** 573 – 575.
3. C. Burda, X. B. Chen, R. Narayanan and M. A. El-Sayed, "Chemistry and properties of nanocrystals of different shapes," *Chem. Rev.*, **2005**, 105, 1025–1102.
4. J. Cao, Q. H. Mao, L. Shi and Y. T. Qian, "Fabrication of γ-MnO_2/α-MnO_2/ hollow core/shell structures and their application to water treatment," *J. Mater. Chem.*, **2011**, 21, 16210–16215.
5. D. Yan, S. Cheng and R. F. Zhuo, "Nanoparticles and 3D sponge-like porous networks of manganese oxides and their microwave absorption properties," *Nanotechnol.*, **2009**, 20, 10.
6. Y. W. Tan, L. R. Meng, Q. Peng and Y.D. Li, "One-dimensional single-crystalline Mn_3O_4 nanostructures with tunable length and magnetic properties of Mn_3O_4 nanowires," *Chem. Comm.*, **2011**, 47, 1172–1174.
7. X. Zhang, Z. Xing and Y. Yu, "Synthesis of Mn_3O_4 nanowires and their transformation to $LiMn_2O_4$ polyhedrons, application of $LiMn_2O_4$ as a cathode in a lithium-ion battery," *Cryst Eng-Comm.*, **2012**, 14, 1485–1489.
8. R. Ma, Y. Bando, L. Zhang and T. Sasaki, "Layered MnO_2 nanobelts: hydrothermal synthesis and electrochemical measurement," *Adv. Mater.*, **2004**, 16, 918–922.
9. F.Y. Cheng, J. Z. Zhao and W. Song, "Facile controlled synthesis of MnO_2 nanostructures of novel shapes and their application in batteries," *Inorg. Chem.*, **2006**, 45, 2038–2044.
10. C. Noguera, '*Physics and Chemistry at Oxide Surfaces*', *Cambridge Univ. Press: Cambridge,* UK, **1996**.

11. H. H. Kung, `*Transition Metal Oxides: Surface Chemistry and Catalysis*', Elsevier: Amsterdam, **1989**.
12. V. E. Henrich and P. A. Cox, `*The Surface Chemistry of Metal Oxides*', Cambridge University Press: Cambridge, UK, **1994.**
13. A. F. Wells, `*Structural Inorganic Chemistry', 6th ed*; Oxford University Press: New York, **1987**.
14. L. E. Achurra, J. P. Lacassie, J.P. Le Roux, C. Marquardt, M. Belmar, J. Ruiz-del-solar and S. E. Ishman, *Sedimentary Geology*, **2009**, 217, 128-139.
15. J. Y. Luo, H. M. Xiong and Y. Y. Xia, *J. Phys. Chem. C.,* **2008,** 112, 12051-12057.
16. M. Nitta, *Appl. Catal.* **1984,** 9, 151-176.
17. J. Cao, Y. Zhu, L. Shi, K. Bao, S. Liu and Y. Qian, *Eur. J. Inorg. Chem.,* **2010,** 1172.
18. E. R. Stobbe, B. A. de Boer and J. W. Geus, *Catal. Today,* **1999,** 47, 161-167.
19. E. F. Pratt and J. F. Van de Castle, *J. Org. Chem.* **1961,** 26, 2973-2975.
20. F. Y. Cheng, J. Z. Zhao and W. Song, "Facile controlled synthesis of MnO_2 nanostructures of novel shapes and their application in batteries," *Inorg. Chem.,* **2006,** 45, 2038–2044.
21. F. Y. Cheng, J. A. Shen, B. Peng, Y. D. Pan, Z. L. Tao and J. Chen, "Rapid room-temperature synthesis of nanocrystalline spinels as oxygen reduction and evolution electrocatalysts," *Nature Chem.*, **2011**, 3, 79–84.
22. B. Sun, Z. X. Chen, H. S. Kim, H. Ahn and G. X. Wang, "MnO/C core-shell nanorods as high capacity anode materials for lithium-ion batteries," *J. Power Sources*, **2011**,196, 3346–3349.
23. Y. Chen, Y. Hong, Y. Ma and J. Li, "Synthesis and formation mechanism of urchin-like nano/micro-hybrid α-MnO_2," *J. Alloys and Compounds*, **2010,** 490, 331–335.
24. X. Wang and Y. Li, "Selected-control hydrothermal synthesis of α- and β-MnO_2 single crystal nanowires," *J. Am. Chem. Soc.*, **2002,** 124, 2880–2881.
25. Greenwood, N. Norman, Earnshaw and Alan, *Chemistry of the Elements* (2nd ed.), Butterworth-Heinemann, **1997**.
26. E. R. Stobhe, A. D. de Boerand and J. W. Geus, 'The reduction and oxidation behaviour of manganese oxides' *Catalysis Today,* **1999**, 47, 161–167.

27. G. D. Moggridge, T. Rayment and R. M. Lambert, 'An in situ XRD investigation of singly and doubly promoted Mn-oxide methane coupling catalysts', *J. Catal.,* **1992**, 134, 242–252.
28. T. Yamashita and A. Vannice, 'NO Decomposition over Mn_2O_3 and Mn_3O_4' *J. Catal.*, **1996**, 163, 158–168.
29. W. M. Wang, Y. N. Yang and J.Y. Zhang, 'Selective reduction of nitrobenzene to nitrosobenzene over different kinds of Mn_3O_4 catalysts', *Applied Catalysis A,* **1995**, 133, 81–93.
30. M. Baldi, E. Finocchio, F. Milella and G. Busca, 'Catalytic combustion of C_3 hydrocarbons and oxygenates over Mn_3O_4', *Applied Catal. B*, **1998**, 16, 43–51.
31. B. Boucher, R. Buhl and M. Perrin, 'Magnetic Structure of Mn_3O_4 by Neutron Diffraction', *J. Appl. Phys.,* **1971**, 42, 1615.
32. I. K. Gopalakrishnan, N. Bagkar, R. Ganguly and S. K. Kulshreshtha, 'Synthesis of superparamagnetic Mn_3O_4 nanocrystallites by ultrasonic irradiation,' *J. Crystal Growth*, **2005,** 280, 436-441.
33. A. Withop and R. E. Travagli, 'Method of making manganese-zinc ferrite' *U.S Patent number: 4093688,* **1978**.
34. Horst Krampitz and Gerhard Wohner, 'Process for preparing lithium manganese oxides', *U.S Patent number: 6706443*, **2004.**
35. S. Thiagarajan, T. Hsuan and S. M. Chen, *Int. J. Electro. Sci.* **2011,** 6, 2235.
36. C. J. Lind, 'Hausmanite conversion to manganite in dilute oxalate solution', *Enviorn, Sci. Technol,* **1988**, 22, 62-70.
37. G. Xi, Y. Peng, Y. Zhu, L. Xu, W. zhang, W. Yu and Y. Qian, *Mater. Res. Bull.,* **2004**, 39, 1641-1648.
38. J. Li, Y. J. Wang, B. S. Zou, X. C. Wu, J. G. Lin, L. Guo and Q. S. Li, *Appl. Phys. Lett.* **1997**, 70, 3047.
39. D. G. Shchukin, D. V. Sviridov and A. I. Kulak, *Sens. Actuators B, Chem.* **2001**, 76, 556.
40. R. B. Anderson and P.T. Dawson, *Experimental Methods in Catalytic Research*, Academic Press, New York, **1976**, 2, 215-219.

41. D. S. King and R. M. Nix, "Thermal Stability and Reducibility of ZnO and Cu/ZnO Catalysts", *J., Catal.,* **1996**, 76, 160.
42. O.Toshio and M. Makato, 'Oxide catalyst in Solid state Chemistry', **1987**, 2889.
43. K. David, Ward and I. K. Edmond, "Preparing Catalytic Materials by the Sol-Gel Method", *Ind. Eng. Chem. Res.,* **1995**, 34, 421-432.
44. M. S. Azam, "Synthesis of Catalytically Important Manganese Oxide Nano-particles and Their Dispersion into a Polymeric Matrix" Department of Chemistry, BUET, Dhaka, Bangladesh, **2008**, 4.
45. M. A. Agam and Q. Guo. "Electron Beam Modification of Polymer Nanospheres". *J. Nanosci. Nanotechnol.,* **2007,** 7, 3615–3619.
46. J. H. Choy, E. S. Jang, J. H. Won, J.H. Chung, D. J. Jang and Y.W. Kim, "Hydrothermal route to ZnO nanocoral reefs and nanofibers", *Appl. Phys. Lett.* **2004**, 84, 287.
47. Y. Sun and Y. Xia. "Shape-controlled synthesis of gold and silver nanoparticles". *Science,* **2002***,* 298, 21769.
48. A. M. Pollard, M. S. Spencer, Thomas, R. G Williams, P. A. Holt and J. Jennings, *Appl. Catal. A,* **1992**, 85, 1–11.
49. S.Pavasupree, S. Ngamsinlapasathian, S. Pivsa-art, S. Suzuki and S. Yoshikawa, *Proceedings* of *The Joint Int'l Conf. on "Sustainable Energy and Environment (SEE),* **2004**, 58-62.
50. A. Tarafdar and P. Pramanik, *Microporous and mesoporous materials*, **2006**, 91, 221-224.
51. Biswas, K. Gupta and U. C. Ghosh, 'Adsorption of fluoride by hydrous iron(III)–tin(IV) bimetal mixed oxide from the aqueous solutions', *Chemical Engg. J.,* In Press, **2008.**
52. Nora, D. Nidola, V. Spaziante, A. Placido, M. Giuseppe, *US patent no. 4267025*, **1981.**
53. T. Koichi and H. Akifusa, *Denki Kagaku oyobi Kogyo Butsuri Kagaku*, **2001**, 69, 692-698.
54. Taylor et al., *Chem. Commun.*, **1999**, 1373-1374.
55. T. Ishihara, K. Kometani, M. Hashida, and Y.Takita, *J. Electrochem. Soc.*, **1991**, 138, 173-176.

56. E. Gill, K. Arshak, A. Arshak and O. Korostynska, *Microsystem Technologies archive* **2008,** 14, 499-507.
57. S.D. Rodney and O.K. Edmond, Method for making a rutile mixed metal oxide pigment, *United States Patent 5759256*, **1998**.
58. E. N. Balko and P. H. Nguyen, *APP. Electrochem.,* **1991**, 21, 678-682.
59. M. Grätzel, Photo electrochemical cells, *Nature*, **2001**, 414, 338-344.
60. F.Zhang, S. Yang, H. Chen and X. Yu, 'Preparation of discrete nanosize ceria powder', *Ceramics Int'l*, **2004**, 30, 997-1002.
61. C. Bouvy and B. Su, *J. Materials Sci.Technol.,* **2008**, 24, 495-511.
62. S. Sanjay, A. Vaghel, D. Ashok, A.Jethv, B. Bhavesh, A. Meth, P. Sunil, Dave, S. Adimurthy and G. Ramachandraiah, "Laboratory Studies of Electrochemical Treatment of Industrial Azo Dye Effluent", *Environ. Sci. Technol.,* **2005**, 39, 2848.
63. D. Ghosh, K. G. Bhattacharyya, 'Adsorption of methylene blue on kaolinite', *Appl. Clay Sci*. **2002**, 20, 295–300.
64. M. Wainwright, D. A. Phoenix, L. Rice, S. M. Burrow and J. Waring, "Increased cytotoxicity and phototoxicity in the methylene blue series via chromophore methylation," *J. Photochem. Photobiol. B*, **1997**, 40, 233-239.
65. T. Zhang, T. Oyama, S. Horikoshi, H. Hidaka, J. Zhao and N. Serpone, "Photocatalyzed N-demethylation and degradation of methylene blue in titania dispersions exposed to concentrated sunlight," *Solar Energy Materials and Solar Cells*, **2002**, 73 287–303.
66. N. Matsuda, J. Zheng, D. K. Qing, A. Takatsu and K. Kato, "In situ absorption spectra and adsorbed species of methylene blue on glass/water interfaces by slab optical waveguide spectroscopy," *Applied Spectroscopy*, **2003**, 57,100–103.
67. A-N. Chowdhury, M. S. Azam, M. Aktaruzzaman and A. Rahim, "Oxidative and antibacterial activity of Mn_3O_4," *J. Hazard. Mater.*, **2009**, 172, 1229–1235.
68. J. Tang, Z. Zou, J. Yin and J. Ye, "Photocatalytic degradation of methylene blue on $CaIn_2O_4$ under visible light irradiation," *Chemical Physics Letters*, **2003**, 382, 175–179.
69. Heinrich Caro, "Improvement in the production of dye-stuffs from methyl-aniline," *U.S. Patent no. 204*, **1878**, 796.

70. L. Michaelis; M. P. Schubert and S. Granick. "Semiquinone Radicals of the Thiazines". *J. Am. Chem. Soc.* **1940**, 62, 204–211.
71. J. Cenens and R. A. Schoonheydt. "Visible Spectroscopy of methylene on Hectorite, Laponite B and Barasym in aqueous suspension". *Clay and Clay Minerals,* **1988,** 36, 214–224.
72. M. A. Aziz, "*A Text Book of Water Supply Engineering*", Hafij book centre*, Dhaka,* **1994**, 178-182.
73. N. Mohan, N. Balasubramanian and C. A. Basha, "Electrochemical Oxidation of Textile Wastewater and Its Reuse", *J. of Hazourd. Mater.,* **2007**, 147*,* 644.
74. C. Cameselle, M. Pazos, M. A. Sanroman, "Selection of an Electrolyte to Enhance the Electrochemical Decolorization of Indigo Optimization and Scale-up", *Chemosphere.* **2005**, 60, 1080.
75. N. Caner, I. Kiran, S. Ilhan and C. F. Iscen,"Isotherm and Kinetic Studies of Burazol Blue ED Dye Biosorption by Dried Anaerobic Sludge", *J. Hazourd. Mater.,* **2009**, 165, 279.
76. W. Zhao, C. Chen, X. Li, J. Jhao, H. Hidaka, and N. Serpone, "Photodegradation of Sulforhodamine-B Dye in Platinized Titania Dispersions under Visible Light Irradiation: Influence of Platinum as a Functional Co-catalyst", *J. Phys. Chem. B.,* **2002**, 106*,* 5022.
77. X. Tao, J. Su and J. F. Chen, "Photooxidative Degradation of Dye Pollutants Accumulated in Self-Assembled Natural Polyelectrolyte Microshells under Visible Radiation" *J. Chem. Eur.,* **2006**, 12, 4164.
78. F. Akbal, "Photocatalytic Degradation of Organic Dyes in the Presence of Titanium Dioxide under UV and Solar Light: Effect of Operational Parameters", *Env. Progress*, **2005**, 24*,* 317-322.
79. S. Ranghu and B. C. Ahmed, "Dye Destruction and Simultaneous Generation of Sodium Hydroxide Using a Divided Electrochemical Reactor" *Ind. Eng. Chem. Res.*, **2008**, 47, 5277.
80. S. Wellington, S. Pereira, S. Renato and S. Freire, "Azo Dye Degradation by Recycled Waste Zero-Valent Iron Powder" *J. Braz. Chem. Soc*. **2006**, 17*,* 832.

81. C. C. Chen, A. J. Chaudhary and S. M. Grimes, "Photodegradation of Acid Blue 29 and Ethyl Violet in the Presence/Absence of Sodium Hydroxide and Aluminium Ions" *Env. Info. Archives.*, **2005**, 3, 111.
82. G. R. P. Malpass, D. W. Miwa, S. A. S. Machado and A. J. Motheo, "Decolourization of Real Textile Waste Using Electrochemical Techniques: Effect of Electrode Composition" *J. Hazard. Mater.,* **2008**, 156, 170.
83. Fu Y, Viraraghavan T., 'Fungal decolorization of dye wastewaters: a review', *Bioresour Technol.*, **2001**,79, 251-62.
84. N. Daneshvar, H. A. Sorkhabi and A.Tizpar, 'Decolorization of orange II by electro coagulation method', *Sep. Purifi. Technol.,* **2003**, 31,153– 162.
85. K. Kadirvelu, M. Kavipriya, C. Karthika, M. Radhika, N. Vennilamani and S. Pattabhi, "Utilization of Various Agricultural Wastes for Activated Carbon Preparation and Application for the Aqueous Solutions", *Bioresour. Technol.,* **2003**, 87, 129-132.
86. T. Robinson, G. McMullan, R. Marchant and P. Nigam, 'Remediation of dyes in textile effluent: a critical review on current treatment technologies with a proposed alternative', *Bioresour.Technol.***, 2001,** 77, 247–255.
87. L. Zhang, X. Zhou, X. Guo, X. Song, and X. Liu, "Investigation on the degradation of acid fuchsin induced oxidation by $MgFe_2O_4$ under microwave irradiation," *J. Molecular Cat. A*, **2011**, 335, 31–37.
88. S. A. Figueiredo, R. A. Boaventura and J. M. Loureiro, 'Color removal with natural adsorbents: modeling, simulation and experimental', *Sep. Purif. Technol.* **2000,** 20,129–141.
89. D. P. Barr and S. D. Aust, 'Mechanisms white rot fungi use to degrade pollutants', *Environ. Sci. Technol.*, **1994**, 28, 78A–87A.
90. F. C. Michel, C. A. Reddy and L. J. Forney, 'Microbial degradation and humification of the lawn care pesticide 2,4-dichlorophenoxy acetic acid during the composting of yard trimmings', *Appl. Env. Microbiol.*, **1995**, 61, 2566-2571.
91. J. M. Davis, R. C. Lohmann, F. M. Phillips, J. L. Wilson and D. W. Love, 'Architecture of the sierra ladrones formation, central New Mexico: Depositional controls on the permeability correlation structure', *Geol. Soc. Amer. Bull.*, **1993**, 105,998-1007.

92. P. Nigam, I. M. Bant, D. Singh and R. Marchant, 'Microbial process for the decolorization of textile eluent containing aza, diazo and reactive dyes', *Process Biochem*, **1996**, 435-442.

93. T. Ogawa and C. Yatome, 'Biodegradation of azo dyes in multi-stage rotating contactor immobilized by assimilating bacteria'. *Bull. Environ. Contam. Toxicol.*, **1990**, 44, 561-566.

94. Kumar *et al*., **1998**.

95. J. K. Polman, C. R. Breckenridge, 'Biomass-mediated binding and recovery of textile dyes from waste effluents' *Text. Chem. Color.*, **1996**, 28, 31-35.

96. D. Choi, K. S. Lee and G.Y. Suh, 'pulmonary tuberculosis presenting as acute respiratory failure: radiologic findings'. *J Comput Assist Tomogr,* **1999**, 23,107–113.

97. Mahmut Özacar and I. A. Sengil, *Colloids Surf. A: Physicochem. Eng. Aspects,* **2004**, 242, 105–113.

98. Malik, **2003.**

99. G. H. Findenegg, '*Fundamentals of Adsorption*, *Engineering Foundation*: New York, **1984**, 207-218.

100. J. T. Nolan, T. W. McKeehan and R. P. Danner, *J. Chem. Eng. Data,* **1981**, 26, 112.

101. P. W. Atkins, Physical Chemistry, Oxford University Press, sixth edition, **1998**, 857.

102. R. Barziv, A. Meller, T. Tlusty, E. Moses, J. Stavans and S. A. Safran, *Phys. Rev. Lett*. **1997**, 78, 154.

103. A. Kamyshny, D. Danino, S. Magdassi and Y. Talmon, *Langmuir,* **2002***,* 18, 3390.

104. A. Shukla, M.A. Kiselev, A. Hoell and R.H.H. Neubert, *Pramana-J Phys*. **2004**, 63, 291.

105. S. Chakraborty, B. Sahoo, I. Teraoka and R.A. Gross, *Carbohydrate Polymers* **2005**, 60, 475.

106. H. Xie, K.L. Gill-Sharp and P. O'Neal, *Nanomed. Nanotechnol. Biol. Med.* **2007**, 3, 89.

107. D. Marguev, *J. Phys. Chem*, **1998**, 102, 10778-10791.

108. W.P. Wuelfing, A. C. Templeton, J. F. Hicks and R. W. Murray, *Anal. Chem.* **1999,** 71, 4069.

109. A. W. Coats and J. P. Redfern, "Thermogravimetric Analysis: A Review". *Analyst* **1963**, 88, 906–924.

110. C. S. Marvel, "Synthesis of Thermally Stable Polymers". *Ft. Belvoir: Defense Technical Information Center,* **1972.**

111. H.K.D.H. Bhadeshia "Thermal analyses techniques. Differential thermal analysis". University of Cambridge, *Mat. Sci. Metallur.*, **2002.**

112. S. Ferrer, J. Borrás and F. J. Martín Gil "Thermal studies on sulphonamide derivative complexes". *Thermochim. Acta*, **1989**, 147, 321.

113. K. G. Berger, E. E. Akehurst "Some applications of differential thermal analysis to oils and fats". *Int'l J. Food Sci. Technol.*, **1966**, 1, 237–247.

114. V.S. Ramachandran, "Applications of differential thermal analysis in cement chemistry". *Chap. V, Chemical Publishing Co., Inc.,* New York, **1969**, 92.

115. W. Smykatz-Kloss "Application of differential thermal analysis in mineralogy". *J. Therm. Anal. Cal.*, **1982**, 23, 15-44.

116. W. Smykatz-Kloss, A. Heil, L. Kaeding and E. Roller "Thermal analysis in environmental studies", *Thermal analysis in Geosci.*, **1991.**

117. M. Schreier, "A Theoritical Study on CO_2 Solubility in Water as a function of pH", *J., Can. Goetech.*, **2006**, 12, 14-17.

118. R. Chang, Chemistry, McGraw-Hill Inc., fifth edition, Int'l edition, **1994,** 817-819.

119. V. B. R. Boppana and F. Jiao "Nanostructured MnO_2: An efficient and robust water oxidation catalyst", *Chem. Commun.*, **2011**, 47, 8973.

120. B. Babakhani and D. G. Ivey, "Anodic deposition of Mn-oxide electrodes with rod-like structures for application as electrochemical capacitors," *J. Power Sources*, **2010**, 195, 2110.

121. H. Chen and J. He, "Facile synthesis of mono disperses Mn-oxide nanostructures and their application in water treatment", *J. Phys. Chem.*, **2008**, 112, 17540.

122. S. C. Pang, S. F. Chin and C. Y. Ling, "Preparation and characterization of self-assembled manganese dioxide thin films," *J. Nanotechnol.,* **2011**, 2011, 7.

123. M. A. Islam and M. M. Rahman, "A kinetic study of the reaction of colloidal Mn-dioxide with perchloric acid in neutral aqueous solution," *J. Colloid Sci. Biotechnol.,* **2013**, 2, 70.

124. Deogratius Jaganyi, Mohammad Altaf and Isaac Wekesa, 'Synthesis and characterization of whisker-shaped MnO_2 nanostructure at room temperature, *'Appl Nanosci.* **2013**, 3, 329–333.

125. Xiujuan Chu and Hua Zhang, 'Catalytic Decomposition of Formaldehyde on Nanometer MnO_2 ', *Modern Applied Sci.,* **2009**, 3, 177-181.

126. Hyun-A Choi, Hyuk Jang, Hyein Hwang, Mincheol Choi, Dongwook Lim, Sang Eun Shim and Sung-Hyeon Baeck, 'Synthesis and Characterization of Different MnO_2 Morphologies for Lithium-Air Batteries', *Electron. Mater. Lett.,* **2014**, 10, 957-962.

127. C. Yuan, B. Gao, L. Su and X. Zhang *, J. Colloid Interface Sci.,* **2008,** 322, 545.

128. Y. Wang, A. Lu, H. Zhang, W. Li *, J. Phys. Chem. C,* **2011**, 115, 5413.

129. R. N. DeGuzman, Y. F. Shen and E. J. Neth, "Synthesis and characterization of Octahedral Molecular Sieves (OMS-2) having the hollandite structure," *Chem. Materials*, **1994**, 6, 815–821.

130. X. Wang and Y. Li, "Synthesis and formation mechanism of MnO_2 nanowires/nanorods," *Chemistry—A European J.*, **2003**, 9, 300–306.

131. J. Wu, H. Zhang and X. Ma, "Synthesis and characterization of single crystalline MnOOH and MnO_2 nanorods by means of the hydrothermal process assisted with CTAB," *Materials Letters*, **2006**, 60, 3895–3898.

132. Suh Cem Pang, Suk Fun Chin, and Chian Ye Ling, 'Controlled Synthesis of Manganese Dioxide Nanostructures via a Facile Hydrothermal Route', *Journal of Nanomaterials,* **2012**, 7, 2012.

133. Aye Aye Hlaing and Phyu Phyu Win' The synthesis of MnO_2 nanorods using hydrothermal homogeneous precipitation' *Adv. Nat. Sci.: Nanosci. Nanotechnol.* **2012**, 3, 3.

134. Danisa Tabassum and A-N. Chowdhury, 'Preparation and characterization of nanoparticle assisted conductive polyaniline' *M. Phil Thesis, BUET*, **2011**, 74-75.

135. Trans Hong Con, Phuong Thao, Trinh Xuan Dai and Dong Kim loan, 'Application of nano dimensional MnO_2 for high effective sorption of arsenic and fluoride in drinking water', *Environ. Sci.,* **2013** , 1, 69-77.

136. Z-Y. Tian , P. M. Kouotou , Naoufal Bahlawane and P. H. T. Ngamou, "Synthesis of the catalytically active Mn_3O_4 spinel and its thermal properties", *J. Phys. Chem. C*, **2013**, 117, 6218.

137. H-M. Luo, F-B. Zhang and P. Yang, "Preparation and electrochemical properties of CPAC/Mn_3O_4 nanocomposite electrode", *J. Mater. Sci: Mater Electron*. **2013**, 24, 601.

138. E. J. Grootendorst, Y. Verbeek and V. Ponec, "The role of the Mars and Van Krevelen mechanism in the selective oxidation of nitrosobenzene and the deoxygenation of nitrobenzene on oxidic catalysts", *J. catal.,* **1995**, 157, 706.

139. L.-X.Yang, Y.-J. Zhu, H.Tong, W.-W. Wang and G.-F. Cheng, *J. Solid State Chem.* **2006**, 179, 1225.

140. Z. W. Chen, J. K. L. Lai and C. H. Shek, *Scr. Mater.* **2006**, 55, 735.

141. Y. C. Zhang, T. Qiao and X.Y. Hu, *J. Solid State Chem.* **2004**, 177, 4093.

142. P. Gibot and L. Laffont, *J. Solid State Chem.* **2007**, 180, 695.

143. Z. H. Wang, D. Y. Geng, Y. J. Zhang and Z. D. Zhang *J. Cryst. Growth,* **2008,** 310, 4148.

144. A. Vázquez-Olmos, R. Redón, G. Rodríguez-Gattorno, M. E. Mata-Zamora, F. Morales-Leal, A. L. Fernández-Osorio and J. S. Saniger, *J. Colloid Inter. Sci.* **2005**, 291, 175.

145. T. Özkaya, A. Baykal, H. Kavas, Y. Köseoglu and M. S. Toprak, *Physica B,* **2008**, 403, 3760.

146. Y. Hu, J. Chen, X. Xue and T. Li, *Mater. Lett.* **2006**, 60, 383.

147. K. Usha and C. K. Mahadevan, 'Structure, Morphology and Electrical properties of Mn3O4 nanocrystals', *Archives of Physics Research*, **2011**, 2, 75-80.

148. Masoud Salavati-Niasari, Fatemeh Davar, Mehdi Mazaheri, 'Synthesis of Mn_3O_4 nanoparticles by thermal decomposition of a[bis(salicylidiminato) Mn(II)] complex' *Polyhedron,* **2008**, 27, 3467–3471.

149. Jr-I. Lai, V. P. Kurikka, M. Shafi, A. Ulman, N-L. Yang, M-H. Cui, T. Vogt and C. Estournes, "Mixed Fe-Mn oxide nanoparticles," *Prepr. Pap.- Am. Chem. Soc., Div, Fuel Chem.,* **2003**, 48, 729.

150. J. Zhou, X. Sheny and M. Jing, "Nanosized Ni-Mn oxides prepared by the citrate gel process and performances for electrochemical capacitors", *J. Mater. Sci. Technol.*, **2006,** 22, 803.

151. C. L. Shope, Ying Xie and C. H. Gammons, "The influence of hydrous Mn–Zn oxides on diel cycling of Zn in an alkaline stream draining abandoned mine lands", *App. Geochem.,* **2006**, 21, 476.

152. J. A. Azurdia, A. Mccrum and R. M. Laine, *J. Mat. Chem.,* **2008**, 18, 3249-3258.

153. Samira Saimuma and A-N. Chowdhury, "Preparation of Fe-Si mixed oxide surface and its application in the removal of toxic from water" *M. Phil Thesis*, BUET, **2011**,

154. Roushown Ali, Kholoud Nour, Abdulrahman Al-warthan, M. Rafiq H. Siddiqui, 'Selective oxidation of benzylic alcohols using Cu-Mn mixed oxide nanoparticles as catalyst' *Arabian Journal of Chemistry,* **2013**, 25, 4815-4819.

155. Gong Zhou, R. S. Parag and R. J. Gorte, 'A Study of Ce–Mn mixed oxides for oxidation catalysis', *Catal Lett*, **2008**, 120,191–197.

156. Hansung Kim and Branko N. Popov, 'Synthesis and Characterization of MnO_2-Based Mixed Oxides as Supercapacitors' *J. Electrochem. Soc.*, **2003,** 150, 56-62.

157. H. Y. Lee and J. B. Goodenough, *J. Solid State Chem.,* **1999**,144, 220,.

158. N. J. Tharayil, R. Raveendron and A. V. Vaidyan, 'synthesis and characterization of nanosized Co-Mn spinel oxide' *Indian J Pure App. Phys.,* **2008**, 46, 47-53.

159. Kurien siby, Sebastian shajo, Methew Jose and K.C. George, *Indian J Pure App. Phys.,* **2004**, 42, 926.

160. M. Suzuki, "Adsorption Engineering", Elsevier, Amsterdam, **1990**, 135-137.

161. A. A. Ismail, A. A. El-Midany, I. A. Ibrahim and H. Matsunaga, "Heavy Metal Removal Using SiO_2 -TiO_2 Binary Oxide", *Adsorption*, **2008**, 14, 21-29.

162. C. Raghavacharya, "Colour Removal from Industrial Effluent", *Chem. Engg. World*, **1997**, 32, 53-58.

163. A. R. Khan, T. A. Al-Bahri and A. Al-Haddad, "Adsorption of Phenol Based Organic Pollutants on Activated Carbon from Multicomponent Dilute Aqueous Solutions", *Wat. Res.*, **1997**, 31, 2102-2112.

164. J. C. Crittenden and W. J. Weber, "Model for Design of Multicomponent Adsorption System", *J. Environm. Engg. Div.*, **1978**, 104, 1175-1193.

165. A. Khenifi, Z. Bouberka, M. Kameche and Z. Derriche, "Adsorption Study of an Industrial Dye by an Organic Clay", *Adsorption,* **2007**, 13, 149-158.

166. I. A. Oke, N. O. Olarinoye, and S. R. A. Adewusi, "Adsorption Kinetics for Arsenic Removal from Aqueous Solutions by Untreated Powdered Eggshell", *Adsorption*, **2008**, 14, 73-83.

167. H.G. El-Shobaky, "Surface and Calalytic Properties of Co, Ni and Cu Binary Oxide System", *Appl. Catal., A.*, **2004**, 278, 1.

168. K. S. Babu, D. Singh and O. N. Srivastava, "Investigatios on the Mixed Oxide Material TiO_2-In_2O_3 in Regard to Photocatalytic Hydrogen Production", *Semicond. Sci. Technol*, **1990**, 5, 364.

169. Wen-Hui Kuan, Chun-Yuan Chen, Ching-Yao Hu and Yu-Min Tzou, *Int'l J. Photoenergy,* **2013**, 2013, 9.

170. Lili Zhang, Yulun Nie, Chun Hu and Xuexiang Hu, *J. Hazard. Mat.,* **2011**, 190, 780–785.

171. Hinda Lachheb, Eric Puzerent, A. Houas and M. Ksibi, *App. Cat. B: Env.,* **2002**, 39, 75-90.

172. Ertan Sahin, Seyid Javad Musevi and Alireza Aslani, 'Antibacterial activity against Escherichia coli and characterization of ZnO and ZnO–Al_2O_3 mixed oxide nanoparticles. *Arabian J. Chem.*, **2013**.

173. Ameer Azam, A. S. Ahmed, M. Oves, M. S. Khan, A. Memic, 'Size-dependent antimicrobial properties of CuO nanoparticles against Gram-positive and -negative bacterial strains', *Int J Nanomedicine*. **2012**, 7, 3527–3535.

174. R. Gokulakrishnan, S. Ravikumer and J. Anadha Raj, 'In vitro antibacterial potential of metal oxide nanoparticles against antibiotic resistant bacteria pathogens', *Asian Pac. J. Trop Dis,* **2012,** 2, 411-413**.**

175. A. W. Bauer, W. M. M. Kirby, L.C. Sherris, M.Truck, 'Antibiotic susceptibility testing standardized single disk method', *Am. J. Clin. Pathol.,* **1966**, 45, 493-496.

176. M. Ocana, 'Uniform particles of manganese compounds obtained by forced hydrolysis of Mn(II) acetate,' *Colloid Polym. Sci.,* **2000**, 278, 443-449.

177. L. Kang, M. Zhang, Z-H. Liu and K. QUI, 'IR spectra of manganese oxides with either layers or tunnel structures', *Spectrometric Acta, part A,* **2007,** 76, 864-869.

178. Y. C. Zhang, T. Qiao, X.Y.Hu and W.D. Zhou, 'Simple hydrothermal preparation of γ-MnOOH nanowires and their Growth', **2005**, 280, 652-657.

179. V. Q. Chiu and J. G. Hering, 'Arsenic adsorption and oxidation at manganite surfaces. Method for simultaneous determination of adsorbed and dissolved arsenic species', *Environ. Sci. Technol.***, 2000**, 34, 2029–2034.

180. A. K. H. Nohman, M. I. Zaki, S. A. A. Mansour, R. B. Fahim and C. Kappenstein, 'Characterization of the thermal genesis course of Mn-oxides from inorganic precursors', *Thermochem. Acta*, **1992**, 210, 103–121.

181. T. Kohler, T. Armbrustor and E. Libowitzky, *J. Solid State Chem.,* **1997**, 133, 486.

182. B. A. M. Figueira, R. S. Angelica and T. Scheller, 'Synthesis and characterization of manganese oxyhydroxide manganite (γ–MnOOH type)', *Ceramics,* **2008**, 54, 193-197.

183. Xinsheng Peng and Izumi Ichinose, 'Manganese oxyhydroxide and oxide nanofibers for high efficiency degradation of organic pollutants', *Nanotechnol.,* **2011**, 22, 1-8.

184. Alexandra Rutz, 'Synthesis and properties of manganese oxide nanoparticles for environmental applications, *NNIN REU Res. Accom,* **2009**, 98-100.

185. P. Tailhedes, B. Gillot and A. Rousset, 'Mixed-valence defect ferrite: a new family of fine powders and thin films of spinel ferrites', *J. De Physique. IV*, **1997**, 2, 249.

186. T. Gao, P. Norby, F. Krumeich, H. Okamoto, R. Nesper and H. Fjellvag, ' Synthesis and properties of layered-structured Mn4O8 nanorods', *J. Phys. Chem. C*, **2010**,114, 922-928.

187. V. Berbenni and A. Marini,' Oxidation behaviour of mechanically activated Mn_3O_4 by TGA/DSC/XRPD', *Mat. Res. Bull,* **2003**, 38, 1859-1866.

188. H.R. Oswald and M.J. Wanpetich, Die Kristallstrukturenvon Mn_5O_8 und $Cd_2Mn_3O_8$', *Helvetica Acta,* **1967**, 50, 2023.

189. J. A. Lee, C. E. Newnham, F. S. Stone and F. L. Tye, 'Thermal decomposition of manganese oxyhydroxide', *J Solid State Chem*, **1980**, 31, 81-93.

190. J. H. Rask and P. R. Buseck, 'Topotactic relations among pyrolusite, manganite and Mn5O8: a high-resolution transmission electron microscopy investigation', American Minerologist, **1986**, 71, 805-814.

191. C. B. Azzoni, M. C. Mozzati and P. Galinetto, 'Thermal stability and structural transition of metastable Mn_5O_8: in situ micro-Raman study', *Solid State Comm.*, **1999**, 112, 375-378.

192. B. Folch, J. Laronova, Y. Guani, C. Guerin and C. Reibel, *J. Solid State Chem.*, **2005**, 178, 2368-2375.

193. D.L. Bish, J.E. Post, 'Thermal Behaviour of complex, tunnel structure Mn-oxides, *Am. Miner.,* **1989**, 74, 177-186.

194. M. Ramstedt, B. M. Anderson, A. Shchukarev and S. Sjoberg, 'Surface properties of hydrous manganite (gamma-MnOOH):A potentiometric, electroacoustic, and X-ray photoelectron spectroscopy study', *Langmuir.* **2004**, 20, 8224.

195. F. Wudl, R.O. Amgus. F. L. Lu, P.M. Allemand, D. J. Vachon, M. Nowak, Z. X. Liu and A. J. Heeger, *J. Am. Chem. Soc.*, **1987**, 109, 3677.

196. Z. Durmusa, M. Tomasa, A. Baykala, H. Kavasb, T. Gürkaynak Altinçekiçc, and M. S. Toprakd, 'The Effect of Neutralizing Agent on the Synthesis and Characterization of Mn_3O_4 Nanoparticles', *Russian J Inorg. Chem.*, **2010**, 55, 1947–1952.

197. R. Chang, Chemistry, McGraw-Hill Inc., fifth edition, International edition, **1994**, 817-819.

198. A. Gunay, E. Arslankaya and I. Tosun, 'Lead removal from aqueous solution by natural and pretreated clinoptilolite: Adsorption equilibrium and kinetics', J. Hazard. Mater.,**2007**, 146, 362-371.

199. M. T. Uddin, M. A. Islam, S. Mahmud and M. Rukanuzzaman, "Adsorptive removal of methylene blue by tea waste" *J. Hazard. Mater.,* **2009**, 164, 58.

200. G. Renmin, S. Yingzhi, C. Jian, L. Huijun and Y. Chao, "Effect of Chemical Modification on Dye Adsorption Capacity of Peaunut Hull", *Dyes and Pigments.,* **2005**, 67, 179.

201. G. C. Catena and F. V. Bright, "Effect of temperature on the adsorption of dyes" *Anal. Chem.*,**1999**, 61, 905.

202. Mao-Xu Zhu, Zheng Wang, Liang-Yong Zhou, 'Oxidative decolorization of methylene blue using pelagite', *J. Hazard. Mater.,* **2008**, 150, 37–45.

203. D. G. Krishna and G. Bhattacharyya, "Adsorption of Methylene Blue on Kaolinite, *Appl. Clay Sci.,* **2002**, 20, 295.

204. C. Namasivayam and R.T. Yamuna, "Adsorption of Direct Red by Biogas Residual Slurry", *Environ. Pollut.*, **1995**, 89, 1.

APPENDIX

APPENDIX

1. Determination of point of zero charge (pH_{PZC}) of Mn-oxide nps

1.1. Point of zero charge of γ−MnOOH nps

Amount of γ−MnOOH nps: 0.005 g Volume of NaCl solution taken: 50mL

Strength of NaCl: 1×10^{-1}M, 1×10^{-2}M and 1×10^{-3}M

Rate of agitation: 215 rpm Time of agitation: 24 hours

Strength of NaOH solution: 0.05M

Table 1: pH metric titration with 1×10^{-1}M NaCl, 1×10^{-2}M NaCl and 1×10^{-3}M NaCl for γ−MnOOH nps

Volume of NaOH solution (mL)	1×10^{-1} M NaCl solution pH		1×10^{-2} M NaCl solution pH		1×10^{-3} M NaCl solution pH	
	suspension	filtrate	suspension	filtrate	suspension	filtrate
0.0	10.4	8.32	6.7	6.5	8.58	7.72
0.5	10.59	9.83	10.12	9.9	9.56	10.07
1.0	10.72	10.28	10.43	10.46	9.99	10.38
1.5	10.8	10.48	10.54	10.66	10.25	10.56
2.0	10.88	10.63	10.68	10.8	10.47	10.68
2.5	10.93	10.73	10.81	10.92	10.62	10.76
3.0	10.98	10.81	10.89	10.99	10.73	10.83
3.5	11.02	10.88	10.98	11.05	10.81	10.9
4.0	11.05	10.93	11.04	11.11	10.89	10.95
4.5	11.07	10.98	11.08	11.16	10.94	10.99
5.0	11.11	11.02	11.11	11.19	11.0	11.06
5.5	11.13	11.06	11.12	11.23	11.06	11.09
6.0	11.15	11.09	11.15	11.26	11.12	11.13
6.5	11.17	11.12	11.16	11.29	11.15	11.15
7.0	11.19	11.12	11.19	11.31	11.18	11.20
7.5	11.21	11.15	11.2	11.34	11.22	11.23
8.0	11.23	11.2	11.22	11.36	11.24	11.24
8.5	11.25	11.22	11.24	11.38	11.26	11.27
9.0	11.27	11.24	11.26	11.41	11.28	11.28
9.5	11.28	11.25	11.27	11.43	11.30	11.30
10.0	11.29	11.27	11.29	11.44	11.32	11.31
10.5	11.31	11.29	11.31	11.46	11.33	11.33
11.0	11.32	11.30	11.31	11.49	11.35	11.35
11.5	11.33	11.32	11.33	11.50	11.35	11.36
12.0	11.34	11.33	11.34	11.51	11.36	11.37
12.5	11.35	11.34	11.35	11.52	11.38	11.38

13.0	11.36	11.35	11.36	11.53	11.39	11.39
13.5	11.38	11.37	11.38	11.54	11.41	11.41
14.0	11.39	11.38	11.38	11.55	11.42	11.42
14.5	11.40	11.39	11.39	11.56	11.45	11.43
15.0	11.40	11.40	11.40	11.57	11.45	11.44
15.5	11.40	11.40	11.41	11.58	11.47	11.46
16.0	11.40	11.41	11.42	11.59	11.48	11.46
16.5	11.40	11.42	11.43	11.59	11.48	11.46

Table 2: Data for volume differences of NaOH solution at various pH of net titration for γ–MnOOH nps for pH_{PZC}

ΔV of NaOH	1×10^{-1} M NaCl solution	1×10^{-2} M NaCl solution		1×10^{-3} M NaCl solution	
	pH	ΔV of NaOH	pH	ΔV of NaOH	pH
0.0	8.32	0.0	6.5	0.0	7.72
0.5	9.83	0.5	9.9	0.5	10.07
1.0	10.28	1.0	10.46	1.0	10.38
1.5	10.48	1.5	10.66	1.5	10.56
2.0	10.63	2.0	10.8	2.0	10.68
2.5	10.73	2.5	10.92	2.5	10.76
3.0	10.81	3.0	10.99	3.0	10.83
3.5	10.88	3.5	11.05	3.5	10.9
4.0	10.93	4.0	11.11	4.0	10.95
4.5	10.98	4.5	11.16	4.5	10.99
5.0	11.02	5.0	11.19	5.0	11.03
5.5	11.06	5.5	11.23	5.5	11.06
6.0	11.09	6.0	11.26	6.0	11.09
6.5	11.12	6.5	11.29	6.5	11.13
7.0	11.12	7.0	11.31	7.0	11.15

1.2. Determination of point of zero charge for MnO_2

Amount of MnO_2 nps: 0.005 g Volume of NaCl solution taken: 50mL

Strength of NaCl: 1×10^{-1}M, 1×10^{-2}M and 1×10^{-3}M

Rate of agitation: 215 rpm Time of agitation: 24 hours

Strength of NaOH solution: 0.05M

Table 3: pH metric titration with 1×10^{-1}M NaCl, 1×10^{-2}M NaCl and 1×10^{-3}M NaCl for MnO_2

Volume of NaOH solution(mL)	1×10^{-1} M NaCl solution		1×10^{-2} M NaCl solution		1×10^{-3} M NaCl solution	
	pH		pH		pH	
	Suspension	Filtrate	Suspension	Filtrate	Suspension	Filtrate
0.0	6.90	7.05	6.90	6.50	7.22	6.53
0.1	7.04	8.76	7.5	6.64	7.75	6.83
0.2	7.22	8.83	8.34	6.85	7.78	8.67
0.3	7.23	9.32	8.85	6.90	8.85	9.06
0.4	7.24	9.39	9.43	6.99	9.15	9.1
0.5	8.77	9.77	9.89	9.90	9.26	9.14
0.6	8.79	10.01	9.89	10.00	9.45	9.41
0.7	8.83	10.09	10.0	10.01	9.52	9.61
0.8	8.86	10.17	10.13	10.06	9.58	9.62
0.9	8.96	10.22	10.17	10.07	9.66	9.63
1.0	9.03	10.55	10.22	10.21	9.86	9.97
1.5	9.43	10.67	10.38	10.22	10.17	10.12
2.0	9.7	10.76	10.52	10.52	10.28	10.23
2.5	9.79	10.83	10.62	10.63	10.46	10.32
3.0	10.14	10.89	10.68	10.7	10.56	10.45
3.5	10.37	10.94	10.73	10.77	10.59	10.52
4.0	10.51	10.98	10.83	10.82	10.71	10.55
4.5	10.57	11.02	10.86	10.84	10.77	10.59
5.0	10.7	11.05	10.89	10.92	10.82	10.63
5.5	10.75	11.08	10.93	10.95	10.87	10.67
6.0	10.85	11.11	10.96	10.98	10.97	10.70
6.5	10.89	11.14	10.99	11.01	11.0	10.73
7.0	10.92	11.16	11.01	11.04	11.03	10.76
7.5	10.99	11.18	11.03	11.06	11.06	10.78
8.0	10.99	11.2	11.05	11.07	11.08	10.8
8.5	11.02	11.22	11.07	11.11	11.1	10.85
9.0	11.04	11.24	11.11	11.13	11.12	10.87
9.5	11.07	11.26	11.12	11.15	11.14	10.89
10.0	11.09	11.27	11.15	11.17	11.17	10.91
10.5	11.11	11.29	11.16	11.19	11.17	10.94
11.0	11.13	11.3	11.18	11.20	11.18	10.98
11.5	11.15	11.31	11.19	11.22	11.20	11.00

12.0	11.17	11.33	11.21	11.23	11.21	11.10
12.5	11.18	11.34	11.22	11.24	11.22	11.20
13.0	11.2	11.35	11.23	11.25	11.24	11.23
13.5	11.21	11.36	11.23	11.27	11.25	11.24
14	11.24	11.37	11.24	11.28	11.26	11.25
14.5	11.25	11.38	11.24	11.29	11.26	11.26
15	11.26	11.39	11.25	11.31	11.27	11.27
15.5	11.27	11.4	11.26	11.31	11.27	11.27
16	11.28	11.4	11.26	11.31	11.28	11.28

Table 4: Data for volume differences of NaOH solution at various pH of net titration

1×10^{-1} M NaCl solution		1×10^{-2} M NaCl solution		1×10^{-3} M NaCl solution	
ΔV of NaOH	pH	ΔV of NaOH	pH	ΔV of NaOH	pH
0	7.05	0	6.5	0	6.53
0.1	8.76	0.1	6.64	0.1	6.83
0.2	8.83	0.2	6.85	0.2	8.67
0.3	9.32	0.3	6.9	0.3	9.06
0.4	9.39	0.4	6.99	0.4	9.1
0.5	9.77	0.5	9.9	0.5	9.14
0.6	10.01	0.6	10	0.6	9.41
0.7	10.09	0.7	10.01	0.7	9.61
0.8	10.17	0.8	10.06	0.8	9.62
0.9	10.22	0.9	10.07	0.9	9.63
1.0	10.55	1.0	10.21	1.0	9.97
1.5	10.67	1.5	10.22	1.5	10.12
2.0	10.76	2.0	10.52	2.0	10.23
2.5	10.83	2.5	10.63	2.5	10.32
3.0	10.89	3.0	10.7	3.0	10.45
3.5	10.94	3.5	10.77	3.5	10.52
4.0	10.98	4.0	10.82	4.0	10.55
4.5	11.02	4.5	10.84	4.5	10.59
5.0	11.05	5.0	10.92	5.0	10.63
5.5	11.08	5.5	10.95	5.5	10.67
6.0	11.11	6.0	10.98	6.0	10.7
6.5	11.14	6.5	11.01	6.5	10.73
7.0	11.16	7.0	11.04	7.0	10.76

1.3. Determination of point of zero charge for Mn_3O_4 nps

Amount of Mn_3O_4: 0.005 g Volume of NaCl solution taken: 50mL

Strength of NaCl: 1×10^{-1}M, 1×10^{-2}M and 1×10^{-3}M

Rate of agitation: 215 rpm Time of agitation: 24 hours

Strength of NaOH solution: 0.05M

Table 5: pH metric titration with 1×10^{-1}M NaCl, 1×10^{-2}M NaCl and 1×10^{-3}M NaCl solution

Volume of NaOH solution (mL)	1×10^{-1} M NaClsolution		1×10^{-2} M NaCl solution		1×10^{-3} M NaCl solution	
	pH		pH		pH	
	Suspension	Filtrate	Suspension	Filtrate	Suspension	Filtrate
0.0	7.02	8.32	6.7	6.5	8.58	7.72
0.5	10.4	9.83	10.12	9.9	9.56	10.07
1.0	10.59	10.28	10.43	10.46	9.99	10.38
1.5	10.72	10.48	10.54	10.66	10.25	10.56
2.0	10.8	10.63	10.68	10.8	10.47	10.68
2.5	10.88	10.73	10.81	10.92	10.62	10.76
3.0	10.93	10.81	10.89	10.99	10.73	10.83
3.5	10.98	10.88	10.98	11.05	10.81	10.9
4.0	11.02	10.93	11.04	11.11	10.89	10.95
4.5	11.05	10.98	11.08	11.16	10.94	10.99
5.0	11.07	11.02	11.11	11.19	11	11.06
5.5	11.11	11.06	11.12	11.23	11.06	11.09
6.0	11.13	11.09	11.15	11.26	11.12	11.13
6.5	11.15	11.12	11.16	11.29	11.15	11.15
7.0	11.17	11.12	11.19	11.31	11.18	11.2
7.5	11.19	11.15	11.2	11.34	11.22	11.23
8.0	11.21	11.2	11.22	11.36	11.24	11.24
8.5	11.23	11.22	11.24	11.38	11.26	11.27
9.0	11.25	11.24	11.26	11.41	11.28	11.28
9.5	11.27	11.25	11.27	11.43	11.3	11.3
10.0	11.28	11.27	11.29	11.44	11.32	11.31
10.5	11.29	11.29	11.31	11.46	11.33	11.33
11.0	11.31	11.3	11.31	11.49	11.35	11.35
11.5	11.32	11.32	11.33	11.5	11.35	11.36
12.0	11.33	11.33	11.34	11.51	11.36	11.37
12.5	11.34	11.34	11.35	11.52	11.38	11.38
13.0	11.35	11.35	11.36	11.53	11.39	11.39
13.5	11.36	11.37	11.38	11.54	11.41	11.41
14.0	11.38	11.38	11.38	11.55	11.42	11.42
14.5	11.39	11.39	11.39	11.56	11.45	11.43
15.0	11.40	11.40	11.4	11.57	11.45	11.44
15.5	11.40	11.40	11.41	11.58	11.47	11.46
16.0	11.40	11.41	11.42	11.59	11.48	11.46
16.5	11.40	11.42	11.43	11.59	11.48	11.46

Table 6: Data for volume differences of NaOH solution at various pH of net titration

1×10^{-1} M NaCl solution		1×10^{-2} M NaCl solution		1×10^{-3} M NaCl solution	
ΔV of NaOH	pH	ΔV of NaOH	pH	ΔV of NaOH	pH
0.0	8.72	0.0	6.5	0.0	7.72
0.5	8.93	0.5	9.9	0.5	10.07
1.0	9.57	1.0	10.46	1.0	10.38
1.5	9.77	1.5	10.66	1.5	10.56
2.0	9.99	2.0	10.8	2.0	10.68
2.5	10.09	2.5	10.92	2.5	10.76
3.0	10.24	3.0	10.99	3.0	10.83
3.5	10.28	3.5	11.05	3.5	10.9
4.0	10.28	4.0	11.11	4.0	10.95
4.5	10.29	4.5	11.16	4.5	10.99
5.0	10.29	5.0	11.19	5.0	11.03
5.5	10.51	5.5	11.23	5.5	11.06
6.0	10.62	6.0	11.26	6.0	11.09
6.5	10.71	6.5	11.29	6.5	11.13
7.0	10.79	7.0	11.31	7.0	11.15